SMHI REPORTS OCEANOGRAPHY No. 26, August 1999

RCO - Rossby Centre regional Ocean climate model: model description (version 1.0) and first results from the hindcast period 1992/93

H. E. Markus Meier [1], Ralf Döscher [1] , Andrew C. Coward [2], Jonas Nycander [3] and Kristofer Döös[3]

Cover figure: Sea surface temperature (in ^{o}C) and mean ice thickness (in cm) from February 23, 1993 as obtained from the Rossby Centre coupled ice-ocean model after 282 days of integration. A comparison with the corresponding ice-sst chart published by SMHI is shown in Section 5 of this report.

[1]Rossby Centre, Swedish Meteorological and Hydrological Institute, 601 76 Norrköping, Sweden
[2]James Rennell Division, Southampton Oceanography Centre, Southampton SO14 3ZH, UK
[3]Department of Meteorology (MISU), Stockholm University, 106 91 Stockholm, Sweden

Contents

1 Introduction

The Swedish Regional Climate Modelling Programme, SWECLIM, aims to increase our knowledge of the effects of climate change in Sweden and the other Nordic countries (SWECLIM, 1998). Thereby, specific regional consequences of global climate change like river discharge, precipitation, regional ice cover, temperatures of air and water and water quality conditions are of special interest for the Nordic societies. To meet this challenge, dynamical downscaling methods are applied. So far, the regional atmospheric model HIRLAM has been used together with boundary data from global ocean-atmosphere circulation models (HadCM2 and ECHAM4/OPYC3) to simulate 10 year time slices (Rummukainen et al., 1998; Räisänen et al., 1999). OGCM fields for the Baltic Sea cannot be expected to be realistic due to coarse resolution. Hence, the Baltic Sea was either parameterized in a simplistic way or represented by the process-oriented PROBE-Baltic model (Omstedt, 1990). The latter consists of 13 boxes with high vertical resolution using parameterizations for horizontal transports between the boxes.

As SWECLIM aims at details of regional climate, a fully three-dimensional model has to be used to represent the Baltic Sea within coupled climate scenarios. A 3D model gives us the possibility to resolve horizontal features like up- and downwelling events, fronts or mesoscale eddies and wind driven transports which are not considered in horizontally integrated models. For a sea ice model, the 3D ocean structure is essential to establish adequate horizontal patterns of ice coverage and compactness. Improved annual cycles of sea ice seasons are expected to result in an improved atmosphere climate simulation for the Nordic countries.

Regional climate impact studies of the future Baltic marine environment (e.g., storm surges, ice seasons and sea surface temperatures, stratification changes due to changed precipitation and river runoff, mean sediment transports, nutrient load impacts, oxygen resources, etc.) require detailed highly resolved information. Considering the needs of potential end users, 3D information as well as 3D-generated information appears to be of critical importance. As a response to these requirements, RCO, the Rossby Centre Ocean Model, has been developed. First results presented in Section 5 of this report indicate that RCO is well suited to meet the above goals.

Several models have been used to study the dynamics of the Baltic Sea. Most of them are process-oriented or two dimensional models, e.g., Welander (1974), Walin (1977), Stigebrandt (1983, 1987), Omstedt (1990), Gidhagen and Håkansson (1992). Three dimensional models were used by Simons (1976), Kielmann (1981) and Krauß and Brügge (1991) for studying the wind-driven circulation of the Baltic Sea. An ocean general circulation model of the whole Baltic Sea was presented by Lehmann (1992, 1995), and regional models of the western Baltic Sea by Seifert and Fennel (1994) and Meier (1996). Meier (1996) has also data assimilation included. Using the same model type Elken (1996) has investigated in deep water overflow, circulation and vertical exchange in the Baltic Proper. Schrum and Backhaus (1999) used a coarse resolution North Sea and Baltic Sea model for sensitivity studies of atmosphere-ocean heat exchange and

heat content for 1983-84.

Recently, several research groups in countries around the Baltic Sea have started to setup 3D ocean models with the purpose to perform multi-year integrations. In that context the activities within BALTEX (the BALtic Sea EXperiment) should be mentioned. One of the main purpose of BALTEX is the modelling of the water and energy budget of the Baltic catchment area which surrounds the Baltic Sea. The water budget of the Baltic Sea is governed by the huge impact of river runoff and the limitation of water exchange with the North Sea due to the shallow and narrow Danish Straits. The calculation of the net outflow from the Baltic Sea through the Danish Straits is an important component of the water budget of the whole BALTEX region. Great horizontal salinity gradients are characteristic for the area between the Skagerrak and the Baltic Proper. As baroclinic effects modify the transports through the Danish Straits, the salt budget of the Baltic Sea has to be included into the considerations. To achieve improved water and salt budgets, accurate modelling and monitoring of the highly variable in- and outflow through the narrow Danish Straits are required over long time periods. The 3D model described in this report with a horizontal resolution of 2 nautical miles will be able to fulfill the above mentioned requirements within SWECLIM and will contribute also to BALTEX and to the planned main BALTEX experiment BRIDGE (BALTEX, 1997).

At the beginning of the first SWECLIM phase a decision had to be made about the model code to be used. High resolution with a corresponding short time step is essential to resolve the bottom topography and small scale processes with impact on the large scale. Integrations over 10 years or longer with a sufficiently resolved Baltic Sea model requires a state-of-the-art super-computer which is available for SWECLIM in form of the CRAY-T3E with 272 processors at the Swedish National Supercomputer Centre (NSC) in Linköping. When SWECLIM started no multi-year integrations were available. Conventional computational capacity did not allow longterm simulations. None of the available Baltic Sea models two years ago was suitable for parallel computing with sufficient performance. Especially, the pre-operationally running forecast model HIROMB (HIgh Resolution Operational Model for the Baltic Sea) at SMHI was not parallelized. Further on, parameterizations of mixed layer and sea ice schemes within HIROMB apply to its original purpose of short term forecast rather than to decade-long integrations. Hence, RCO has been developed within SWECLIM using the OCCAM version (Ocean Circulation Climate Advanced Modelling Project in Southampton) of the Bryan - Cox - Semtner primitive equation ocean model with a free surface (Bryan, 1969; Cox, 1984; Killworth et al., 1991; Webb et al., 1997). As the OCCAM project focuses on global scales it was necessary to add Baltic Sea specific parameterizations like a turbulence scheme, open boundary conditions, sea ice, etc..

The report is organized as follows: In the second and third section the model equations for the ocean model and the sea ice model are described. In the fourth section technical details about the used code are outlined. According to the strategy within SWECLIM two hindcast periods have been defined for evaluating the model using observed atmospheric forcing data. The first period - May 1992 until September 1993 - has been

chosen testing the model performance during the latest major inflow event in January 1993. First results are presented in the fifth section. An accompanied report will describe the results of the longer hindcast period May 1980 until September 1993 using a coarser grid version of the model presented here. The report ends with summary and future outlook.

2 Ocean model description

2.1 Basic model equations

The model is based on the primitive equations (e.g., Krauß, 1973; Müller and Willebrand, 1989) which are derived from the Navier-Stokes equations using the Boussinesq, the shallow water, the traditional and the hydrostatic approximation. The traditional approximation neglects the component of the Coriolis force due to vertical current velocity. The conservation of momentum, mass, potential temperature and salinity are

$$\frac{\partial u}{\partial t} + \Gamma(u) - fv = -\frac{1}{\rho_0 R \cos\phi}\frac{\partial p}{\partial \lambda} + F_u\,, \tag{1}$$

$$\frac{\partial v}{\partial t} + \Gamma(v) + fu = -\frac{1}{\rho_0 R}\frac{\partial p}{\partial \phi} + F_v\,, \tag{2}$$

$$\Gamma(1) = 0\,, \tag{3}$$

$$\frac{\partial p}{\partial z} = -g\,\rho\,, \tag{4}$$

$$\frac{\partial T}{\partial t} + \Gamma(T) = F_T + \frac{1}{\rho_0\, c_{pw}}\frac{\partial I}{\partial z}\,, \tag{5}$$

$$\frac{\partial S}{\partial t} + \Gamma(S) = F_S\,, \tag{6}$$

$$\rho = \rho(T, S, p) \tag{7}$$

with the advection operator

$$\Gamma(\mu) = \frac{1}{R\cos\phi}\left[\frac{\partial}{\partial\lambda}(u\,\mu) + \frac{\partial}{\partial\phi}(v\,\mu\,\cos\phi)\right] + \frac{\partial}{\partial z}(w\,\mu)\,, \tag{8}$$

$\mu = (T,\, S,\, u,\, v,\, 1)$, Coriolis parameter $f = 2\,\Omega\,\sin\phi$, earth radius $R = 6370\,km$, angular speed of rotation of the earth $\Omega = 2\,\pi/86\,164\,s$, acceleration of gravity $g = 9.81\,m\,s^{-2}$, reference density of water $\rho_0 = 10^3 kg\,m^{-3}$, specific heat capacity of water $c_{pw} = 4.186 \cdot 10^3 J\,kg^{-1}\,K^{-1}$ and solar insolation I (see Section 2.3).

This system of partial differential equations (1)–(7) can be solved for the 7 dependent variables velocity u, v, w, pressure p, potential temperature T, salinity S and density ρ as a function of time t, latitude ϕ and longitude λ as well as water depth z (< 0) if an equation of state (7) and boundary conditions are prescribed. The vertical coordinate z is positive upward and zero at the sea surface. F_u, F_v, F_T and F_S denote the divergences of turbulent Reynolds fluxes which are parameterized according to the austausch concept:

$$F_u = \frac{\partial}{\partial z}\left(\nu_t(z)\,\frac{\partial u}{\partial z}\right) + A_M\,\nabla^2 u\,, \tag{9}$$

$$F_v = \frac{\partial}{\partial z}\left(\nu_t(z)\,\frac{\partial v}{\partial z}\right) + A_M\,\nabla^2 v\,, \tag{10}$$

$$F_T = \frac{\partial}{\partial z}\left(\frac{\nu_t}{\sigma_t}(z)\,\frac{\partial T}{\partial z}\right) + A_T\,\nabla^2 T\,, \tag{11}$$

$$F_S = \frac{\partial}{\partial z}\left(\frac{\nu_t}{\sigma_t}(z)\,\frac{\partial S}{\partial z}\right) + A_T\,\nabla^2 S \tag{12}$$

with

$$\nabla^2\mu = \frac{1}{R^2\,\cos^2\phi}\,\frac{\partial^2\mu}{\partial\lambda^2} + \frac{1}{R^2\,\cos\phi}\,\frac{\partial}{\partial\phi}\left(\frac{\partial\mu}{\partial\phi}\,\cos\phi\right) \tag{13}$$

(additional metric terms in F_u and F_v are neglected). A_M and A_T denote horizontal austausch coefficients of viscosity and diffusivity, respectively. ν_t is the turbulent vertical friction coefficient and σ_t the turbulent Prandtl number. As timescales of barotropic and baroclinic processes are different, it is more efficient rather than to integrate Eq.(1)–(7) to introduce an external and internal mode with different timesteps. Hence, the hydrostatic equation (4) is integrated vertically

$$p - p(z=0) = P_L + \int_z^0 g\,\rho\,dz\,, \tag{14}$$

and a free surface $\zeta(\lambda,\phi,t)$

$$p(z=0) =: g\,\rho_0\,\zeta \tag{15}$$

is defined which is assumed to be small compared to the water depth H. In (14) use of the dynamical boundary condition leads to the introduction of sea surface air pressure P_L. With the definition of volume fluxes or mean velocities,

$$U := H\,\bar{u} := \int_{-H}^{\zeta} u\,dz \quad \text{and} \quad V := H\,\bar{v} := \int_{-H}^{\zeta} v\,dz \tag{16}$$

vertical integration of continuity equation (3) and momentum equations (1) and (2) result in prognostic equations for the external mode

$$\frac{\partial\zeta}{\partial t} + \frac{1}{R\cos\phi}\left[\frac{\partial U}{\partial\lambda} + \frac{\partial}{\partial\phi}\,(V\cos\phi)\right] = 0\,, \tag{17}$$

$$\frac{\partial U}{\partial t} - fV + \frac{gH}{R\cos\phi}\,\frac{\partial\zeta}{\partial\lambda} = \frac{\tau_\lambda}{\rho_0} - \frac{H}{\rho_0 R\cos\phi}\,\frac{\partial P_L}{\partial\lambda} - \frac{\tau^B_\lambda}{\rho_0} + X\,, \tag{18}$$

$$\frac{\partial V}{\partial t} + fU + \frac{gH}{R}\,\frac{\partial\zeta}{\partial\phi} = \frac{\tau_\phi}{\rho_0} - \frac{H}{\rho_0 R}\,\frac{\partial P_L}{\partial\phi} - \frac{\tau^B_\phi}{\rho_0} + Y\,, \tag{19}$$

with

$$X = -\int_{-H}^{\zeta}\Gamma(u)\,dz - \frac{g}{\rho_0\,R\,\cos\phi}\int_{-H}^{\zeta}dz\int_z^0\frac{\partial\rho}{\partial\lambda}\,dz + A_M\int_{-H}^{\zeta}\nabla^2 u\,dz\,, \tag{20}$$

$$Y = -\int_{-H}^{\zeta}\Gamma(v)\,dz - \frac{g}{\rho_0\,R}\int_{-H}^{\zeta}dz\int_z^0\frac{\partial\rho}{\partial\phi}\,dz + A_M\int_{-H}^{\zeta}\nabla^2 v\,dz\,. \tag{21}$$

According to the boundary conditions wind stress $\vec{\tau}$ and bottom stress $\vec{\tau}^B$ need to be specified in Eq.(18) and (19) completing the set of equations. The lateral boundary conditions are "free slip" for momentum and isolation for tracer:

$$u = v = \frac{\partial T}{\partial \vec{n}} = \frac{\partial S}{\partial \vec{n}} = 0\,. \tag{22}$$

$\vec{n}$ is a normal vector to the wall. At the ocean surface ($z = 0$) the boundary conditions are

$$\rho_0\,\nu_t\,\frac{\partial u}{\partial z} = \tau_\lambda\,, \quad \rho_0\,\nu_t\,\frac{\partial v}{\partial z} = \tau_\phi\,, \tag{23}$$

$$\rho_0\,c_{pw}\,\frac{\nu_t}{\sigma_t}\,\frac{\partial T}{\partial z} = Q_T\,, \quad \frac{\nu_t}{\sigma_t}\,\frac{\partial S}{\partial z} = S_F\,, \tag{24}$$

$$w \tilde{=} \frac{\partial \zeta}{\partial t}\,. \tag{25}$$

Q_T and S_F are total heat flux at the sea surface without solar insolation and salt flux, respectively. At the bottom ($z = -H$) the corresponding equations are

$$\rho_0\,\nu_t\,\frac{\partial u}{\partial z} = \tau^B_\lambda\,, \quad \rho_0\,\nu_t\,\frac{\partial v}{\partial z} = \tau^B_\phi\,, \tag{26}$$

$$\frac{\partial T}{\partial z} = 0\,, \quad \frac{\partial S}{\partial z} = 0\,, \tag{27}$$

$$w = -\frac{u}{R\,\cos\phi}\,\frac{\partial H}{\partial \lambda} - \frac{v}{R}\,\frac{\partial H}{\partial \phi}. \tag{28}$$

The equation of state (7) will be discussed in Section 2.4. Use is made of the polynomial fit of Bryan and Cox (1972). Bottom friction is parameterized according to Cox (1984):

$$\vec{\tau}^B = \rho_0\,c_b\,\sqrt{u^2 + v^2}\begin{pmatrix} u \\ v \end{pmatrix} \tag{29}$$

with $u = u(z{=}{-}H)$, $v = v(z{=}{-}H)$.
The prognostic equations of the internal mode (1), (2), (5), (6) together with the diagnostic equations (3), (7), (14) and the prognostic equations of the external mode (17), (18), (19) are discretized on the Arakawa–B–grid (Mesinger and Arakawa, 1976) and are integrated asynchronously with a baroclinic timestep Δt_c and a much smaller barotropic timestep Δt_b. A detailed description is given by Killworth et al. (1989).

2.2 Sea surface boundary conditions

For hindcast experiments using atmospheric forcing data like $10\,m$ wind speed, $2\,m$ air temperature, sea surface air pressure, $2\,m$ relative humidity, total cloudiness and precipitation one need to specify bulk formulae to calculate sea surface fluxes. The used parameterizations are outlined below and follow mainly Omstedt and Nyberg (1995). Compared to their heat flux package the bulk formulae for sensible and latent heat (Friehe and Schmitt, 1976) have been replaced because Rutgersson (1999) found that these formulations applied to the PROBE-Baltic model give too high evaporation and too low surface temperatures.

2.2.1 Wind stress

The wind stress in Eq.(23) is parameterized according to Large and Pond (1981):

$$\vec{\tau} = c_{aw}^{d}\,\rho_a\,\left|\vec{U}_{10}\right|\,\vec{U}_{10} \tag{30}$$

with

$$c_{aw}^{d}\ \times\ 10^3 = \begin{cases} 1.2 & : \quad 0 < \left|\vec{U}_{10}\right| \leq 11\,m/s \\ 0.49 + 0.065\,\left|\vec{U}_{10}\right| & : \quad 11 < \left|\vec{U}_{10}\right| \leq 22\,m/s \end{cases} . \tag{31}$$

$\vec{U}_{10}$ denotes wind speed in $10\,m$ height and ρ_a air density.

2.2.2 Heat flux

The total heat flux through the sea surface Q_{TOT} is given by the sum of shortwave radiation Q_{SW}, longwave incoming radiation $Q_{LW\downarrow}$, longwave outgoing radiation $Q_{LW\uparrow}$, sensible Q_S and latent heat fluxes Q_L:

$$Q_{TOT} = Q_{SW} + Q_{LW\downarrow} - Q_{LW\uparrow} + Q_S + Q_L\,. \tag{32}$$

The shortwave radiation Q_S penetrates into deeper ocean layers and is discussed together with the radiation model (Section 2.3). The total heat flux without solar insolation Q_T specified in Eq.(24) is given by

$$Q_T = Q_{LW} + Q_S + Q_L \quad \text{with} \quad Q_{LW} = Q_{LW\downarrow} - Q_{LW\uparrow}. \tag{33}$$

The sensible and latent heat fluxes are determined by temperature and moisture differences between water and air, respectively. The parameterization follows Large and Pond (1982) including a stability dependence of the transfer coefficients. The sensible heat flux Q_S is given by

$$Q_S = \rho_a\,c_{pa}\,c_{aw}^{s}\,\left|\vec{U}_{10}\right|\,(T_a - T_w) \tag{34}$$

with air density $\rho_a = 1.225\,kg\,m^{-3}$, specific heat capacity of air $c_{pa} = 1.008 \cdot 10^3 J\,kg^{-1}\,K^{-1}$, air temperature T_a and water temperature of the first model layer T_w (=T in Section 2.1). The transfer coefficient c_{aw}^{h} (Stanton number) is given by

$$c_{aw}^{s}\ \times\ 10^3 = \begin{cases} 1.13 & : \quad (T_a - T_w) < 0 \quad \text{unstable} \\ 0.66 & : \quad (T_a - T_w) \geq 0 \quad \text{stable} \end{cases} . \tag{35}$$

The latent heat flux Q_L is given by

$$Q_L = L_{aw}\,E \tag{36}$$

with $L_{aw} = 2.5 \cdot 10^6\,J\,kg^{-1}$ latent heat of vaporization. The evaporation E is calculated according to

$$E = \rho_a\,c_{aw}^{l}\,\left|\vec{U}_{10}\right|\,(q_a - q_w) \tag{37}$$

with q_a and q_w specific humidity in $2\,m$ height of the atmosphere and close to the water surface, respectively. $c^l_{aw} = 1.15$ is the corresponding transfer coefficient (Dalton number).

Following Maykut (1986) specific humidity is calculated from water vapour pressure e according to

$$q_{a,w} = \epsilon \, \frac{e_{a,w}}{P_0} \tag{38}$$

with $\epsilon = 0.62197$ and $P_0 = 1.013 \cdot 10^5 Pa$. Water vapour pressure in the atmosphere e_a and close to the sea surface e_w is derived from

$$e_a = U\, r\, e^{\frac{c_1\, T_a}{T_a + T_0 - c_2}} \quad \text{and} \quad e_w = r\, e^{\frac{c_1\, T_w}{T_w + T_0 - c_2}} \tag{39}$$

with relative humidity U, $r = 6.1078 \cdot 10^2\, Pa$, $c_1 = 17.269$, $c_2 = 35.86\, K$ and $T_0 = 273.155\, K$.

The longwave incoming radiation $Q_{LW\downarrow}$ is calculated according to Bodin (1979)

$$Q_{LW\downarrow} = \epsilon_w\, \sigma_s\, T^4_{air}\, (a_1 + a_2\, e^{0.5}_a)\, (1 + a_3\, C^2_a) \tag{40}$$

with emissivity of the water surface $\epsilon_w = 0.97$, Stefan Boltzmann's constant $\sigma_s = 5.68 \cdot 10^{-8} W\, m^{-2}\, K^{-4}$, total cloudiness C_a and the empirical constants $a_1 = 0.68$, $a_2 = 0.0036$ and $a_3 = 0.18$.

The longwave outgoing radiation $Q_{LW\uparrow}$ is calculated from Stefan Boltzmann's law

$$Q_{LW\uparrow} = \epsilon_w\, \sigma_s\, T^4_w\,. \tag{41}$$

2.2.3 Freshwater flux

According to Krauß (1973) the salt flux S_F in the boundary condition for salinity (partial mass, see Eq.24)) is given to

$$S_F = -H_S\, S \tag{42}$$

with the freshwater flux

$$H_S = P - E \tag{43}$$

and precipitation P. This traditional approach is used here. Steinhorn (1991) discussed an inaccuracy in the formulation (42) and suggested

$$S_F = -H_S\, \frac{S}{1 - S}\,. \tag{44}$$

As the error for the Baltic Sea surface water is smaller than one percent the traditional boundary condition is suitable. For the hypersaline Dead Sea the revised formula would have to be used.

2.3 Radiation model

Shortwave radiation penetrates into the ocean either through the open sea surface or through the ice cover (see Section 3). The shortwave energy flux through the open water surface is

$$Q_{SW} = Q^0_{SW}\,(1-\alpha_w) \tag{45}$$

with incoming solar radiation Q^0_{SW} and sea surface albedo α_w.

According to Bodin (1979) the incoming solar radiation at the sea surface can be calculated from

$$Q^0_{SW} = T_u\,S_0\,\cos\theta\,(T_r - A_w)(1 - C_a\,F_a) \tag{46}$$

with the atmospherical turbidity $T_u = 0.95$, the solar constant $S_0 = 1.353{\cdot}10^3\,J\,m^{-2}\,s^{-1}$ and the zenith angle θ. T_r and A_w are transmission and absorption functions and F_a is a cloud function:

$$T_r = 1.041 - 0.16\,\cos\theta^{-0.5} \tag{47}$$

$$F_a = 0.55 + 0.01\,\cos\theta^{-1} \tag{48}$$

$$A_w = 0.077\,m^{0.3}\,\cos\theta^{-0.3}\,. \tag{49}$$

The zenith angle θ is calculated from latitude ϕ, sun's declination angle δ and sun's hour angle α_n:

$$\cos\theta = \sin\phi\,\sin\delta + \cos\phi\,\cos\delta\,\cos\alpha_n \tag{50}$$

with

$$\delta = 23.44^o\,\cos\left(\frac{172.25 - d}{365.25}\,2\pi\right) \tag{51}$$

(d is the day of the corresponding year) and

$$\alpha_n = (1 - \frac{t_s}{12})\,\pi\,, \quad t_s \in [0, 24[\,. \tag{52}$$

(t_s is the hour of the corresponding day). The model time is calculated from an exact calendar including leap years. The daily cycle is included in the model. m is the optical path length and is given by

$$m = 1.25 + 0.75\,\sin\left(2\pi\,\frac{d - 120}{365.25}\right)\,. \tag{53}$$

The albedo is calculated from Fresnel's formula

$$\alpha_w = \frac{1}{2}\,\left(\frac{\sin^2(\theta-\psi)}{\sin^2(\theta+\psi)} + \frac{\tan^2(\theta-\psi)}{\tan^2(\theta+\psi)}\right) \tag{54}$$

with the refraction angle $\psi = \arcsin(\sin\theta\,/1.333)$.

The divergence of absorbed intensity I of the penetrated shortwave radiation is heating the water column (see Eq.(5)). This effect can contribute to summer time warming of up to 2^oC in $10\,m$ depth (Meier, 1996) and is included in the model. The solar intensity is parameterized according to Paulson and Simpson (1977) with two extinction lengths

$$I = Q_{SW}\left[R_{SW}\, e^{\frac{z}{\zeta_1}} + (1 - R_{SW})\, e^{\frac{z}{\zeta_2}}\right] \tag{55}$$

with $R_{SW} = 0.64$, $\zeta_1 = 1.78\,m$ and $\zeta_2 = 3.26\,m$. Usually optical water types are classified according to Jerlov (1968) but not very detailed information is available for the Baltic Sea. Jerlov classified the Skagerrak water as coastal water type 1 and the Baltic proper as coastal water type 3 without giving the corresponding extinction lengths. Hence, climatology data from Dera (1992, see his Tab. 5.3.1) has been used to optimize the unknown constant R_{SW} and the extinction lengths ζ_1 and ζ_2 utilizing a least-squares fit. The available data are average monthly means of solar energy over the entire spectrum reaching particular depths in the southern Baltic. The optimization procedure has been done as described in Paulson and Simpson (1977). For comparison, the most turbid optical water type III for oceans according to Jerlov (1968) uses the values $R_{SW} = 0.78$, $\zeta_1 = 1.4\,m$ and $\zeta_2 = 7.9\,m$.

Not very much is known about the parameterization of clouds in Eq.(46). Very different approaches are used in the literature (e.g. Reed, 1977; Parkinson and Washington, 1979; Bodin, 1979). Three different radiation models are compared by Niekamp (1992) but he could not decide about the quality due to erroneous radiation data. Hence, the radiation model could be used only to estimate the solar insolation.

The effect of various parameterizations of shortwave, longwave, sensible and latent heat fluxes on the sea surface heat budget of the Arctic Ocean and Nordic Seas has been shown by Simonsen and Haugan (1996).

2.4 Equation of state

The equation of state of sea water is calculated using a third order polynomial approximation in form of sigma anomalies. The method is taken from that described by Bryan and Cox (1972). The coefficients compute density as a function of temperature and salinity at predetermined depths as used in the model. The equation of state is set by the Joint Panel on Oceanographic Tables and Standards (UNESCO, 1981) as described by Gill (1982). An iterative least-squares polynomial fitting for the overdetermined system is performed.

Other authors like Lehmann (1995) or Meier (1996) use the equation of state from Millero and Kremling (1976) which is better adjusted to Baltic Sea conditions because dissolved solids from river water input are considered additionally. As the differences for the range of Baltic Sea temperatures and salinities are smaller than $10^{-4}\,g\,cm^{-3}$ and as the equation from Millero and Kremling (1976) is computationally more expensive, the polynomial fit of the UNESCO formula is used here.

2.5 Model domain and resolution

As outlined in the introduction RCO has been developed to simulate 10 year timeslice experiments of control and scenario simulations. The water exchange between Baltic and North Sea is mainly governed by the sea level difference between Kattegat and western Baltic Sea. Hence, it is necessary at least to include the North Sea in the model domain to simulate sea level elevations in the Kattegat. As the whole shelf can be filled up with water during intense storm surges (Bertil Håkansson, pers. comm.) also the signal of the North Atlantic has to be taken into account. Under special circumstances these storms lead to major Baltic inflow events replacing the bottom water of the Baltic Sea. As will be shown in Section 5, the salt water transports into the Baltic are dependent on the hydrography in the Kattegat. Under normal meteorological conditions low saline Baltic Sea water flows out through the Danish Straits. The Belt Sea front and the Kattegat - Skagerrak front separate Baltic and North Sea water (Wattenberg, 1941). During inflow events these fronts move towards the sills in the Danish Straits (Meier, 1996). Adequate modelling of the Kattegat and Skagerrak hydrography makes it necessary to simulate the whole North Sea. Hence, the final model domain of RCO will cover Baltic and North Sea (Fig.1) with open boundary conditions towards the North East Atlantic and in the English Channel. A storm surge model based on the shallow water equations will be used to model the wind forced sea levels outside the border of RCO forced by the atmospheric regional model. These results will be added to available tide data and provide the necessary information at the open boundaries. To reduce the computational burden during the development and testing phase a smaller model domain with open boundaries in the northern Kattegat has been used. In Section 5 results of the limited area version of RCO (Baltic Sea only) are presented. Henceforth this model configuration will be named RCO version 1.0.

For realistic simulations of the Baltic Sea a fine model grid in horizontal and vertical direction is necessary to resolve the topography of the Danish Straits and other sills and narrows and to describe overflow and other small scale processes with impact on the large scale. The width of the narrowest part of the Sound near Helsingør-Helsingborg amounts $4\,km$ approximately. Darß Sill with a depth of about $18\,m$ separates the Belt Sea from the Arkona Basin. The Sound has a sill depth of only $7\,m$ at the south entrance (Drogden). The topography is shown below (Fig.3).

Further, horizontal salinity fronts and strong vertical stratification have to be resolved too. For example, after the salt water inflow event in 1993, in mid-February, the vertical salinity gradient between the mixed surface layer water in the Arkona Basin and the salty bottom water amounted $13\,PSU$ per $5\,m$ (Meier, 1996).

A third argument for high resolution is given by the size of internal Rossby radii. On the basis of a data set recorded in the Baltic Sea during 1977 - 1987 Fennel et al. (1991) found that the Rossby radii show a seasonal cycle with minimum values during winter and autumn, and maxima during summer. The largest Rossby radius, $7\,km$, was found in the Bornholm Basin and the smallest ones, $1.3\,km$, in the Belt Sea and in the Gulf of Finland during autumn. Similar results were reported from Aitsam and

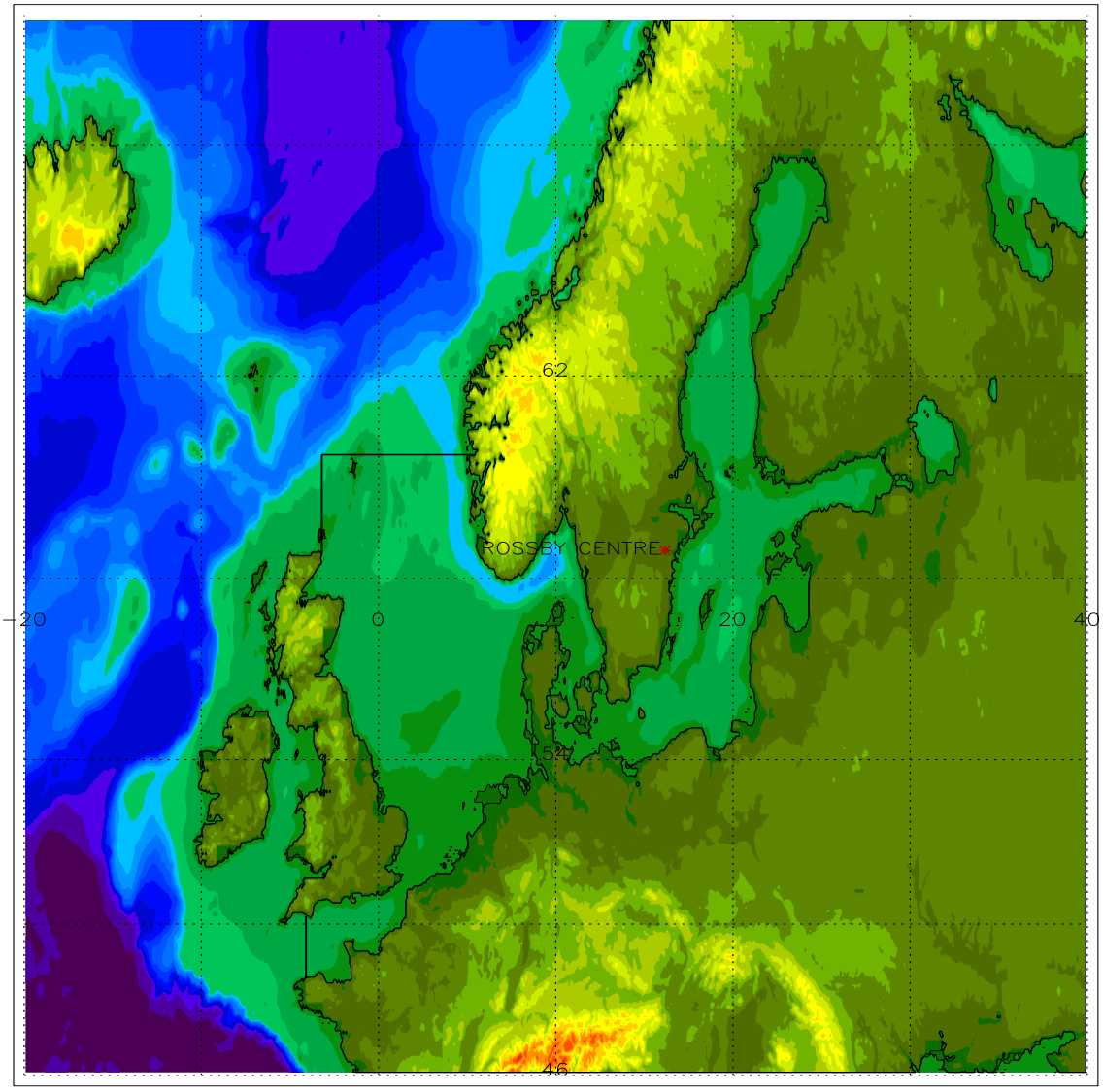

Figure 1: *The target model domain of RCO covers the whole North Sea and the Baltic Sea.*

Elken (1982). As the relation between eddy and mean transports are unknown yet, an eddy permitting model is desirable.

Hence, we have chosen a model resolution of 2 nautical miles in horizontal direction as a compromise ($\Delta\phi = 2'$, $\Delta\lambda = 4'$). In vertical direction the model makes use of 41 levels with layer thicknesses from $3\,m$ close to the surface to $12\,m$ near the bottom. The maximum depth in RCO version 1.0 is $250\,m$. The vertical distribution of levels is shown in Fig.2. For comparison the vertical grid of the coupled Kiel Baltic Sea model is shown (Hagedorn et al., 1999). Our higher resolution, even close to the bottom, is beneficial for representing deep water overflows between the Baltic sub-basins.

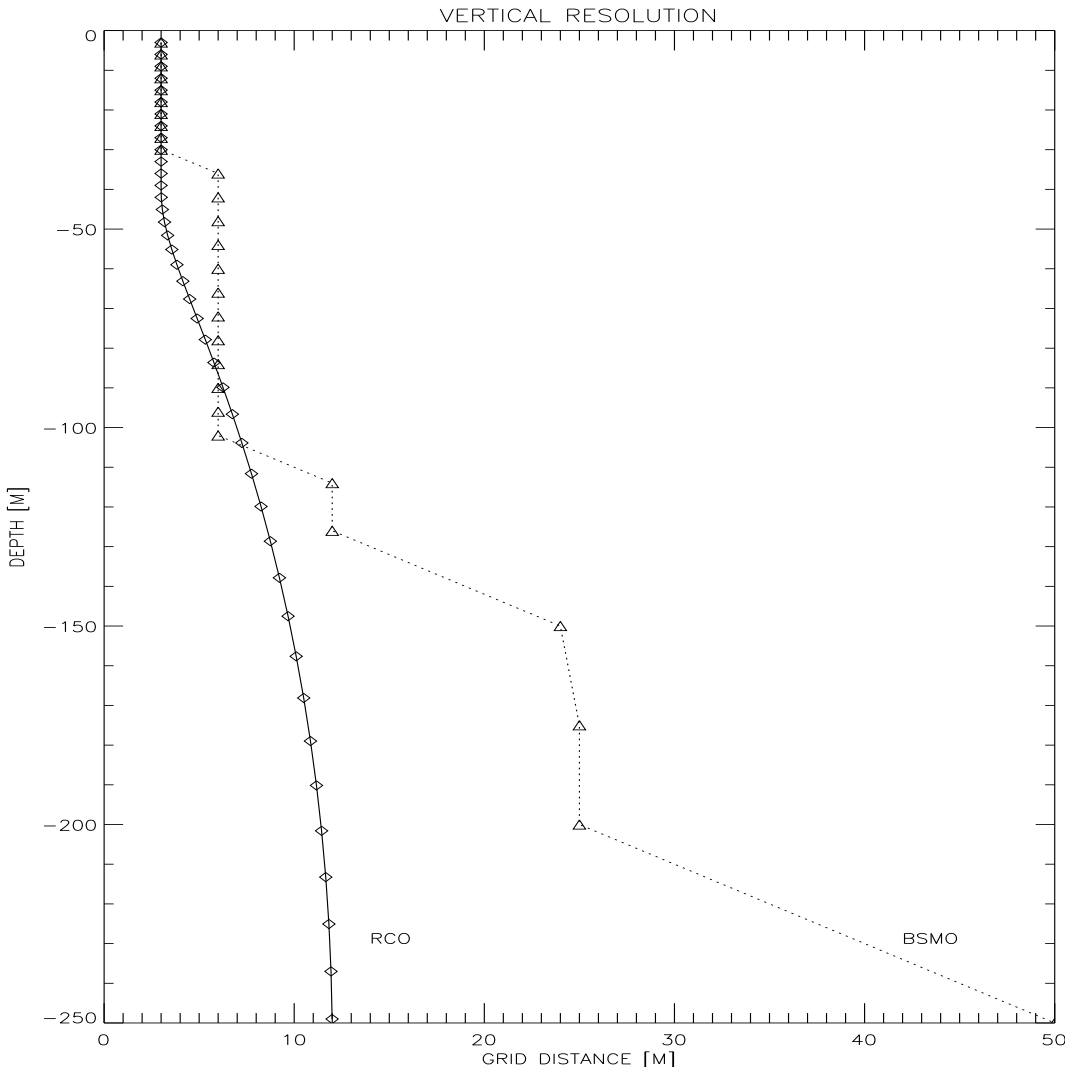

Figure 2: *Vertical resolution of RCO and the Kiel Baltic Sea model (BSMO) as used by Hagedorn et al. (1999).*

Due to the computational burden a course version with horizontal resolution of 6 nautical miles has been used additionally (see results of the coupled ice-ocean model in Section 5.7).

2.6 Bottom topography

The model depths are based on realistic bottom topography data (Seifert and Kayser, 1995) as shown in Fig.3. Seifert and Kayser (1995) compiled a high resolution grid topography of the Baltic Sea east of $9^o E$. The Belt Sea was sampled with a resolution of $\Delta\phi = 0.5'$ and $\Delta\lambda = 1'$ ($\approx 1\,km$) in steps of $1\,m$, the remaining parts of the Baltic Sea with $\Delta\phi = 1'$ and $\Delta\lambda = 2'$ ($\approx 2\,km$) in steps of $1\,m$ in the depth range $1\,m$ - $50\,m$, of $5\,m$ in the depth range $50\,m$ - $150\,m$ and of $10\,m$ for depths greater than $150\,m$. For RCO the data have been filtered and corrected by hand in the Danish Straits to ensure

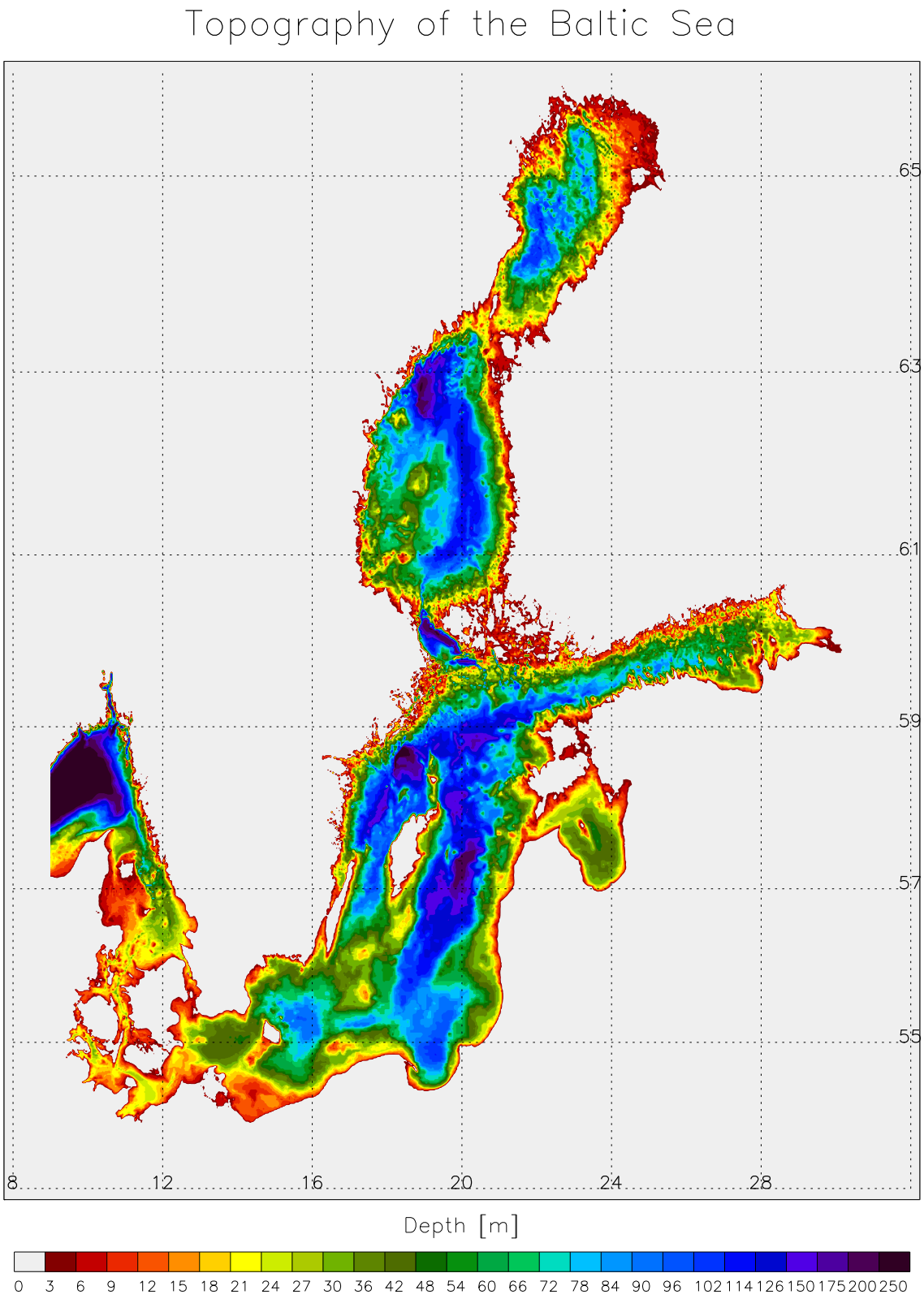

Figure 3: *Bottom topography of the Baltic Sea including Kattegat and Skagerrak (data from Seifert and Kayser, 1995).*

observed strait cross sections. All model grid points are connected to each other via advective horizontal or vertical transports on the Arakawa B-grid.

2.7 Open boundary conditions

2.7.1 Overview

One of the most important and most problematic aspects of regional ocean models is the open boundary conditions, connecting the model area to the open sea. The first requirement on these conditions is that they must be numerically stable. Even this is nontrivial: it is well known that seemingly reasonable numerical boundary conditions may destabilize otherwise stable finite difference schemes. The second requirement is accuracy: a signal (for example a tidal wave or a Kelvin wave, or an advected temperature anomaly) propagating outward should not be artificially reflected at the open boundary. Likewise, in the case of active boundary conditions (with time dependent data outside the model domain), signals propagating inward from the open sea should be allowed to enter the model domain.

In a test version of RCO used in this section, the open boundary is a north-south line in Skagerrak, from southern Norway to northern Denmark. It is intended that in the climate runs the temperature and salinity fields will be provided by a global ocean model and the sea surface height (SSH) from a storm surge model. In the test runs described below, the value of SSH was taken from hourly tide gauge measurements at Smögen, a Swedish station in Skagerrak. In order to model the inflows through the Danish Straits accurately, it is essential that incoming waves from the North Sea are generated correctly by the active boundary conditions.

In the near future, we intend to include the North Sea in the model area. The open boundaries to the North Atlantic Ocean will then be much longer than in the present version of the model, and the importance of the open boundary conditions even greater.

The time step and the basic numerical scheme in the model are very different for the baroclinic (three-dimensional) and the barotropic (two-dimensional) variables. Hence, the open boundary conditions are also different. The boundary conditions implemented for the baroclinic variables are the same as those proposed by Stevens (1990, 1991), and later used by several other authors (e.g., Meier and Krauß, 1994; Meier, 1996). Briefly, this means that the tracer fields at the boundary are relaxed toward prescribed values for inflow, while a radiation condition is used for outflow. The baroclinic velocity at the boundary is calculated from the linearized equation of motion, neglecting advection and calculating the diffusion term by simple extrapolation. (This will keep the velocity close to geostrophic.)

The barotropic boundary conditions proposed by Stevens cannot be used, since his model employed a streamfunction formulation, in contrast to our formulation with a free surface. In the present model the SSH is relaxed toward the prescribed value at

the boundary, following a normal time-step calculated by extrapolating the velocities.

Distinct sponge zones are used for the baroclinic and barotropic variables. In the baroclinic one enhanced diffusion and viscosity coefficients may be used. In the barotropic sponge zone the SSH is relaxed toward the prescribed boundary value, and a nonzero barotropic viscosity may be used.

2.7.2 Baroclinic fields

For simplicity we only consider a western boundary, and use Cartesian coordinates in the equations below (actually spherical coordinates are used in the model).

At outflow, the radiation condition for a tracer T (temperature or salinity) proposed by Stevens is

$$\frac{\partial T}{\partial t} + (u + c_T)\frac{\partial T}{\partial x} = \frac{\nu_t}{\sigma_t}\frac{\partial^2 T}{\partial z^2} + A_T \nabla^2 T. \tag{56}$$

Here u is the advection velocity, while c_T is a correcting phase speed which is calculated numerically from the finite difference form of the equation

$$\frac{\partial T}{\partial t} + c_T \frac{\partial T}{\partial x} = 0, \tag{57}$$

at points adjacent to the boundary at the previous timestep. The two velocities u and c_T in Eq.(56) reflect two different physical mechanisms by which a tracer signal may reach the boundary: by advection of a tracer anomaly, or by an internal wave, which has a signature in the tracer fields.

With the boundary at $i = 1$, the finite difference form of Eq.(56) is

$$\frac{T^{n+1}_{1,j,k} - T^n_{1,j,k}}{\Delta t} = -(u^{*n}_{j,k} + c^n_{Tj,k})\frac{T^n_{2,j,k} - T^n_{1,j,k}}{\Delta x} + F^{n-1}_{1,j,k}, \tag{58}$$

where $F^{n-1}_{1,j,k}$ is the usual second order diffusion term calculated as in the interior region, with the tracer value in the point outside the boundary given by extrapolation (i.e. effectively setting $T^n_{0,j,k} = T^n_{1,j,k}$). The biharmonic diffusion term as part of the advanced advection scheme (Section 2.8) which is used in the interior is dropped at the boundary points. With the B-grid used in the model, the advecting velocity at a western boundary point is taken as $u^{*n}_{j,k} = (u^n_{1,j,k} + u^n_{1,j-1,k})/2$ if negative, otherwise $u^{*n}_{j,k} = 0$. The correcting phase speed is given by

$$c^n_{Tj,k} = -\frac{\Delta x}{\Delta t}\frac{T^n_{2,j,k} - T^{n-1}_{2,j,k}}{T^n_{3,j,k} - T^n_{2,j,k}} \tag{59}$$

for $-\Delta x/\Delta t \le c^n_{Tj,k} \le 0$, with $c^n_{Tj,k}$ set to its bounds if these are exceeded by the expression (59).

Equation (58) is used if $u^{*n}_{j,k} + c^n_{Tj,k} < 0$ ("outflow"). In the opposite case, at "inflow", the tracer is relaxed toward the prescribed boundary value T_b:

$$T^{n+1}_{1,j,k} = T^n_{1,j,k} + \alpha(T_b - T^n_{1,j,k}) \tag{60}$$

where α is a suitable relaxation constant.

The momentum equations are linearized at the open boundary:

$$\frac{\partial u}{\partial t} - fv = -\frac{1}{\rho_0}\frac{\partial p}{\partial x} + \nu_t \frac{\partial^2 u}{\partial z^2} + A_M \nabla^2 u, \tag{61}$$

$$\frac{\partial v}{\partial t} + fu = -\frac{1}{\rho_0}\frac{\partial p}{\partial y} + \nu_t \frac{\partial^2 v}{\partial z^2} + A_M \nabla^2 v. \tag{62}$$

This keeps the velocity close to geostrophic, which makes it consistent with the density field. Since the last u-point at the open boundary is inside the last T-point (where the pressure is defined), the pressure term in Eq.(61) can be calculated as in the interior. The velocity in the first point outside the boundary, which is needed for the horizontal diffusion term, is obtained by extrapolation, similarly as for the tracer calculation. Again, the biharmonic diffusion term used in the interior is dropped at the boundary points.

Inside the open boundary there is a baroclinic sponge zone, whose width is typically set to about five or ten grid points. In this zone, the ambient horizontal diffusion coefficients A_T and A_M are multiplied by enhancement factors that taper off linearly toward the interior. This is done in order to stabilize the scheme and remove unwanted reflections at the boundary.

2.7.3 Barotropic fields

In general, we have found that the barotropic boundary conditions, in particular the active ones, easily cause numerical instabilities. Stevens used the Sverdrup balance to obtain an active boundary condition for the barotropic streamfunction (Stevens, 1990), but this can obviously not be done in a regional model with a free surface. A radiation condition has been used by Stevens for the barotropic streamfunction in the passive case, and by Mutzke (1998) for the free surface in a similar model as the present one. We have also tried a radiation condition for the free surface, but found that this is unstable.

The basic equations used for the barotropic variables $\zeta, \bar{u}$ and $\bar{v}$ in the model are the linearized shallow water equations:

$$\frac{\partial \zeta}{\partial t} + \frac{\partial}{\partial x}(H\bar{u}) + \frac{\partial}{\partial y}(H\bar{v}) = 0, \tag{63}$$

$$\frac{\partial \bar{u}}{\partial t} - f\bar{v} = -g\frac{\partial \zeta}{\partial x} + F_x, \tag{64}$$

$$\frac{\partial \bar{v}}{\partial t} + f\bar{u} = -g\frac{\partial \zeta}{\partial y} + F_y, \tag{65}$$

where H is the equilibrium depth (defined by the topography) and F_x and F_y are forcing terms which include the vertically averaged influence from the baroclinic fields. (They are thus constant during a baroclinic time step.) These equations are solved using a

leapfrog scheme, with a semi-implicit treatment of the Coriolis terms. In addition to this, a smoothing spatial filter is added to the calculation of ζ at a few selected time steps, in order to avoid a chequerboard pattern.

The outermost u-points at the open boundary, where $\bar{u}$ and $\bar{v}$ are defined, are inside the outermost T-points, where ζ is defined. Hence, the velocities $\bar{u}$ and $\bar{v}$ at these points can be calculated using the same scheme as in the interior region without supplying any extra information.

To calculate ζ at the boundary, on the other hand, the velocities in the first point outside the boundary are needed. They are defined by extrapolation, which in effect means that only the velocity component parallel to the boundary contributes in Eq.(63). In addition, a relaxation term toward the prescribed boundary value ζ_b is included in this equation. The finite difference form of the condition at a western boundary at $i = 1$ is thus

$$\frac{\zeta^* - \zeta^{n-1}_{1,j,k}}{2\Delta t} = \frac{H_{1,j,k}\bar{v}^n_{1,j,k} - H_{1,j-1,k}\bar{v}^n_{1,j-1,k}}{\Delta y}, \tag{66}$$

and

$$\zeta^{n+1}_{1,j,k} = \zeta^* + \beta(\zeta_b - \zeta^*), \tag{67}$$

where $\beta \leq 1$ is a suitable positive relaxation constant.

If $\beta = 1$, ζ is simply set equal to ζ_b at the boundary, and the extrapolation has no effect. No wave can then propagate across the boundary, and all incident waves are totally reflected. (With $\zeta_b = 0$, this is the appropriate boundary condition between a shelf and an infinitely deep open sea.) Furthermore, with a time-dependent ζ_b, it has been seen that numerical instabilities appear. (Typically, the vertical velocity exceeds the CFL limit near the point where the open boundary and the coast meet. Thus, it may not be a purely barotropic instability in the sense that the barotropic mode is self-amplifying; the problem is rather that its amplitude gets too large in some points.)

If, on the other hand, $\beta = 0$, the value of ζ_b is not felt at all, and we in effect have a passive boundary condition corresponding to $\partial\bar{u}/\partial x = 0$ and $\partial\bar{v}/\partial x = 0$ in the continuum limit. For a plane wave at normal incidence to the boundary, this is equivalent to setting $\beta = 1$ and $\zeta_b = 0$, and such a wave is totally reflected. On the other hand, wave propagation along the boundary is now possible, and waves incident at an oblique angle should therefore be less than totally reflected.

We have examined two ways of stabilizing the active boundary condition, both employing a barotropic sponge zone. The first method is to use the relaxation procedure in Eq.(67) not just at the boundary, but in the whole sponge zone, with a relaxation constant β that tapers off to zero inward.

The second method is to introduce a viscous term $0.5A_{bt}f(\Delta x)^2\nabla^2\bar{u}$ in Eq.(64) in the sponge zone, and similarly in Eq.(65). (Otherwise, the leapfrog scheme is inviscid except for the filtering done in selected time steps.) The viscosity coefficient A_{bt} is defined

in such a way that $A_{bt} = 0.25$ gives a characteristic damping time of one inertial period for grid scale noise. (That is, with this value the real and imaginary parts of the eigenfrequency of the "computational inertial mode" are equal.) The viscosity constant A_{bt} tapers off to zero inward in the sponge zone.

Extensive tests of the barotropic boundary condition have been made with a course resolution version of the model, $\Delta x = 0.18$ degrees and $\Delta y = 0.09$ degrees. This version of the model had a simplified topography truncated at the depth $250\,m$ near the open boundary in Skagerrak. Tests with higher resolution and a realistic topography are underway. The baroclinic timestep was $300\,s$, and the barotropic one $15\,s$.

Two different sets of initial fields were used, the first one with realistic vertical temperature and salinity profiles, and the second one with constant salinity and a simplified temperature profile based on a zonally averaged Levitus climatology. The time-dependent value ζ_b used at the boundary was either taken as sinusoidally varying with amplitude $50\,cm$ and period 12 hours, or else defined from tide gauge measurements at Smögen, in particular from January 1993, when the SSH variability was unusually large. Linear interpolation in time was done between the hourly measurements. No meteorological forcing was applied at the sea surface.

In all tests the model was run for at least 8 days (if possible), and in some cases for 30 or 90 days. With a sinusoidal SSH variation at the boundary, the numerical instability always occurred during the first two days.

If the SSH at the boundary was directly prescribed (i.e. $\beta = 1$) and no sponge zone was employed, numerical instability occurred with all combinations of initial fields and SSH variation, except with the simple initial profiles based on Levitus' climatology and a sinusoidal SSH variation. The width of the sponge zone was then set to five grid points, and a number runs performed with different values of the relaxation coefficient β and the barotropic viscosity coefficient A_{bt}.

In all cases, a value of $\beta = 0.5$ was found to be small enough to stabilize the model. This value is perhaps surprisingly large, and in fact gives a very stiff relaxation, with a timescale of only two barotropic time steps. Thus, on the scale of one baroclinic time step this is practically equivalent to a direct prescription of the boundary SSH.

The model could also be stabilized by a nonzero barotropic viscosity in the sponge zone. (In this case we used $\beta = 1$ and no relaxation in the sponge zone.) When using realistic initial profiles, it was found that a value of $A_{bt} = 0.4$ at the boundary was needed for stability with a sinusoidally varying SSH, while $A_{bt} = 0.8$ was needed with the Smögen data. With the simple initial profiles based on Levitus' climatology combined with Smögen data for the SSH, $A_{bt} = 0.4$ at the boundary was necessary.

Our tentative conclusion is that relaxing the SSH in a sponge zone is the most efficient way of stabilizing the boundary condition. While it is also possible to use barotropic viscosity, the value of the viscosity coefficient needed depends more on the situation,

and is rather large.

2.7.4 Implementation of open boundaries in RCO 1.0

The open boundary conditions described in the previous sections have been implemented in RCO version 1.0, i.e., the model border is located in the northern Kattegat on the same latitude as the Danish city Frederikshavn. Sea level, temperature and salinity data need to be specified at the boundary.

Hourly sea level data from the tide gauges Frederikshavn and Ringhals (Varberg) are prescribed. For the results in Section 5 the mean of 1992/1993 has been subtracted from each time series and replaced by the geodetic solution from Ekman and Mäkinen (1996), i.e., $\bar{\zeta_F} = -11.1$ for Frederikshavn and $\bar{\zeta_R} = -1.4$ for Ringhals. In addition, the sea level data have been lowpass filtered to eliminate the semi-diurnal and diurnal tides. Only in Kattegat, Danish Straits and Belt Sea the tidal signal is important with amplitudes of $10\,cm$ (Maagard and Rheinheimer, 1974). In the interior of the Baltic Sea the tidal signal can be neglected. The sea level elevation between the two tide gauge stations have been linear interpolated.

From the Swedish Ocean Archive SHARK (Svenskt HavsARKiv, SMHI) temperature and salinity profiles from the open sea monitoring station Anholt East in the Kattegat ($56^oN\,40.0^{'}$, $12^oE\,7.0^{'}$, cf. Fig.5) have been extracted and mean profiles for the period 1980 until 1993 have been calculated. In the area of the model boundary the Skagerrak-Kattegat front is located with rapid changes of its position on daily timescales (Jakobsen, 1997). Due to the lack of data resolving the northern Kattegat hydrography the mean profiles are used as open boundary conditions. Hence, it is obvious that the model will not perform very well in the Kattegat. The sensitivity of the model interior in dependence of the salinity profiles used for the open boundary conditions are shown in Section 5.

2.8 Advection scheme

Earlier versions of the Bryan-Cox-Semtner ocean model had a problem in the advection scheme. Approximations involved in deriving the finite-difference momentum equation lead to an error in the estimated vertical flux of momentum. The error is largest in features that are only just resolved by the model grid and the magnitude of the largest error increases as the grid size is reduced. As a result, in ocean models like RCO that are just eddy resolving, the error can have a significant effect on the overall balance of momentum. Webb (1995) presented an improved finite-difference scheme that greatly reduces the error. The scheme is implemented in OCCAM and RCO.

Leonard's widely used QUICK advection scheme (Leonard, 1979) is , like the Bryan-Cox-Semtner ocean model, based on a control volume form of the advection equation. Unfortunately, in its normal form it cannot be used with the leapfrog-Euler forward

time-stepping schemes used by the ocean model. Farrow and Stevens (1995) overcame the problem by implementing a predictor-corrector time-stepping scheme with the drawback to be computationally expensive to run. Webb et al. (1998) showed that the problem can be overcome by splitting the QUICK operator into an $O(\delta x^2)$ advective term and a velocity dependent biharmonic diffusion term. These can then be time-stepped using the combined leapfrog and Euler forward schemes of the Bryan-Cox-Semtner ocean model, leading to a significant increase in model efficiency. A small change in the advection operator coefficients leads to $O(\delta x^4)$ accuracy. The improved scheme is used in OCCAM and RCO.

2.9 Bottom friction

In the model unresolved bottom roughness is parameterized according to Cox (1984) using a second order law for bottom friction (Eq.(29)). As during the major inflow in January 1993 the accumulated transport through the Danish Straits into the Baltic is known from observations (e.g., Matthäus et al., 1993; Jakobsen, 1995), the bottom friction coefficient c_b can be determined comparing model and observed transports. Provided that the critical strait cross sections are correct Meier (1996) derived $c_b = 0.5 \cdot 10^{-3}$.

2.10 Horizontal friction

Horizontal viscosity and diffusivity are parameterized using a harmonic approach (Eq.(9) – (12)). The role of horizontal friction in high resolution Baltic Sea models is discussed by Meier (1996) who also tested scale dependent approaches like biharmonic friction or the Smagorinsky scheme (Smagorinsky, 1963). We have tested different values for the constants A_M and A_H in the range $A_M = 5 \cdot 10^1 - 5 \cdot 10^3 m^2/s$ and $A_H = 1 \cdot 10^1 - 5 \cdot 10^2 m^2/s$. For 10 year runs it is important to choose diffusivity as small as possible. Minimum values for horizontal friction are necessary to ensure numerical stability of the explicit discretization scheme.

2.11 Turbulence model

2.11.1 Equations for turbulent kinetic energy and dissipation

As shown by Baumert et al. (1997), the two commonly used second moment turbulence closures, the $k-\epsilon$ (Svensson, 1978; Rodi, 1993) and the $k-l$ model (Mellor and Yamada, 1982), can be written in a canonical presentation. Despite the parameterization of the interaction of turbulence and stratification, the two model types behave rather similar. It is decided to use the $k-\epsilon$ model. Additionally, two prognostic equations for turbulent kinetic energy (TKE) and for dissipation of TKE has to be solved at every grid point

of the three-dimensional model:

$$\frac{\partial k}{\partial t} - \frac{\partial}{\partial z}\left(\frac{\nu_t}{\sigma_k}\,\frac{\partial k}{\partial z}\right) = P + G - \epsilon\,, \tag{68}$$

$$\frac{\partial \epsilon}{\partial t} - \frac{\partial}{\partial z}\left(\frac{\nu_t}{\sigma_\epsilon}\,\frac{\partial \epsilon}{\partial z}\right) = c_{\epsilon 1}\,\frac{\epsilon}{k}\,\left(P + c_{\epsilon 3}\,G\right) - c_{\epsilon 2}\,\frac{\epsilon^2}{k}\,, \tag{69}$$

$$\text{with}\quad P = \nu_t\,\left[\left(\frac{\partial u}{\partial z}\right)^2 + \left(\frac{\partial v}{\partial z}\right)^2\right], \quad G = -\frac{\nu_t}{\sigma_t}\,N^2\,, \tag{70}$$

$$\nu_t = c_\mu\,\frac{k^2}{\epsilon}\,. \tag{71}$$

Here, k denotes TKE, ϵ dissipation of TKE, ν_t the turbulent friction coefficient, u and v horizontal velocity components and N the Brunt-Väisälä frequency. The constants are given in Table 1 according to Rodi (1993). In case of unstable stratification the constant $c_{\epsilon 3}$ is set equal to 1 to ensure complete mixing between adjacent grid boxes.

c_μ	$c_{\epsilon 1}$	$c_{\epsilon 2}$	$c_{\epsilon 3}$	σ_k	σ_ϵ
0.09	1.44	1.92	0	1	1.3

Table 1: *Constants of the $k-\epsilon$ model (Rodi, 1993).*

The turbulence model gives no information about the turbulent Prandtl number σ_t so that an empirical formula has to be used to complete the mixing scheme. In several experiments we get the best results using a Richardson number dependent Prandtl number (Blanke and Delecluse, 1993).

$$\sigma_t = \begin{cases} 1 & : \quad Ri \le 0.2 \\ 5\,Ri & : \quad 0.2 < Ri \le 2 \\ 10 & : \quad 2 < Ri \end{cases}\,. \tag{72}$$

Here Ri denotes the gradient Richardson number. A constant turbulent Prandtl number results in a too strong erosion of the halocline. It turned out that probably the greatest problems of the $k-\epsilon$ model are related to the unknown turbulent Prandtl number and the unknown constant $c_{\epsilon 3}$ (see also Burchard and Baumert, 1995). More details are given by Meier (1999).

2.11.2 Surface flux boundary conditions for the $k-\epsilon$ model

Commonly, Dirichlet boundary conditions are used for the $k-\epsilon$ turbulence model. At the surface a logarithmic boundary layer is assumed with balance between shear production P and dissipation ϵ (Svensson, 1978):

$$P + G \stackrel{!}{=} \epsilon, \quad l \stackrel{!}{=} \kappa\,(z_0 - z) \tag{73}$$

with von Kármán's constant κ and roughness length z_0 (the exclamation marks indicate that above equalities are assumed to be valid). In case of high vertical resolution these boundary conditions are only slightly dependent on the surface roughness length. Within the boundary layer dissipation decays inversely proportional with the distance from the surface. Contrary, measurements show that dissipation decays much faster with the second or third power (see Craig and Banner, 1994; Craig, 1996). Due to breaking surface gravity waves a turbulence enhanced layer is developed which controls the vertical flux of TKE from the wave field to the mixed layer interior. Therefore flux boundary conditions are included which are calculated from an analytical solution of the TKE equation basing on the assumption of a balance of TKE diffusion and dissipation (Craig and Banner, 1994):

$$\frac{\partial}{\partial z}\left(\frac{\nu_t}{\sigma_k}\frac{\partial k}{\partial z}\right) \stackrel{!}{=} \epsilon, \quad l \stackrel{!}{=} \kappa\,(z_0 - z) \quad . \tag{74}$$

From the assumed balance (74) the following flux boundary conditions are derived:

$$\left.\frac{\nu_t}{\sigma_k}\,\frac{\partial k}{\partial z}\right|_{z=-\frac{\Delta z}{2}} = \frac{m\,u_\star^3 + \kappa\,z_0\,B_0}{\left(1+\frac{\Delta z}{2\,z_0}\right)^n} \quad , \tag{75}$$

$$\left.\frac{\nu_t}{\sigma_\epsilon}\,\frac{\partial \epsilon}{\partial z}\right|_{z=-\frac{\Delta z}{2}} = a_\epsilon\,\frac{\left(m\,u_\star^3 + \kappa\,z_0\,B_0\right)^{\frac{4}{3}}}{z_0\,\left(1+\frac{\Delta z}{2\,z_0}\right)^{\frac{4\,n}{3}+1}} \tag{76}$$

with

$$n = \sqrt{\frac{3}{2}\,\frac{\sigma_k}{c_\mu}}\,\frac{c_d}{\kappa} \tag{77}$$

and $c_d = 0.16$. The value of the constant a_ϵ is given by

$$a_\epsilon = \frac{c_\mu^{\frac{1}{3}}}{\sigma_\epsilon}\left(\frac{3\,\sigma_k}{4}\right)^{\frac{2}{3}}\left(\sqrt{\frac{3\,\sigma_k}{c_\mu}}\,\frac{c_d}{\kappa}+1\right) \quad . \tag{78}$$

Further, $u_\star$ is friction velocity, B_0 surface buoyancy flux, $m = 100$ a constant given by Craig and Banner (1994) and $\Delta z = 3\,m$ is the vertical grid distance. The surface roughness length is calculated from Charnock's formula (Charnock, 1955):

$$z_0 = \alpha\,\frac{u_\star^2}{g} \tag{79}$$

with $\alpha = 1400$ (Ly, 1990). In case of sea ice $u_\star$ is not calculated from wind stress but from the corresponding ice-ocean stress (Equation (131)).

It has been shown that the results of the $k-\epsilon$ model converge towards the approximate solution from which the flux boundary conditions are calculated. The depth of the turbulence enhanced surface layer depends only from the roughness length. The approach of the here derived flux boundary conditions makes only sense as long as the depth of the turbulence enhanced surface layer is larger than $\Delta z/2$, i.e., $z_0 > 35\,cm$ if

$\Delta z = 3\,m$.

It turned out that the main difference between Dirichlet and Neumann (or flux) boundary conditions is the dependence on the surface roughness length in the range between $10\,cm$ up to $1\,m$. In case of flux boundary conditions the friction coefficients are much more sensitive against changes of the roughness length than in case of Dirichlet boundary conditions.

2.12 Initial conditions

For the calculation of initial temperature and salinity fields the model domain has been divided into 14 boxes. The borders have been chosen according to topographic features which determine the hydrography of the sub-basins. These sub-basins are comparable to the boxes of Omstedt's model (1990) and shown in Fig.4. Temperature and salinity

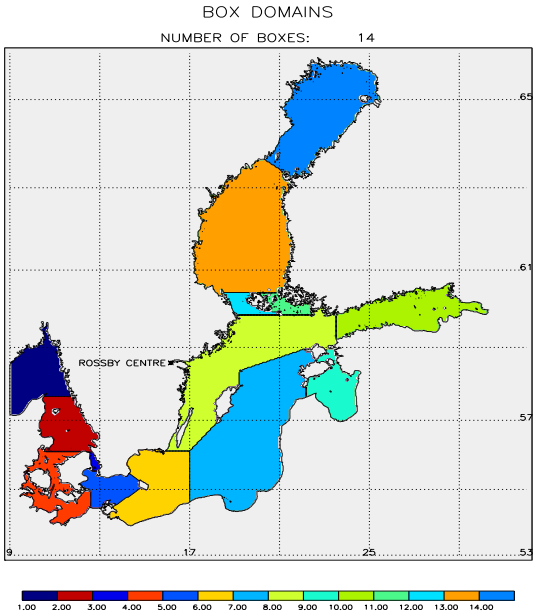

Figure 4: *Division of the Baltic Sea into sub-basins for the calculation of initial fields for temperature and salinity.*

profiles from the SHARK data base (Svenskt HavsARKiv, SMHI) have been selected to compile initial conditions for May 18, 1992. Single profiles of temperature and salinity observed closest to the chosen date have been attached to each sub-basin. This method ensures an unsmoothed vertical density structure. In Fig.5 the positions of 29 available open sea monitoring stations of the SHARK data base are shown. May 18 was selected because around this date most of the boxes could be filled up with data. Tab.2 lists sub-basins and corresponding profiles.

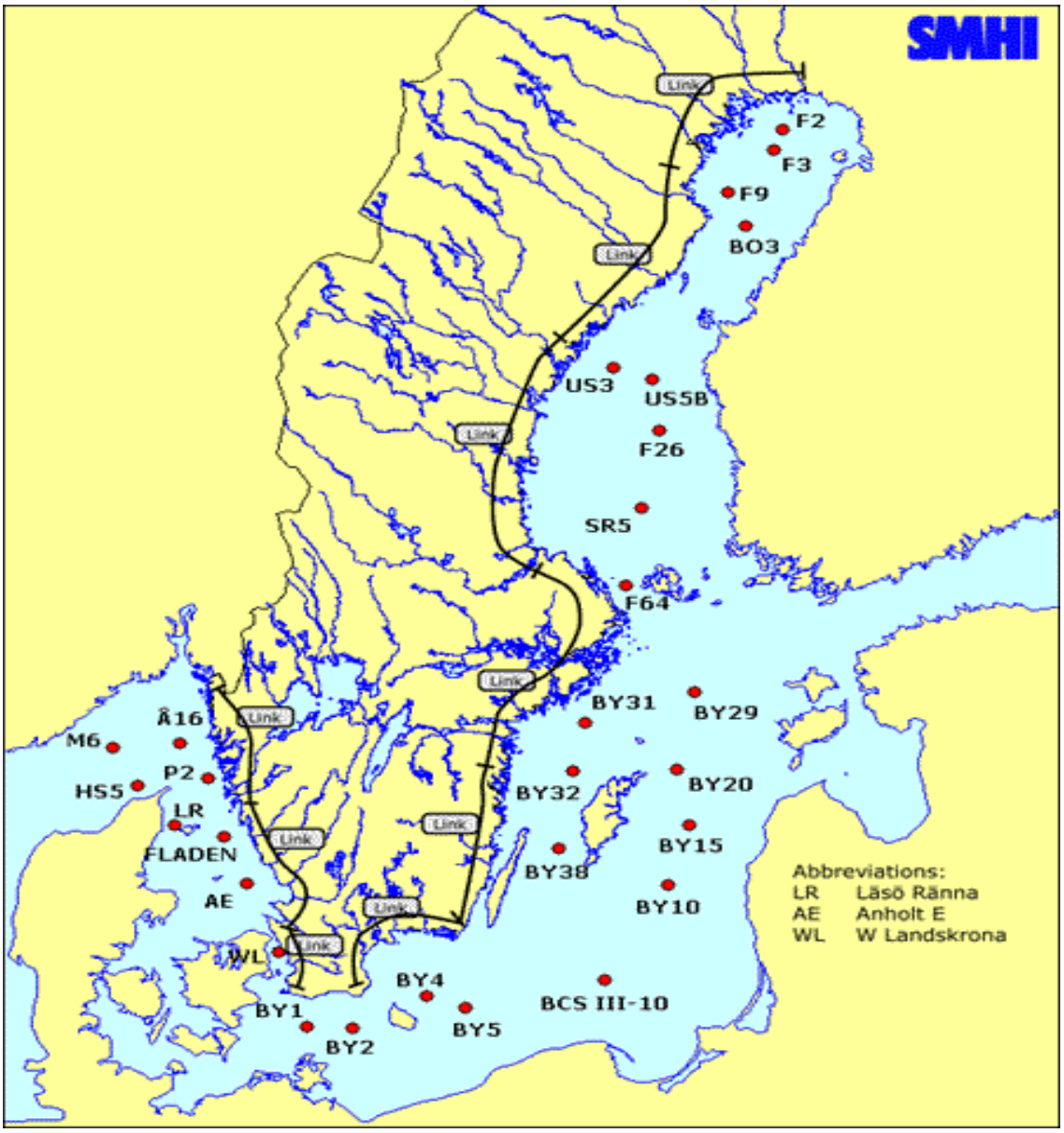

Figure 5: *Positions of selected open sea monitoring stations of the SHARK data base (Svenskt HavsARKiv, SMHI).*

The initialization of models is quite often a problem because observations are missing and the model results depend crucially on initial conditions. The strategy employed here is simple and not applicable for integration periods shorter than the horizontal advective timescale. However, for multi-year model studies it is more important to start with correct initial vertical stratification within each sub-basin than with correct initial horizontal gradients. The vertical salinity distribution in the Baltic Sea changes with diffusive timescale if there are no salt water inflows. The diffusive timescale of the order of decades is much longer than the advective timescale of the order of weeks to months. Hence, a spin-up integration of 3 months should be more than sufficient to smooth out unrealistic sharp gradients in the horizontal without changing vertical

Nr.	Sub-basin	Station	Date	Comment
1	Skagerrak	M6	19920505	not used in RCO 1.0
2	Kattegat	Anholt East	19920518	
3	Öresund	Western Landskrona	19920519	
4	Belt Sea	Great Belt	no data	initialized as Öresund
5	Arkona Basin	BY2	19920519	
6	Bornholm Basin	BY5 (Bornholm Deep)	19920520	
7	Eastern Gotland Basin	BY15 (Gotland Deep)	19920521	
8	Northwestern Gotland Basin	BY31 (Landsort Deep)	19920519	
9	Gulf of Riga		19920525	not from SHARK
10	Gulf of Finland	LL07	19890507	not from SHARK
11	Archipelago Sea		no data	initialized as Åland Sea
12	Åland Sea	F64	19920523	
13	Bothnian Sea	SR05	19920524	
14	Bothnian Bay	F9	19920527	

Table 2: *Sub-basins, corresponding monitoring stations and observations times.*

gradients. The results in Section 5 show that this strategy is justified. Due to the high variability of salt water inflows (Matthäus and Frank, 1992) and river discharge (Bergström and Carlsson, 1994) the Baltic Sea is never in steady state and usually far from its mean. Hence, climatologies (Bock, 1971; Lenz, 1971; Janssen et al., 1999) are unsuitable as starting fields for 10 year integrations.

2.13 Atmospheric forcing

The atmospheric forcing data are three hourly maps for sea level pressure $[Pa]$, geostrophic wind components $[m/s]$, air temperature in $2\,m$ height $[°C]$, relative humidity in $2\,m$ height [%] and total cloud cover [%] from the SMHI data base (Lars Meuller, pers. comm.). In addition, at 06 and $18\,UTC$ also 12 hourly accumulated precipitation $[mm]$ is used. If no precipitation data are available, climatological areal estimates (1951-1970) from Dahlström (1986) have been used. The SMHI data base is available from 1979 onwards and is updated regularly. The horizontal resolution is one degree and the grid is not rotated. The maps cover the latitudinal range $49.5°\,N - 71.5°\,N$ and the longitudinal range $7.5°\,E - 39.5°\,E$.

As only geostrophic wind fields are available a boundary layer parameterization has to be used to calculate wind speeds in $10\,m$ height. According to Karger (1995) and Bumke (1997, pers.comm.) the dependence of the reduction coefficient from the distance to the coast has to be taken into account. They correlated the ratio between geostrophic wind speeds and onshore and offshore wind speeds observed on trading ships in the Baltic Sea with the distance to the coast. Corresponding to land and open sea Karger (1995) calculated matrices of reduction coefficients in the range between

0.45 and 0.86. Improved analysis from Bumke (1997, pers.comm.) gave the range between 0.53 and 0.71. Here a simplified scheme has been implemented with coefficients varying independent of the wind direction linear between 0.5 at the coast and 0.7 for distances greater than 50 km. The wind mask used in RCO is shown in Fig.6. A con-

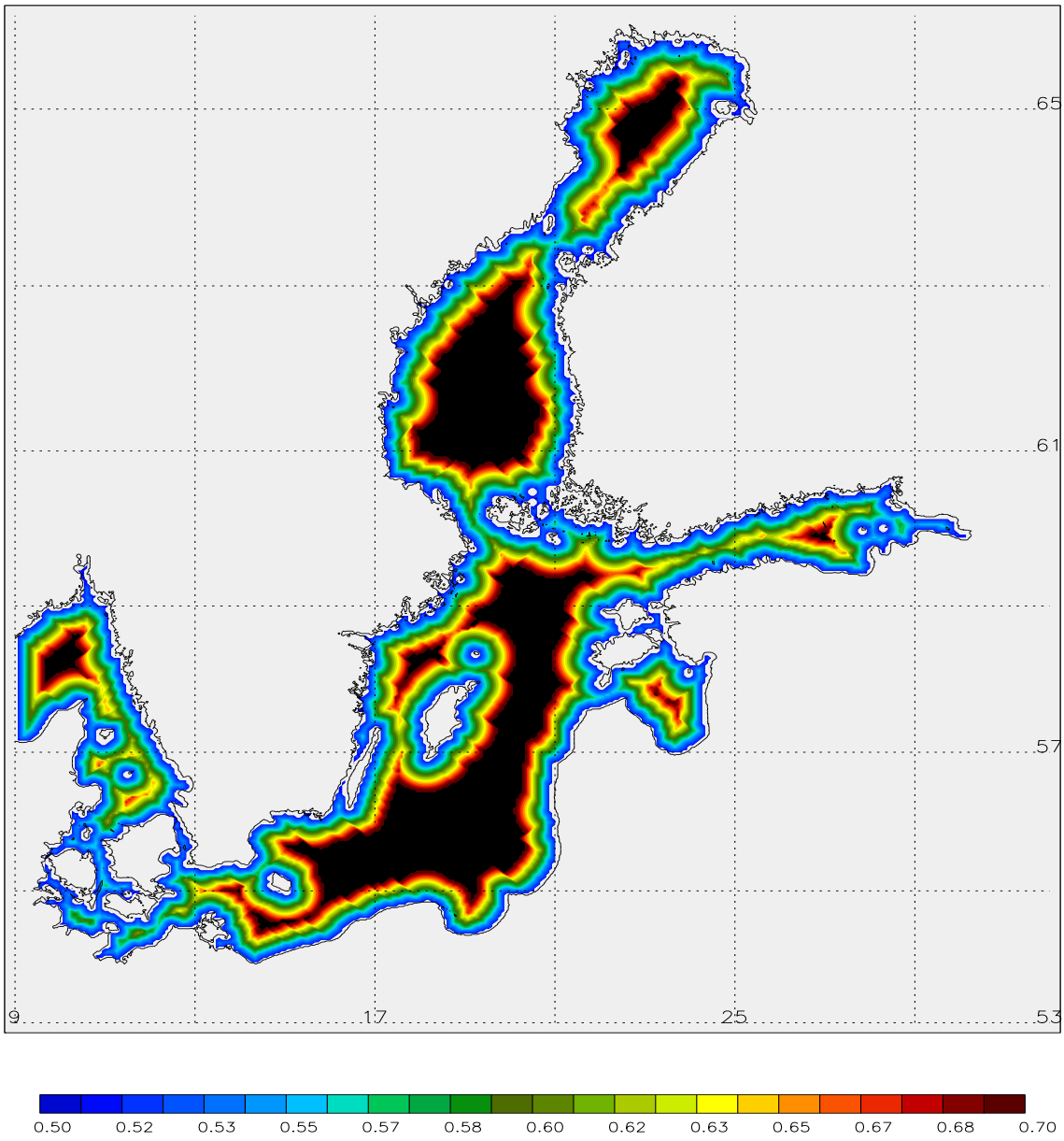

Figure 6: *Mask used for the calculation of* 10 m *wind speeds. The reduction coefficient is 0.7 in black areas.*

stant ageostrophic angle of 17 degrees has been used according to Bumke and Hasse (1989). Karger (1995) related the ageostrophic angle α to the stability $\Delta T = T_a - T_w$ and got the rather large value $\alpha = 25.5 + 1.7\,\Delta T$. Meier (1996) assimilated sea level data and measurements of surface wind fields from trading ships into a Baltic Sea model to optimize planetary boundary parameterization using a variational method based on the adjoint technique. He got as result 0.71 ± 0.02 for the reduction coefficient and

23.7 ± 0.5^o for the ageostrophic angle. It should be noted that the major shortcoming of the scheme used in RCO is probably the lack of stability dependency.

As the SMHI data base maps are not available for the North Sea and as the wind fields are only geostrophic wind speeds a new version of RCO is under preparation using ECMWF reanalysis data (ERA). Therefore, at the Rossby Centre surface data from the ERA period January 1980 until February 1994 covering the area $20^o N - 90^o N$, $90^o W - 90^o E$ with a resolution of 2.5 degree have been prepared (Anders Ullerstig, pers.comm.). The variables are surface pressure, surface temperature, temperature at $2\,m$, dewpoint temperature at $2\,m$, wind at $10\,m$, land/sea mask, precipition, latent heat flux, sensible heat flux, clouds (L, M, H) and total cloud cover.

2.14 River Runoff

2.14.1 Data

The river runoff data have been taken from the BHDC data base at SMHI (BALTEX Hydrological Data Centre). The data do not only represent the inflow by major rivers, but the runoff through coastal segments including also estimated smaller runoff ways. This data base is documented thoroughly by Bergström and Carlsson (1994). The period 1980 - 1993 is covered for RCO. The data base does not include Numedalslagen, a river in southern Norway. It has been added to the runoff data for RCO from the HIROMB data base.

For RCO we picked the 30 (31) most important coastal segments. They sum up to 13 864 $m^3 s^{-1}$ (14 464 $m^3 s^{-1}$ including Numedalslagen). The total observed contribution of river runoff to the Baltic Sea catchment area is 15 310 $m^3 s^{-1}$ for the period 1950 - 1990 (Bergström and Carlsson, 1994). However for the period 1982 - 1993, the total observed river runoff is 16 404 $m^3 s^{-1}$. As the last period is more relevant for the verification of RCO, the reference transport is taken from 1982 - 1993. 31 RCO rivers cover 85% of 17 404 $m^3 s^{-1}$ (16 404 + 600 (Numedalslagen)). The remaining 15% are distributed over the segments proportional to their mean transports by applying a factor $1/0.85 = 1.18$ to the volume transport. This ensures the supply of a correct amount of freshwater to the Baltic Sea including Kattegat and Skagerrak.

The coastal segments have been named after the biggest rivers within their range. Table 3 lists the segments together with its mean volume transports between 1980 and 1993. Transports differ from Bergström and Carlsson (1994) due to different time periods. The positions are visualized in Fig.7.

2.14.2 Implementation of River Runoff

RCO employs a free surface according to Killworth et al. (1991), e.g. the surface can freely move up and down as a result of continuity. This gives us the possibility to add the river runoff's volume per second on top of the existing water column. The

Nr.	Longitude	Latitude	Transport	Seg Nr	Name
1	30.13	59.95	2584	3003	NEVA
2	18.93	54.35	1026	7001	VISTULA
3	23.20	65.71	749	1001	KALIXAELVEN
4	24.00	57.05	728	3014	DAUGAVA (DAGUA)
5	17.53	62.41	653	1011	INDALSAELVEN
6	21.06	55.71	651	3016	NEMAN
7	22.06	65.45	603	1002	LULEAELVEN
8	11.73	57.65	600	1037	GOETAAELV
9	24.53	65.71	593	2101	KEMIJOKI
10	17.93	62.81	575	1010	ANGERMANAELVEN
11	14.26	53.95	517	7004	ODRA/ODER
12	20.33	63.65	502	1007	UMEAELVEN
13	28.00	59.45	453	3005	NARVA
14	17.40	60.65	442	1015	DALAELVEN
15	26.86	60.41	344	2129	KEMIJOKI
16	21.53	61.58	273	2117	KOKEMAEENJOKI
17	25.40	65.01	272	2105	OULUJOKI
18	17.20	61.18	258	1014	LJUSNAN
19	21.66	65.35	205	1003	PITEAELVEN
20	21.53	57.38	201	3015	VENTA
21	21.26	64.65	194	1005	SKELLEFTEAELVEN
22	18.66	59.35	186	1019	NORRSTROEM
23	19.86	54.61	179	3017	PREGOLIA
24	12.93	56.51	175	1034	LAGAN
25	25.26	65.28	175	2103	IIJOKI
26	10.46	57.08	165	9007	LIMFJORD
27	24.46	58.35	155	3011	PAERNU NAVESTI
28	23.86	56.98	146	3009	between DAUGAVA and VENTA
29	28.26	59.68	130	3004	LUGA
30	15.73	54.21	130	7003	PARSETA
31	10.06	58.98	600	0	NUMEDALSLAGEN

Table 3: *River segments from the BHDC data base with central positions, mean volume flux in $m^3 s^{-1}$ for 1980 - 1993, segment number and appendant names.*

prognostic equation for the sea surface elevation ζ is then given by

$$\frac{\partial \zeta}{\partial t} = -\frac{1}{R\cos\phi}\left[\frac{\partial U}{\partial \lambda} + \frac{\partial}{\partial \phi}\left(V\cos\phi\right)\right] + \left.\frac{\partial \zeta}{\partial t}\right|_{riv}, \tag{80}$$

$$\left.\frac{\partial \zeta}{\partial t}\right|_{riv} = \frac{F_{riv}}{a_{surf}} \tag{81}$$

whereby F_{riv} = river volume flux and a_{surf} = the area to which the extra surface lifting is applied. This is the surface area of a single ocean grid box at the coast.

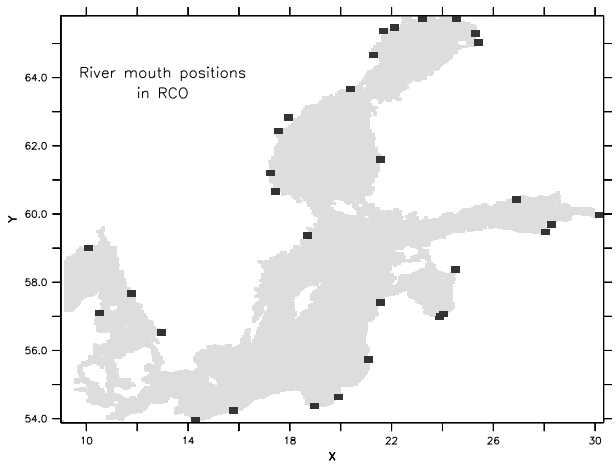

Figure 7: *Positions of the major rivers within a coastal runoff segment*

Since the free surface option requires a shorter timestep ($\triangle t_b$) then for the baroclinic mode ($\triangle t_c$), subcycling for the prognostic equation for ζ (Eq.80) is necessary. The additional river flux term has to be applied within that subcycling loop, otherwise the system would sense intermittent surface lifts only every $\triangle t_c/\triangle t_b$ timesteps. The signal would gradually vanish during the subcycling procedure.

For a river mouth in nature, the sea surface level increase comes along with input of momentum, heat and salinity. In RCO, input of momentum and heat are neglected. The temperature is assumed to be identical to the upper ocean temperature. The rivers are assumed to carry zero salinity. The new salinity S at each timestep is calculated as weighted mean of the already updated salinity ($S_{old} + \frac{\partial S}{\partial t}|_{no\_river} \triangle t$) before the river water addition, and zero salinity in the newly created upper part of the surface box:

$$S = \frac{(S_{old} + \frac{\partial S}{\partial t}|_{no\_river} \triangle t) \cdot (\Delta z + \zeta)}{\Delta z + \zeta + \triangle \zeta_{riv}} . \tag{82}$$

This is equivalent to a salinity change

$$\frac{\partial S}{\partial t} = \frac{\frac{\partial S}{\partial t}|_{no\_river} \cdot (\Delta z + \zeta) - \frac{\partial \zeta}{\partial t}|_{riv} \cdot S_{old}}{\Delta z + \zeta + \triangle \zeta_{riv}} \tag{83}$$

with thickness $\triangle \zeta_{riv}$ created by the runoff, Δz = thickness of upper level, ζ = surface elevation before application of river runoff and S_{old} is the salinity of the previous timestep. Eq.(82) and (83) describe the effects of advection, diffusion and increase of the surface grid box volume.

This implementation of rivers covers the dominant effects by adding freshwater to the water column. Numerical instabilities have not been encountered.

3 Sea ice model description

Modelling of the Baltic during wintertime relies on an adequate representation of sea ice. Sea ice affects atmosphere and ocean on both annual and climatological timescales. Compared to non-ice conditions, ice limits the fluxes of heat and freshwater. It also alters the energy budget of a coupled ocean-atmosphere system by changing the surface albedo drastically.

Dynamic-thermodynamic ice models of the Hibler-type have been applied to the Baltic successfully in recent years (e.g., Haapala and Leppäranta, 1996). These models employ the same viscous-plastic (VP) rheology as used in many global ocean-ice circulation models. An overview about ice dynamics is given by Leppäranta (1998). The VP rheology with it's typical numerical implementations is known to have a weakness in responding to quickly changing forcing fields (Hunke and Dukowicz, 1997). An extension of the VP rheology with an elastic component (EVP) , offers a solution to this problem. It also enables more strait forward and less troublesome numerics, particularly for a parallel computer architecture as the CRAY-T3E, which is the workhorse of the SWECLIM project.

A first version of the sea ice model of the OCCAM group has been adopted and adjusted for RCO. This model is currently the only EVP model available to us for distributed memory parallel computer architecture which we rely on. This model is a multi-layer thermodynamic-dynamic model. It is based on the EVP rheology as developed by Hunke and Dukowicz (1997). Thermodynamics are implemented according to Semtner (1976). Adjustments to Baltic conditions had to be made. Transport and ice-adjustment algorithms have been developed by the OCCAM group (Andrew Coward, Vladimir Ivchenko) and significantly modified at the Rossby Centre for RCO purposes. Henceforth this ice model is called "RCO-ice model" in this report.

The representation of the central quantities h (ice thickness) and c (ice concentration) can be summarized by the equations

$$\frac{\partial h}{\partial t} = \left.\frac{\partial h}{\partial t}\right|_{advect} + \left.\frac{\partial h}{\partial t}\right|_{diffusion} + \left.\frac{\partial h}{\partial t}\right|_{thermo} + \left.\frac{\partial h}{\partial t}\right|_{lateral}, \tag{84}$$

$$\frac{\partial c}{\partial t} = \left.\frac{\partial c}{\partial t}\right|_{advect} + \left.\frac{\partial c}{\partial t}\right|_{diffusion} + \left.\frac{\partial c}{\partial t}\right|_{lateral} \tag{85}$$

describing advective (Section 3.1.5), diffusive (Section 3.1.5), thermodynamic effects in the vertical (Section 3.2) and lateral freezing and melting (Section 3.2.7).

In this section, the RCO-ice model is described. First results are shown for verification later in this report.

3.1 Dynamics

3.1.1 Rheology

Besides other quantities, the model predicts velocity, thickness and concentration. The latter two are advected, whereby convergence (piling up, ridging) or divergence (cracks, rifts) may occur. In order to determine the response of the ice to convergence under high concentration, a rheology (a relation between ice stress and velocity gradient) must be introduced.

The two major governing equations of ice dynamics are the momentum equation and a constitutive law. Momentum is described as

$$m\frac{\partial u_i}{\partial t} = \frac{\partial \sigma_{ij}}{\partial x_j} + \tau_i(u_k) \tag{86}$$

with total mass of ice and snow per unit area m, ice velocity u_i $(i = 1, 2)$ and internal ice stress tensor σ_{ij}. $\tau_i(u_k)$ represents the forcing

$$\tau_i(u_k) = \tau_{ai} + \tau_{wi} + \varepsilon_{ij3} m f u_j - mg\frac{\partial H_0}{\partial x_i} \tag{87}$$

with Levi-Civita tensor ε_{ijk} and sea surface height H_0 $(= \zeta$ in Section 2). The viscous-plastic rheology constitutive law is well established and has been introduced by Hibler (1979):

$$\frac{1}{2\eta}\sigma_{ij} + \frac{\eta - \zeta}{4\eta\zeta}\sigma_{kk}\delta_{ij} + \frac{P}{4\zeta}\delta_{ij} = \dot{\epsilon}_{ij} \tag{88}$$

(η = shear viscosity, ζ = bulk viscosity, P = internal ice pressure, $\dot{\epsilon_{ij}} = \frac{1}{2}(\frac{\partial u_i}{\partial x_j} + \frac{\partial v_j}{\partial y_i}) =$ rate of strain).

Recently, a modification to VP has been introduced by Hunke and Dukowicz (1997). An elastic term has been added:

$$\frac{1}{E}\frac{\partial \sigma_{ij}}{\partial t} + \frac{1}{2\eta}\sigma_{ij} + \frac{\eta - \zeta}{4\eta\zeta}\sigma_{kk}\delta_{ij} + \frac{P}{4\zeta}\delta_{ij} = \dot{\epsilon}_{ij} \tag{89}$$

This converts the constitutive law to a prognostic equation which can be explicitly discretized with favorable numeric features. Convergence studies by Hunke and Dukowicz (1997) reveal the possibility of distinctly higher convergence rates for EVP $(\sim (1 - \alpha\Delta x)^k)$ than for VP $(\sim (1 - \alpha\Delta x^2)^k)$. This handy convergence rate enables practical use of explicit numerics. This is a great advantage on massively parallel processing (mpp) architecture, because message passing as a cpu-performance bottleneck can be limited.

Numerical implementations of VP suffer from a singularity for zero strain rate. Viscosities have to be limited (regularized) by an upper bound. This leads to a big range of effective viscosities. The regularization together with the implicit discretion of VP

causes potential inaccuracies.

EVP includes a computationally efficient elastic wave mechanism. Elastic waves represent a different numerical regularization of the singularity that occurs at zero strain rate: for infinite viscosities, the viscous terms in Eq.(89) approach zero and the elastic term takes over control. The balance is no longer viscous-plastic, but elastic-plastic. In this limit, zero strain rates are avoided. Thus, upper bounds for bulk and shear viscosities ζ and η are not necessary.

Hunke and Dukowicz (1997) demonstrated EVP's ability to reproduce VP's behaviour on long timescales while producing more accurate ice response to forcing of shorter times scales (days or less). While retaining the essential physics, EVP responds more quickly to changing winds as does VP. Considering the comparatively small spatial dimensions of the Baltic Sea, this feature appears to be promising.

The Rossby Centre has chosen to use EVP rheology because its ability to run efficiently on parallel computer architectures, its regularization and because of the potentially better response behaviour.

3.1.2 Ice pressure

The pressure (or strength) of sea ice must be dependent on ice concentration and ice thickness. Several linear and quadratic formulations (for h) have been used in the past. The prevalent traditional formulation for ice pressure is

$$P = P^* che^{-C^*(1-c)} \tag{90}$$

with constants P^* and C^*. This gives a high ice pressure for thick and highly concentrated ice. The bulk and shear viscosities ζ and η depend on the ice pressure P in the numerator:

$$\zeta = \frac{P}{2\delta} \quad , \quad \eta = \frac{P}{2\delta e^2} \tag{91}$$

with

$$\delta = \left[(\dot{\epsilon}_{11} + \dot{\epsilon}_{22})(1 + e^{-2}) + 4e^{-2}\dot{\epsilon}_{12}^2 + 2\dot{\epsilon}_{11}\dot{\epsilon}_{22}(1 - e^{-2})\right]^{1/2} \tag{92}$$

and the yield curve ratio $e = 2$.

Therefore, smoothed ice and velocity fields can be expected for high pressures. Especially in highly compact ice, high values for P^* reduce the motion. For less compact ice, P^* is not a sensitive parameter. The parameter C^* plays a bigger role for less compact situations: ice moves more freely for increasing C^*. $1/C^*$ represents the e-folding scale of ice-stress reduction in decreasing ice-concentration c.

Several sensitivity studies for the ice pressure parameter P^* are available (e.g., Leppäranta et al. (1995), Chapman et al. (1994)). P^* has been determined by comparing model ice velocities with satellite tracked ice drift trajectories. A value for

$P^* = 2.75 \cdot 10^4 Nm^{-2}$ results for typical VP models. However, as this determination of the parameter P^* depends on the model features like grid length, timescale of the forcing and others, there is an unspecified range for using P^* as a calibration parameter. One-way coupling tests with the "CICE"-EVP distribution of Hunke (1997) applied to the RCO model domain confirmed smoother thickness fields, while the overall structure is unchanged. The standard choice for the RCO-ice model is $P^* = 2.75 \cdot 10^4 Nm^{-2}$ and $C^* = 20$.

3.1.3 Young's modulus

Young's modulus E (elasticity modulus) controls the value of strain rate at which the EVP regularization becomes active to prevent zero strain rates and infinite viscosities. E is related to an adjustable parameter E_0:

$$E = \frac{2E_0\rho_i ch}{\Delta t_e^2} min(\Delta x^2, \Delta y^2) \tag{93}$$

where $0 < E_0 < 1$, ρ_i = sea ice density, Δt_e = time step for ice dynamics, $\Delta x, \Delta y$ = grid distance. Stability considerations lead to a possible range of $0 < E_0 < 0.5$ (Hunke and Dukowicz, 1997).

One-way coupling tests with the "CICE"-EVP distribution have been carried out. The maximum area of ice coverage has been used as a test quantity, because it is most relevant for the SWECLIM purpose of regional modelling. Values of E_0 ranging from E_0 = 0.1 - 0.5 have been tested for a timestep of 2250 s. As a result, the maximum ice coverage does not significantly depend on E. This result is in agreement with more general findings of Hunke and Dukowicz (1997). A large range of E_0 exists for which the EVP method is stable. In particular, this is beneficial for the model's timestep. A variation of timestep with constant E_0 is equivalent to an according variation of E_0 with constant timestep. For RCO, $E_0 = 0.25$ is a choice in the mid of the stable range.

3.1.4 Timestep and subcycles

Hunke (1997) gives a conservative estimate of a stable transport timestep Δt for the EVP rheology:

$$\Delta t < \frac{min(\Delta x, \Delta y)}{4\ max(u, v)}\,. \tag{94}$$

For the high resolution version of the model, $\Delta x = 2\,nm$ and $max(u)$ estimated to be $50\,cms^{-1}$, this gives a maximal timestep of $1850\,s$. The coarser resolution of $6\,nm$ requires not more than $5550\,s$. This is well above the ocean model's timesteps of $150\,s$ ($2\,nm$) and $600\,s$ ($6\,nm$). As the ice model is integrated with the ocean timestep ($\Delta t = \Delta t_c$), stability is ensured and inaccurate results are prevented.

Within each timestep, the dynamic component needs to subcycle several times to damp elastic waves. As described in Hunke and Zhang (1999), the elastic term initially makes a prediction for the stress σ, which is then "corrected" toward the VP solution

by means of subcycling. By choosing the number of subcycles N, a compromise has to be made between an energetic solution that quickly adjust during rapidly changing forcing conditions (small N) and a solution which not significantly differs from VP on longer timescales (high N). Hunke and Zhang (1999) recommend N = 100.

During tests with the "CICE"-EVP distribution, N has been varied between 20 and 200. Interestingly, the area of ice coverage again is not sensitive to this parameter. However, timeseries of ice quantities at specific locations can show significant differences. Elastic waves can be seen for low N. These are damped out for high N's. This illustrates the existence of elastic waves. The insensitivity of the ice covered area to N enables us to choose N purely for reasons of numerical stability. N = 80 is the standard value in RCO.

Table 4 lists the standard parameters for the RCO-ice model's rheology.

E_0	Young's modulus	0.25
N	Number of subcycles	80
Δt	Timestep	$150\,(600)\,s$
P^*	Pressure coefficient	$2.75 \cdot 10^4\, Nm^{-2}$
C^*	Empirical constant	20
Δy	Spatial latitudinal resolution	$2\,(6)\,nm$
Δx	Spatial longitudinal resolution	$4\,(12)\,nm \cdot \cos\phi$

Table 4: *Standard parameters for the EVP rheology for high and low resolution (in brackets).*

3.1.5 Transport

The transport model is given by advection and diffusion of the ice volume (ch_i), ice concentration (c), snow volume (ch_s), heat content of brine (W_{bri}), surface temperature (T_{sur}), temperature of snow layer (T_s) and temperature of ice layers (T_i). Thus, snow and ice volume are transported as

$$\left.\frac{\partial(ch)}{\partial t}\right|_{adv,dif} = -\vec{u}\cdot\nabla(ch) + \nabla\cdot\left(A_{ice}\,\nabla(ch)\right). \tag{95}$$

All other quantities are transported as

$$\left.\frac{\partial f}{\partial t}\right|_{adv,dif} = -\vec{u}\cdot\nabla f + \nabla\cdot\left(A_{ice}\,\nabla f\right) \tag{96}$$

with f = c, W_{bri}, T_{sur}, T_s and T_i. An upstream advection scheme has been chosen for now. The harmonic diffusion is necessary to prevent numerical instabilities, however, the diffusion coefficient A_{ice} can be kept as small as $4 \cdot 10^2\, m^2 s^{-1}$. This choice corresponds well with other ice models, e.g., Haapala and Leppäranta (1996).

The basic discrimination of ice types is thick ice (multiple layers) and thin ice ("zero"-layer) as defined in Section 3.2 (discriminating thickness h_0). Both ice types are advected.

An exception from advection is fast ice. This coastal ice is found in shallow areas. It is stationary because it is grounded by several contacts of ridged ice with the bottom. In the Baltic Sea the fast ice zone typically extends to the 10 m isobath. Thus the model limits ice movement by

$$\vec{u} = \begin{cases} \vec{u} & \text{if water depth} > 10 \text{ m} \\ 0 & \text{otherwise.} \end{cases} . \tag{97}$$

3.2 Thermodynamics

3.2.1 Semtner's layer models

The thermodynamics are based on a publication of Semtner (1976). It handles local rates of vertical growth and melt of snow and existing ice. New ice is treated by a separate mechanism described in subsection "Leads".
The sea ice system consists of one or more layers of ice and one layer of snow on top. The layer structure is illustrated in Fig.8.

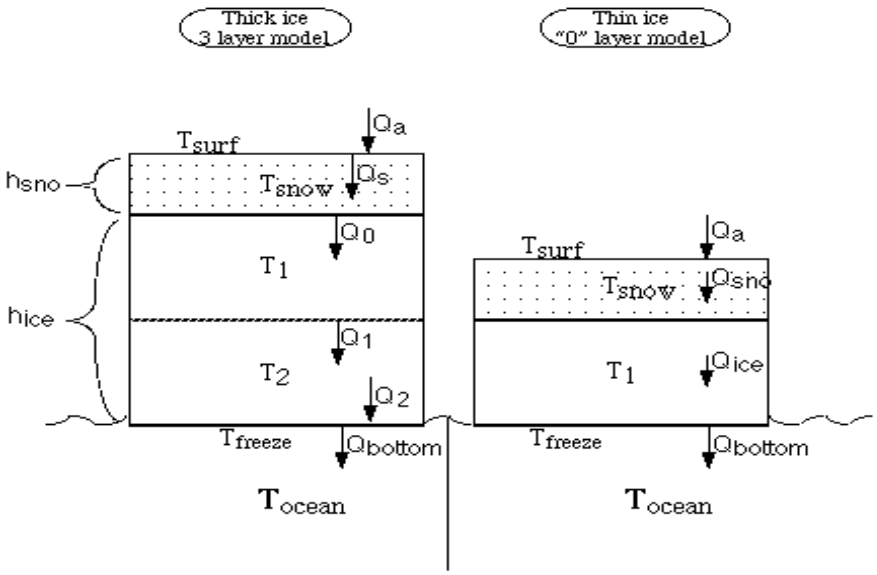

Figure 8: *The multi-layer and "zero"-layer model of Semtner (1976): thick ice (left) and thin ice (right). Q's are heat fluxes, h's layer thickness and T's are temperatures.*

Vertical heat fluxes through internal and external boundaries of the ice-snow system are governed by one-dimensional diffusion equations. The temperature within the ice and snow layers are calculated as

$$(\rho c_p)_{i,s} \frac{\partial T}{\partial t} = k_{i,s} \frac{\partial^2 T}{\partial z^2} \tag{98}$$

with i,s representing ice and snow. $k_{i,s}$ is the diffusivity constant, $c_{p(i,s)}$ the thermal capacity (values see Table 5) and T is the temperature within ice or snow. Heat flux differences are used to calculate thickness changes due to accretion, ablation and melting.

Two basically alternative formulations are used:

- **Thick ice** (multi-layer)
  consists of one or two layers of ice and one layer of snow.
- **Thin ice** ("zero"-layer)
  consists of one layer of ice and one layer of snow with simplified flux formulations.

The reason for this discrimination is numerical stability. The multi-layer ice model tends to become unstable for snow of less than 15 cm thickness and ice of less than 25 cm thickness. Therefore, the discriminating thicknesses between thin and thick ice $h_{0,i}$ and snow $h_{0,s}$ are set accordingly.

For a multi-layer "thick" ice/snow compound as in Fig.8 (left) , growth and decay rates of individual layers are described in terms of diffusive energy fluxes at the upper and lower surfaces of the layers. A linear temperature profile between the centered temperature points is assumed. For a "zero"-layer "thin" ice/snow compound as in Fig.8 (right), simple mass balance equations are applied. Ice and snow temperatures are calculated along a single linear interpolation of the freezing point temperature T_{fp} (below the ice) and surface temperature T_{sur} of ice or snow. A uniform vertical interior heat flux is applied for the whole snow-ice compound. For both cases, thin and thick ice, the bottom temperature right below the ice is always given by the freezing point. The surface temperature is obtained as a solution in instantaneous equilibrium with the forcing (see Section 3.2.3).

3.2.2 Boundary conditions and fluxes

The wind stress to the ice is parameterized similar as to the ocean (cf. Eq.(30))

$$\vec{\tau}_{ai} = c_{ai}^d \, \rho_a \left| \vec{U}_{10} \right| \vec{U}_{10} \tag{99}$$

with the air-ice drag coefficient $c_{ai}^d = c_{aw}^d$ (Eq.(31)).

The boundary condition for heat at the top of ice or snow is

$$k_{i,s} \frac{\partial T}{\partial z} \;=\; Q_a \,. \tag{100}$$

The total heat flux Q_a is given by the sum of shortwave radiation Q_{SW}, longwave incoming radiation $Q_{LW\downarrow}$, longwave outgoing radiation $Q_{LW\uparrow}$, sensible Q_S and latent heat fluxes Q_L.

$$Q_a = Q_{SW}(1 - I_0) + Q_{LW\downarrow} - Q_{LW\uparrow} + Q_S + Q_L \tag{101}$$

with fraction of penetrating solar radiation $I_0 = I_{0,1} + I_{0,2}$ stored in brine pockets $I_{0,1}$ (Section 3.2.5) or in the ocean $I_{0,2}$ (Section 3.4). Q_a corresponds to Q_T, the heat flux at the open water surface (see Section 2.2.2). The individual contributions are given by

shortwave radiation (Q_{SW}):

$$Q_{SW} = Q^0_{SW}(1 - \alpha_{i,s}) \tag{102}$$

with Q^0_{SW} defined in Eq.(46) and ice albedo α_i or snow albedo α_s.

longwave incoming radiation ($Q_{LW}\downarrow$):
This is calculated according to Bodin (1979) as in the open water case (cf. Eq.(40)):

$$Q_{LW\downarrow} = \epsilon_w \, \sigma_s \, T^4_{air} \, (a_1 + a_2 \, e_a^{0.5}) \, (1 + a_3 \, C_a^2) \tag{103}$$

with σ_s Stefan Boltzmann's constant, ϵ_w emissivity of the water surface, e_a saturation water vapor pressure in the atmosphere, C_a cloudiness and a_1, a_2, a_3 empirical constants.

longwave outgoing radiation ($Q_{LW\uparrow}$):
This is calculated from Stefan Boltzmann's law

$$Q_{LW\uparrow} = \sigma_s T^4_{sur} \, . \tag{104}$$

sensible heat flux (Q_S):
Following Large and Pond (1982),

$$Q_S = \rho_a \, c_{pa} \, c^s_{ai} \, \left|\vec{U}_{10}\right| \, (T_a - T_{sur}) \tag{105}$$

with T_a = air temperature, T_{sur} = ice or snow surface temperature, ρ_a = density of air, c_{pa} = specific heat of air, and the bulk heat transfer coefficient

$$c^s_{ai} \times 10^3 = \begin{cases} 1.13 & : \quad (T_a - T_{sur}) < 0 \quad \text{unstable} \\ 0.66 & : \quad (T_a - T_{sur}) \geq 0 \quad \text{stable} \end{cases} \, . \tag{106}$$

latent heat flux (Q_L):

$$Q_L = c^l_{ai} \, \rho_a \, L_{ai} \, \left|\vec{U}_{10}\right| \, (q_a - q_s) \, , \tag{107}$$

$$q_s = \epsilon \frac{e_s}{P_0} \, , \tag{108}$$

$$e_s = r \, e^{\frac{c_1 \, T_{sur}}{T_{sur} + T_0 - c_2}} \tag{109}$$

with $T_0 = 273.155\,K$, L_{ai} = latent heat of sublimation at the air-ice interface, c^l_{ai} = corresponding bulk heat transfer coefficient, q_s = specific humidity of the ice surface, e_s = saturation water vapor pressure of the ice surface, c_1, c_2, ϵ and r empirical constants.

Heat fluxes directly under the bottom of the ice provide an important boundary condition. Semtner (1976) used constant bottom heat fluxes which appeared to be strongly influential on the mean sea ice thickness. Bottom fluxes between 0 and 8.28 Wm^{-2} ($\hat{=} 4.5\,kcal\,cm^{-2}\,yr^{-1}$) lead to 5 m mean thickness difference. This means that the bottom flux can either be used as an efficient tuning parameter or that it needs to be parameterized in a meaningful way. Bottom fluxes can be calculated according to Haapala and Leppäranta (1996) using a bulk formula

$$Q_{bottom} = \rho_w\, c_{pw}\, c^h_{wi}\, |\vec{u}_w - \vec{u}_i|\, (T_w - T_{fp}) \tag{110}$$

where c_{pw} is the specific heat of sea water and c^h_{wi} the bulk heat transfer coefficient. T_w and T_{fp} are the water and freezing point temperature of water. Omstedt and Wettlaufer (1992) suggested to use $c^h_{wi} = 2.8 \cdot 10^{-4}$ in order to get reasonable results. Temperature and velocity differences in Eq.(110) have to be limited to ensure a minimal heat flux: $\Delta u_{min} = 0.001\ ms^{-1}$ and $\Delta T_{min} = 0.1$ K. Eq.(110) allows for variable bottom fluxes responding to changes in temperature under the ice. Heat flows in both upward and downward direction are enabled. The same but opposite flow can be applied to the upper ocean layer. Below freezing point temperatures in the upper ocean are forced back towards the freezing point by receiving heat from the ice. Thereby, the necessity of a direct setting of water temperature is eliminated.

The freezing point temperature T_{fp} is calculated according to Millero (1978)

$$T_{fp} = -0.0575\,S + 1.710523 \cdot 10^{-3}\,S^{3/2} - 2.154996 \cdot 10^{-4}\,S^2\,. \tag{111}$$

3.2.3 Surface temperature

The surface temperature can be approached to by assuming it to be an equilibrium value that results if the internal snow and ice profile adjusts instantaneously to the applied forcing. Further assuming, that the surface temperature change within a timestep is small, a temperature change ΔT can be obtained by linearly approximating the surface fluxes (expanding in a Taylor series) and resolving for ΔT. A new surface temperature at the current time step is then given as the sum of the temperature at the previous timestep and the temperature change $T_{sur,+} = T_{sur,-} + \Delta T$. Semtner (1976) suggests to linearly approximate solely the blackbody emission term. We follow Hunke (1997) in refining and extending this concept to a linearization of sensible and latent heat flux as well. Then ΔT satisfies the equation

$$\begin{aligned}(1-\alpha_{i,s})(1-I_0)Q^0_{SW} + Q_{LW\downarrow} - \sigma_s T^4_{sur,-} + Q_S|_{T_{sur,-}} + Q_L|_{T_{sur,-}} \\ -\Delta T \cdot 4\sigma_s T^3_{sur,-} \\ -\Delta T \cdot \rho_a\, c_{pa}\, c^s_{ai}\, |\vec{U}_{10}|\end{aligned}$$

$$-\Delta T \cdot c_{ai}^{l}\,\rho_a\,L_{ai}\,|\vec{U}_{10}|\,\frac{c_1(T_0-c_2)q_s}{(T_{sur}+T_0-c_2)^2} + k_{i,s}\frac{(T_{i,s}-T_{sur,-}-\Delta T)}{h_{i,s}/2n} = 0\,. \quad (112)$$

n is the number of ice or snow layers. Equation (112) can be resolved to

$$\Delta T \cdot \left(4\sigma_s T_{sur,-}^3 + \rho_a\,c_{pa}\,c_{ai}^{s}\,|\vec{U}_{10}| + c_{ai}^{l}\,\rho_a\,L_{ai}\,|\vec{U}_{10}|\,\frac{c_1(T_0-c_2)q_s}{(T_{sur}+T_0-c_2)^2} + k_{i,s}\frac{\Delta T}{h_{i,s}/2n}\right) = \Sigma Q + k_{i,s}\frac{(T_{i,s}-T_{sur,-})}{h_{i,s}/2n} \quad (113)$$

with

$$\Sigma Q = (1-\alpha_I)(1-I_0)Q_{SW}^0 + Q_{LW\downarrow} - \sigma_s T_{sur,-}^4 + Q_S|_{T_{sur,-}} + Q_L|_{T_{sur,-}}\,. \quad (114)$$

A direct application of Eq.(113) is possible in general but may lead to less accurate results and troublesome behaviour. More accurate results are obtained by applying Eq.(113) in a Newton-Raphson iteration several times. A maximum number of 20 iterations together with a convergence criterion of $\Delta T < 0.5K$ yields stable results.

However, this method relies on the above mentioned equilibrium assumption. Practical tests show a preference towards colder than realistic surface temperatures. This point needs to be explored further. It may be speculated, that the equilibrium assumption may not be an appropriate assumption, at least for the conditions in the Baltic Sea.

Should positive temperatures occur in this procedure, the melting algorithm melts ice or snow at the top and resets the surface temperature to the freezing point.

3.2.4 Thickness changes

As now the temperature profile in snow of ice are known as well as the vertical fluxes, thickness changes due to accretion/ablation at the base of the ice and as melting at the top can be calculated.

Melting of snow or ice occurs if the surface temperature increases above the melting point. Then the ice or snow layer's thickness is reduced according to

$$\frac{\partial h_{i,s}}{\partial t} = (Q_a - Q_{sur})/q_{i,s}^h \le 0. \quad (115)$$

Q_a is the atmospheric heat flux. The surface heat fluxes Q_{sur} are differently defined for thick and thin ice/snow:

$$Q_{sur} = \begin{cases} \frac{k_i}{h_i+\frac{k_i}{k_s}h_s}\,(T_{fp}-T_{sur}) & \text{for thin ice,} \\ \frac{k_i}{\frac{h_i}{2n}}\,(T_i-T_{sur}) & \text{for exposed thick ice,} \\ \frac{k_i}{\frac{h_i}{2n}+\frac{k_i}{k_s}h_s}\,(T_i-T_{sur}) & \text{for thick ice and thin snow,} \\ \frac{k_i}{\frac{h_i}{2n}+\frac{k_i}{k_s}\frac{h_s}{2}}\,(T_s-T_{sur}) & \text{for thick ice and thick snow.} \end{cases} \quad (116)$$

$q^h_{i,s}$ is the volumetric heat of fusion for ice or snow at the surface. For details, the reader is referred to Semtner (1979). Ablation or accretion at the bottom is given by

$$\frac{\partial h_{bottom}}{\partial t} = \begin{cases} (Q_{sur} - Q_{bottom})/q^h_b & \text{for thin ice ,} \\ \\ (Q_n - Q_{bottom})/q^h_b & \text{for thick ice .} \end{cases} \tag{117}$$

with the volumetric heat of fusion at the lower surface q^h_b. Q_a, Q_{sur}, Q_{bottom} and Q_n are heat fluxes into the atmosphere, at the surface, bottom and at the upper interface of the lowermost ice layer (see Fig.8).

3.2.5 Brine pockets and penetrating solar radiation

Sea ice releases brine to the sea, however some brine remains in pockets. These brine pockets are able to store heat. Following Semtner (1976), penetrating radiation is partioned between warming of ice layers and heat storage in brine pockets. 17 % ($I_{0,1} = 0.17$) is stored. The temporal change of brine pocket heat content is given by

$$\frac{\partial W_{bri}}{\partial t} = I_{0,1}\,(1 - \alpha_{i,s})\,Q^0_{SW}\,. \tag{118}$$

This heat is saved to delay the upper ice layer cooling. If the upper ice layer temperature drops below the melting point, the energy from the brine pockets is converted to force temperature back towards the melting point, thereby parameterizing release of heat through refreezing of brine pockets.

In polar oceans this parameterization would lead to delayed top ice melting in summer and delayed internal cooling in fall. In the Baltic Sea however, where no ice exists in summer, the brine pocket storage is applied to smooth warming-cooling events.

3.2.6 Snow

Snow on top of sea ice affects the interaction in the ocean-ice-atmosphere system by modifying radiative and thermal properties of the surface. Due to lower thermal conductivity and albedo higher than for ice (see Tables 5 and 6), snow is thought to increase the sensitivity of sea ice to climate change.

It is expected that snow cover decreases the total volume of sea ice grown thermodynamically. It acts as an isolating device to shield the underlying ice from extreme events.

Snowfall in the RCO model is realized by using observed precipitation from the SMHI data base (Lars Meuller, pers.comm.) as forcing. Precipitation over ice is assumed to be converted to snow. Assuming a snow density ρ_s of $0.33 \cdot 10^3\,kg\,m^3$ and a fluid rain density ρ_w of $1.03 \cdot 10^3\,kg\ m^3$ leads to a change of equivalent snow thickness h_s of

$$\frac{\partial h_s}{\partial t} = P\,\frac{\rho_w}{\rho_s} \tag{119}$$

Abbr.	Parameter	model units	SI units
k_i	thermal conductivity of ice	$4.86 \cdot 10^{-3}\, cal\, cm^{-1}\, s^{-1}\, K^{-1}$	$2.0\, W\, m^{-1}\, K^{-1}$
k_s	thermal conductivity of snow	$7.40 \cdot 10^{-4}\, cal\, cm^{-1}\, s^{-1}\, K^{-1}$	$0.3\, W\, m^{-1}\, K^{-1}$
$h_{0,i}$	discriminating thickness between thin and thick ice	$25\, cm$	$0.25\, m$
$h_{0,s}$	discriminating thickness between thin and thick snow	$15\, cm$	$0.15\, m$
h_{min}	min. permitted thickness of ice	$4 \cdot 10^{-2}\, cm$	$4 \cdot 10^{-4}\, m$
c_{min}	min. permitted concentration of ice	$2 \cdot 10^{-2}$	$2 \cdot 10^{-2}$
c_{max}	max. permitted concentration of ice	0.99	0.99
ρ_a	density of air	$1.225 \cdot 10^{-3}\, g\, cm^{-3}$	$1.225\, kg\, m^{-3}$
ρ_i	density of ice	$0.91\, g\, cm^{-3}$	$0.91 \cdot 10^{3}\, kg\, m^{-3}$
ρ_s	density of snow	$0.33\, g\, cm^{-3}$	$0.33 \cdot 10^{3}\, kg\, m^{-3}$
ρ_w	density of water	$1.03\, g\, cm^{-3}$	$1.03 \cdot 10^{3}\, kg\, m^{-3}$
$\rho_a c_{pa}/c_{pa}$	specific heat of air	$0.29 \cdot 10^{-3}\, cal\, cm^{-3}\, K^{-1}$	$1.008 \cdot 10^{3}\, J\, kg^{-1}\, K^{-1}$
$\rho_i c_{pi}/c_{pi}$	specific heat of ice	$0.45\, cal\, cm^{-3}\, K^{-1}$	$2.1 \cdot 10^{3}\, J\, kg^{-1}\, K^{-1}$
$\rho_s c_{ps}/c_{ps}$	specific heat of snow	$0.165\, cal\, cm^{-3}\, K^{-1}$	$2.1 \cdot 10^{3}\, J\, kg^{-1}\, K^{-1}$
$\rho_w c_{pw}/c_{pw}$	specific heat of sea water	$1.0\, cal\, cm^{-3}\, K^{-1}$	$4.186 \cdot 10^{3}\, J\, kg^{-1}\, K^{-1}$
$I_{0,1}$	fraction of penetrating radiation	0.17	0.17
ϵ_w	emissivity of the water surface	0.97	0.97
σ_s	Stefan Boltzmann constant	$1.35 \cdot 10^{-12}\, cal\, s^{-1}\, cm^{-2}\, K^{-4}$	$5.67 \cdot 10^{-8}\, W\, m^{-2}\, K^{-4}$
P_0	sea level pressure	$1.013 \cdot 10^{6}\, dyn\, cm^{-2}$	$1.013 \cdot 10^{5}\, N\, m^{-2}$
a_1	empirical const.		0.68
a_2	empirical const.		0.0036
a_3	empirical const.		0.18
ϵ	empirical const.	0.62197	0.62197
L_{ai}	latent heat of sublimation	$677\, cal\, g^{-1}$	$2.834 \cdot 10^{6}\, J\, kg^{-1}$
c_{ai}^{s}	bulk coefficient for sensible heat		
c_{ai}^{l}	bulk coefficient for latent heat	$1.15 \cdot 10^{-3}$	$1.15 \cdot 10^{-3}$
c_1	empirical const.	21.875	21.875
c_2	empirical const.	7.66	7.66
r	empirical const.	6107.8	6107.8
c_{wi}^{h}	bulk heat transfer coefficient	$2.8 \cdot 10^{-4}$	$2.8 \cdot 10^{-4}$
T_w	temperature of water		
T_{fp}	temperature at the freezing point of water		
q_s^h	volumetric heat of fusion of snow	$26.2\, cal\, cm^{-3}$	$1.1 \cdot 10^{2}\, J\, m^{-3}$
q_b^h	volumetric heat of fusion of water at the ice bottom	$64\, cal\, cm^{-3}$	$2.7 \cdot 10^{2}\, J\, m^{-3}$
q_i^h	volumetric heat of fusion of ice at the surface	$72\, cal\, cm^{-3}$	$3.3 \cdot 10^{2}\, J\, m^{-3}$
L_{wi}	latent heat of fusion	$79\, cal\, g^{-1}$	$3.3 \cdot 10^{5}\, J\, kg^{-1}$
$h_{ref,max}$	max. virtual reference height for lateral freezing	$2.5\, cm$	$0.025\, m$
f_{sol}	penetration factor	0.1	0.1
κ_i	bulk extinction coefficient for ice	$0.015\, cm^{-1}$	$1.5\, m^{-1}$
κ_s	bulk extinction coefficient for snow	$0.15\, cm^{-1}$	$15\, m^{-1}$

Table 5: *Standard parameters for sea ice thermodynamics.*

with P = precipitation.

Melting of the snow top occurs if the surface temperature is less than the melting point of snow. In this case, the surface temperature is set back to the melting point and vertical heat fluxes are calculated accordingly. Melting is then given by Eq.(115).

Snow thickness undergoes advection, diffusion and overrun adjustments as described in Section 3.3 for ice. However, snow cannot grow laterally as ice does. Partial snow cover does not occur. In this development state of the model, concentrations of snow and ice are identical, i.e. if there is snow on the ice, all ice within a grid cell is snow-covered.

3.2.7 Leads

Leads are ice-free areas between the ice. They play an essential role in ocean-atmosphere-ice interaction as vertical fluxes of heat and energy are distinctly different than during ice coverage. Leads occur during the ice formation when the ocean-atmosphere fluxes are not strong enough to fill a complete area immediately. During the freezing phase leads are filled by lateral ice growth. Lateral melting occurs in warming phases. Another source of leads are diverging winds. The advection equation (96) translates this in weaker ice concentration.

Lateral freezing or melting occurs dependent on the direction of the net ocean-atmosphere heat flux. The height (volume per unit area) of new ice to be formed or to be ablated in leads is given by

$$V_{new} = -Q_{TOT}|_{noice} \frac{(1-c)}{q_i^h} \Delta t \tag{120}$$

with the volumetric heat of fusion q_i^h and the model timestep Δt. V_{new} has the dimension of a length. Q_{TOT} is the atmosphere to ocean heat flux as defined by Eq.(32). For lateral freezing, Q_{TOT} is completely consumed for ice formation. No energy from Q_{TOT} is left for further cooling of water.

Lateral freezing in leads occurs if the net ocean-atmosphere heat flux Q_{TOT} is directed upward. In the RCO-ice model, a formulation of Harvey (1988) is used. It is based on an analytic integration of ice growth equations. The ice concentration c and mean ice thickness ($\tilde{h}_i = c\, h_i$) over the ice-free and ice-covered parts of the grid box are governed by

$$\frac{\partial c}{\partial t} = \frac{V_{new}}{\Delta t\, h_{ref}}(1-c) \tag{121}$$

$$\frac{\partial \tilde{h}_i}{\partial t} = c \left.\frac{\partial h_i}{\partial t}\right|_{before} + (1-c)\frac{V_{new}}{\Delta t} \tag{122}$$

with h_{ref} = a virtual thickness of newly formed ice in the lead. $c\frac{\partial h_i}{\partial t}|_{before}$ represents the growth of preexisting ice during a given timestep due to other processes like vertical thermodynamics or advection. h_{ref} can also be interpreted in conjunction with V_{new} as a timescale $\tau_{freeze} = \Delta t\, h_{ref}/V_{new}$. This is the time it would take to fill the lead with ice of thickness h_{ref} under the forcing V_{new}. If the model timestep is shorter than τ_{freeze}, the lead will not be completely filled. This is the rationale of this method. It makes partial lateral freezing in leads possible. This is an important feature of a sea ice system as it enables ongoing ocean-atmosphere interaction through the leads as it occurs in nature.

Harvey (1988) has taken this method one step further after acknowledging that Eq.(121) and (122) do not take into account the reduction of lead area during one timestep. Therefore, Eq.(121) and (122) were integrated analytically over a time Δt

which corresponds to the model timestep:

$$c_{n+1} = 1 - (1 - c_n)e^{-\Delta t/\tau_{freeze}} \tag{123}$$

$$\tilde{h}_{i,n+1} = \tilde{h}_{i,n} + c\,\frac{\partial h_i}{\partial t}\bigg|_{before}\Delta t + (1 - c_n)(1 - e^{-\Delta t/\tau_{freeze}})\,h_{ref}\,. \tag{124}$$

The last term can be described as

$$\Delta c\,h_{ref} = (1 - c_n)(1 - e^{-\Delta t/\tau_{freeze}})\,h_{ref}.$$

Thus, this term of Eq.(124) $\Delta c\,h_{ref}$ can be interpreted as the mean thickness (or virtual volume) of laterally created new ice. It is added to the growth of preexisting ice and to the mean thickness at the previous timestep. The result is then divided by the actual concentration c to obtain the new ice thickness. The new analytically integrated formulation (Eq.(123) and (124)) takes a continuously decreasing ice-free area during a given timestep into account, while the forcing, i.e., the volume per unit area of new ice V_{new}, is assumed to be constant. The effect is illustrated in Fig.9. The change of ice concentration is distinctly smaller if the decreasing ice-free area is taken into account (solid curves in Fig.9).

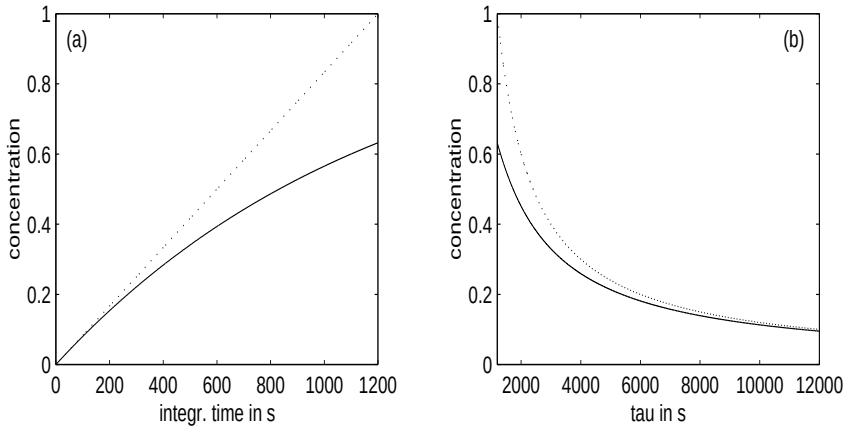

Figure 9: *Effect of taking continuously decreasing ice-free area into account. Change of concentration from zero during a single timestep of 1200 s: for $\tau_{freeze} = 1200\,s$ (a), for various τ_{freeze} (b). For Eq.(121) (dotted curve) and for Eq.(123) (solid curve).*

Hibler (1979), using a formulation like Eq.(121), suggested $h_{ref} = 0.5 - 1.0\,m$ for the polar oceans. These values cannot be applied in the Baltic, as the ice is thinner and vanishes completely during summer. Situations occur with no preexisting ice. Therefore, the choice of the reference height h_{ref} has to allow for initial ice formation and once ice exists, it must be used as a tuning parameter for the ice concentration. These two objectives require a non-constant h_{ref}. For RCO, h_{ref} has been chosen to grow linearly with ice thickness up to $h_{ref,max} = 2.5$ cm:

$$h_{ref} = \begin{cases} h_{min} & \text{if } h_i < h_{min} \\ h_i & \text{if } h_{min} < h_i < h_{ref,max} \\ h_{ref,max} & \text{otherwise} \end{cases}\,. \tag{125}$$

This choice leads to realistic ice concentrations (see also Section 5).

RCO employs a minimum permitted ice thickness h_{min}. If V_{new} cannot supply this minimum no ice is formed. Cut-off thicknesses like this one are common in many ice models, e.g., Haapala and Leppäranta (1996) or Hunke (1997). They crudely represent the initial freezing phase when frazil crystals and grease ice forms but direct atmosphere ocean fluxes are still active. Mechanical mixing can prevent this initial ice from forming areas of closed ice cover (Carsey, 1992). Sophisticated parameterizations for these fine-scale processes are not yet applicable. Therefore strong cooling is required in sea-ice models to form a partial ice cover in a grid box. Similarly, a minimum permitted ice concentration is used.

Lateral melting in leads occurs if the net ocean-atmosphere heat flux is directed downward, i.e., $V_{new} < 0$. RCO uses a simple parameterization which translates the ratio of melted ice volume per unit area V_{new} and ice thickness h_i into a concentration change.

$$\Delta c = c\, V_{new}/h_i\,. \tag{126}$$

The concentration c is multiplied in order to express a decreasing melting effect with increasing ice-free area. Although a simple parameterization, it efficiently distributes the incoming energy among lateral melting of ice and warming of water, because the corresponding factor $(1 - c)$ is applied to the atmosphere-ocean heat flux (see below Eq.(128)).

3.2.8 Albedo

The surface albedo of the snow-ice system depends on whether snow is present or not, and on the state of snow or ice. Dry ice has a higher reflectivity than melting ice. The same is true for snow. Melting conditions are given if the surface temperature is above the melting points of snow or ice. Table 6 lists the different albedos.

Type	Symbol	Albedo (RCO)	Albedo (Perovich, 1996)
dry snow	$\alpha_{s,d}$	0.75	0.87
wet snow	$\alpha_{s,m}$	0.3	0.77
dry ice	$\alpha_{i,d}$	0.66	0.7
wet ice	$\alpha_{i,m}$	0.66	0.3

Table 6: *Albedo of snow and ice used in RCO and according to Perovich (1996).*

The albedos in RCO are not optimized yet. Hence, further sensitivity studies are necessary.

3.3 Adjustments

Ice concentration c is unphysical below 0 and above 1. However such unphysical situations may occur after applying certain algorithms of the model. As mentioned in

Section 3.1.5, c is advected. Convergent situations may lead to $c > 1$. Physical consistency requires some adjustments.

Upper and lower limits for c have been set ($c_{min} = 0.02$, $c_{max} = 0.99$). If c drops below the minimum permitted ice concentration c_{min}, c is set to zero. In the case of $c > c_{max}$, snow and ice thicknesses are adjusted to reflect an upper limit concentration.

$$\left\{ \begin{array}{rl} h_i & = c\, h_i / c_{max} \\ h_s & = c\, h_s / c_{max} \\ c & = c_{max} \end{array} \right\} \quad \text{if} \quad c > c_{max}\,. \tag{127}$$

This formulation conserves volume. On the one hand side concentration is reduced and on the other hand side thickness is increased. This becomes more comprehensible if one thinks about an advecting low concentration ice field of constant thickness. Initially, convergent advection does not increase the mean thickness, but the concentration and volume. After the maximum concentration is reached, volume increase leads to thickness increase. In the model, this is reflected by concentrations greater than one. Eq.(127) translates this to a thickness increase.

The upper limit concentration $c_{max} = 0.99$ is chosen to be less than 1, because small leads can always be found in observations. Cracks and the non-continuous nature of real ice prevents total coverage. A similar measure has been successfully applied on other sea ice models of the Baltic (Omstedt and Nyberg, 1996) as well as the arctic oceans (e.g., Bettge et al., 1996).

3.4 Ice-ocean interaction

The heat content of an ocean grid box under the ice may be changed by pure oceanic processes (advection and mixing), by ocean-atmosphere heat fluxes through leads or by heat exchange with the ice. The flux at the bottom of the ice is given by Eq.(110). The same but opposite flow is applied to the upper ocean layer (Eq.(128)).

In case of lateral freezing, all the atmospheric cooling expressed by the volume per unit area of new ice V_{new} is used to close leads (see Section 3.2.7). In case of lateral melting however, the heat flux from the atmosphere is divided among lateral melting of ice and warming of water. For lateral melting, this is expressed in Eq.(126) by applying a factor c. A corresponding factor $(1 - c)$ is applied to the atmosphere-ocean heat flux

$$Q_{TOT} = \left(Q_{TOT}|_{noice}(1-c)\right)(1-c) + Q_{bottom}\, c\,. \tag{128}$$

Thereby, $Q_{TOT}|_{noice}$ is the atmosphere-ocean heat flux, specified by Eq.(32) and Q_{bottom} is the ice to water heat flux defined by Eq.(110).

Solar radiation is the only flux component at the ice-atmosphere interface, that can pervade sea ice and warm the underlying water. In the Baltic Sea with low salinities, and temperatures close to the freezing point, this can lead to static instabilities with

subsequent mixing events. This pervading part of solar radiation $Q_{SW}^{ib} = Q_{SW}^{0}\,(1 - \alpha_{i,s})\,I_{0,2}$ is described according to Sahlberg (1988):

$$Q_{SW}^{ib} = \begin{cases} Q_{SW}^{0}\,(1-\alpha_s)\,f_{sol}\,e^{-\kappa_s\,h_s - \kappa_i\,h_i} & \text{if } h_s > 10\ cm\,, \\ Q_{SW}^{0}\,(1-\alpha_s)\,f_{sol}\,e^{-\kappa_i\,h_i} & \text{if } 0 < h_s \leq 10\ cm\,, \\ Q_{SW}^{0}\,(1-\alpha_i)\,f_{sol}\,e^{-\kappa_i h_i} & \text{if } h_s = 0\,. \end{cases} \tag{129}$$

κ_i and κ_s are bulk extinction coefficients and f_{sol} a penetration factor.

The atmosphere-ocean freshwater flux in leads, as formulated in Section 2.2.3, Eq.(42), is reduced proportional to the relative area of open water. Further, brine is released into the ocean during the freezing process. This modification is summarized in

$$S_F = S_F|_{noice}\,(1-c) + \frac{V_{new}}{\Delta t}\,\frac{\rho_i}{\rho_w}\,S \tag{130}$$

with S salinity of the uppermost ocean box and Δt timestep.

Similar modification apply to ocean-atmosphere momentum fluxes. The wind stress is limited to the lead area, whereas an ice stress on the ocean is applied under the ice.

$$\vec{\tau} = (1-c)\,\vec{\tau}|_{noice} + c\,\rho_w\,c_{wi}^{d}\,|\vec{u}_i - \vec{u}_w|\,(\vec{u}_i - \vec{u}_w) \tag{131}$$

with the ice-ocean drag coefficient $c_{wi}^{d} = 3.5 \cdot 10^{-3}$.

3.5 Sequence of algorithms

The code of the sea ice model is embedded in the RCO ocean model. The ice code uses the existing ocean structure and message passing system. At each timestep a sequence of ice calculations is performed as outlined below:

- calculate ice-atmosphere fluxes
- check sst,
  if sst $< T_{fp}$ or $h_i > 0$
  allow ice formation
- calculate ice volume to be formed in leads
- limit ocean-atmosphere heat and freshwater fluxes according to the relative size of leads within each grid box
- check ice and snow thickness if multi-layer or "zero"-layer model is applied
- determine surface temperature
- melt snow or ice under melting conditions

- store heat in brine reservoir
- calculate ice or snow temperature profile
- calculate accretion or ablation at the bottom of the ice
- modify exchange heat between ice and ocean
- add snow on top if precipitation
- modify momentum forcing under ice to account for stress of ice on water
- advection using EVP ice velocities
- diffusion
- timestepping
- adjust possible ice concentration overrun
- use brine reservoir
- lateral freezing and melting
- adjust possible ice concentration overrun
- set number of levels for ice model
- calculate EVP ice velocities

4 Model code

4.1 Overview

The starting point for the Rossby Centre Ocean model was a sub-set of the fully global OCCAM model (Webb et al., 1997). The OCCAM model is an array processor version of the GFDL Modular Ocean Model version 1.0 (Pacanowski, 1996). OCCAM has been developed and run at the James Rennell Division, Southampton Oceanography Centre. The actual OCCAM code consists of a number of FORTRAN 77 modules and associated header files. Extensive use is made of pre-processor directives to allow the easy switching of physics or numerical techniques. To produce a more user-friendly and accessible code for the SWECLIM project, many of the pre-processor options available in OCCAM have been permanently selected and a new set of partially pre-processed source modules have been created (Coward, 1997). During the past two years a number of new options have been added to the code by the authors, especially in the areas of open boundary conditions, atmosphere forcing, radiation model, river runoff, turbulence modelling, implicit vertical friction, thermodynamics and dynamics of sea ice, etc.. The code development is a cooperation between Rossby Centre, Southampton Oceanography Centre and MISU at Stockholm University.

OCCAM uses a Master-Slave arrangement with one master processor (called 'Caesar') dedicated to external I/O and house-keeping tasks. At the beginning of each run, this processor reads in values for restarting the model, the processor map, the topography map and forcing/boundary data. Each slave processor (called 'Legion') receives the data that it needs to perform the calculations in the domain that has been assigned. Later in the run the master also controls and handles the writing out of model results, the reading in of new forcing fields and the calculation of diagnostics.

OCCAM has an asynchronous I/O management. When a slave processor reaches an archive time step it buffers the solution it holds before continuing with the main calculations. Waiting is only necessary for exchange of boundary data (from the so-called 'halo') from neighbouring processors to solve the discretized equations. Each processor has a domain consisting of a core region surrounded by a ring of 'halo' points.

The RCO model is being running on the CRAY-T3E at the Swedish National Supercomputer Centre (NSC) in Linköping with the SHMEM message passing library. In addition, the model has been used for testing on SUN, DEC ALPHA and HEWLETT PACKARD workstation clusters with the MPI message passing library.

As mentioned in the introduction (Section 1) two years ago none of the available Baltic Sea models was suitable to integrate multi-year runs with sufficient resolution due to technical reasons. This gave the motivation to develop a new Baltic Sea model within SWECLIM. Before the decision for the OCCAM code a model intercomparison between the parallel codes OCCAM and MOM 2 has been carried out mainly to compare cpu-performance. The MOM 2.2 code with special features and options of the oceanography model group at the Baltic Sea Research Institute in Warnemünde (IOW) has

kindly been made available to the Rossby Centre (Schmidt et al., 1997). The parallelization of MOM 2 has been done in Warnemünde. Using the Warnemünde model SWECLIM might have had the advantage to reduce the model development time because a lot of special Baltic Sea features are included which were not available for the global OCCAM. The results of the benchmark tests (one month integration period) shows Fig.10. The speedup is normalized for both models to a 13 processor run and

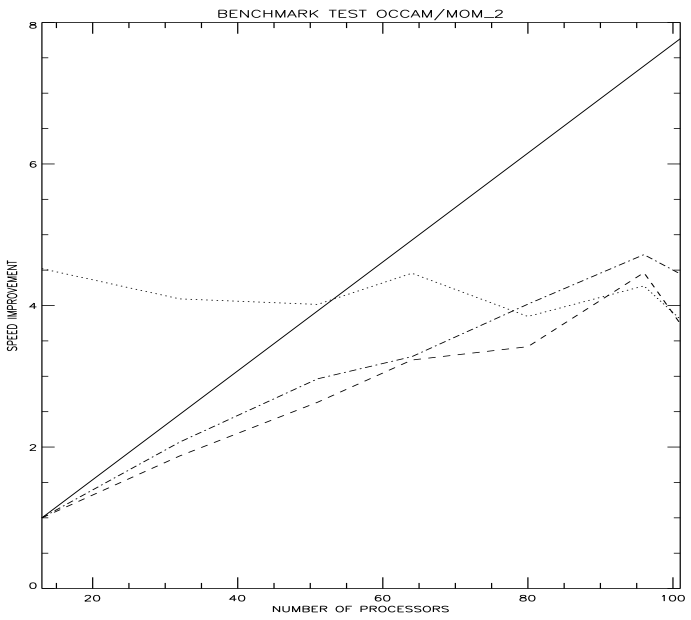

Figure 10: *Benchmark test between OCCAM (dashed) and MOM 2 (dash-dotted). The speed ratio (OCCAM divided by MOM2) is shown as dotted curve and the ideal speedup as solid curve.*

has comparable size. The speed factor of 4 between the models is approximately constant for different number of processors. That means OCCAM was 4 times faster than the Warnemünde model. It should be noted that the model intercomparison has been carried out in January/February 1998. Since then both models have been improved further and the Warnemünde group has switched to a new parallel version, MOM 3. The reason for the large difference is that the Warnemünde model was parallelized in full latitudinal strips. Thus, sea points were calculated as well as land points.

4.2 Processor maps

Each processor is assigned a compact region of the ocean surface (see Figures 11 - 13).

Different from the standard MOM 2 code no calculations are carried out on land regions and only sea points are considered. For Baltic Sea and North Sea modelling this treatment is important for the performance because only 10 percent of the three-dimensional array holding the prognostic variables are sea points. For an efficient code, the total amount of work to be done needs to be assigned as evenly as possible between

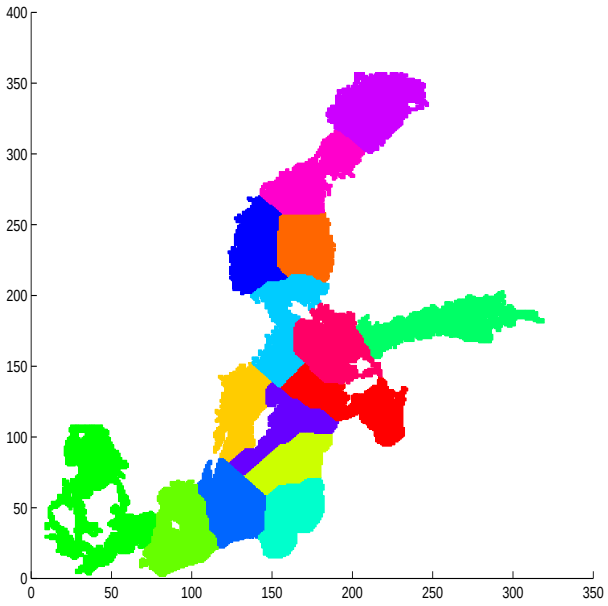

Figure 11: *Processor map for 16 processors (15 slaves and 1 master).*

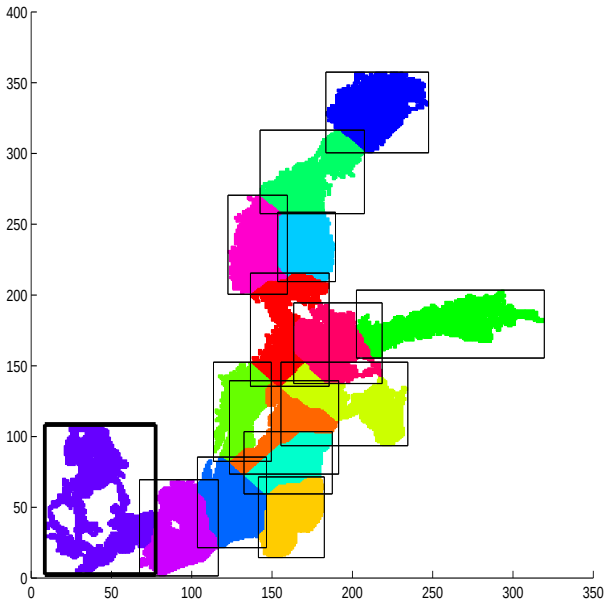

Figure 12: *As Fig.11 but with bounding boxes. The largest box is emphasized using a thick frame.*

the processors. To allow this, the OCCAM code is written for irregular shaped processor regions. For high resolution models, memory requirements restrict the maximum dimensions of the processor regions, which sets the lower boundary on the number of processors that can run the model. The total memory requirement is given by the

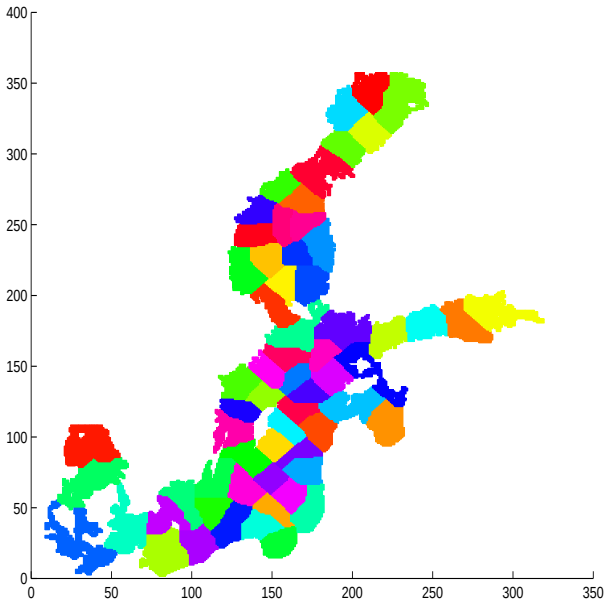

Figure 13: *Processor map for 64 processors (63 slaves and 1 master).*

largest box surrounding the irregular shaped processor domains (Fig.12). Although not necessary OCCAM uses the memory of a virtual box with dimensions given by the maximum length of all bounding boxes in longitudinal direction times the maximum length in latitudinal direction.

The derivation of an optimal partitioning for any particular number of processors is a non-trivial task requiring some degree of interactive manipulation of the processor maps using a OCCAM utility program (Coward, 1997). This utility program requests an approximate number of processor regions along each horizontal dimension and divides the region into equal rectangular areas. Any areas devoid of sea points (and hence containing no work) are removed from the map. Thus the final number of processor regions defined may well be less than the number requested. This is increasingly true for ever greater numbers of processors.

RCO uses a different load balancing strategy than the original OCCAM code described by Coward (1997). At the Rossby Centre a standalone software package for minimizing load unbalance has been developed. The program assigns regions of the ocean surface to each processor, while minimizing the difference between the work for the processors using a new partitioning strategy based on graph theory (Rantakokko, 1997). Input to the software package are the grid point depths and the number of slaves. To assess the work for each vertical column belonging to the surface point (i, j) the following workmap w is used

$$w(i, j) = \alpha + \beta\, k(i, j) \tag{132}$$

with k the number of vertical levels for the corresponding surface point.

The workmap w is a two dimensional data structure that quantifies the amount of work that needs to be done for the vertical column belonging to the surface point (i, j). The idea with having the two weights α and β is that one can now adjust for the fact that the work in each column is not just a function of depth, it is a function of the ratio of work in the baroclinic part (which is a function of depth) and the barotropic part (only calculated for the surface points). If one gets the weights right it should be possible to minimize the difference in the amount of work done by each processor, instead of just minimizing the difference in the number of grid points that each processor is assigned. For a given workmap the software package calculates first the corresponding so-called graph (a mathematical function) and second processor maps based on recursive spectral bisection method for a given number of processors (Rantakokko, 1997). In case of an optimal workmap the load will be even and the number of communication points will be a minimum for the processor domains.

Rantakokko (1998, pers.comm.) implemented the new developed software package into RCO and made a series of benchmark tests to find out the optimal set of constant weights α and β (Fig.14). Due to the complicated code structure it is not obvious

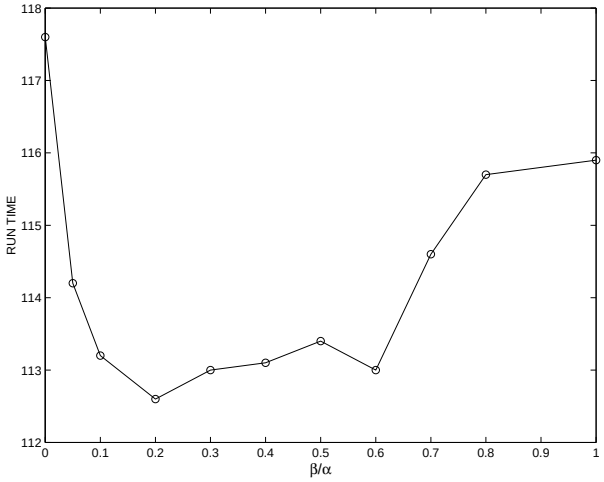

Figure 14: *Code performance as a function of the weight ratio calculated by Rantakokko (1998, pers.comm.).*

that only one absolute minimum exists for a set of only two constants. According to Rantakokko's results (Fig.14) in RCO $\alpha = 5$ and $\beta = 1$ are used.

Using an improved processor map for a 16 processor run (15 slaves and 1 master) RCO in coarse resolution version ($6\,nm$) is 40 % faster compared to a run with a processor map assigning the same number of surface grid points to each slave ($\alpha = 1$, $\beta = 0$). The latter would be the perfect solution of the interactive procedure of the OCCAM utility program to generate a processor map.

Using an improved processor map for 32 processors RCO version 1.0 with $6\,nm$ grid

distance and without sea ice model consumes on the CRAY-T3E 1 cpu hour per model year approximately. Hence, this version is as fast as the PROBE-Baltic model on a SUN workstation (Anders Omstedt, pers.comm.).

4.3 Code optimization

Faxen (1999) made a single and a parallel performance analysis of RCO using different workmaps (Fig.15 and 16). Additionally, he implemented optimizations into RCO

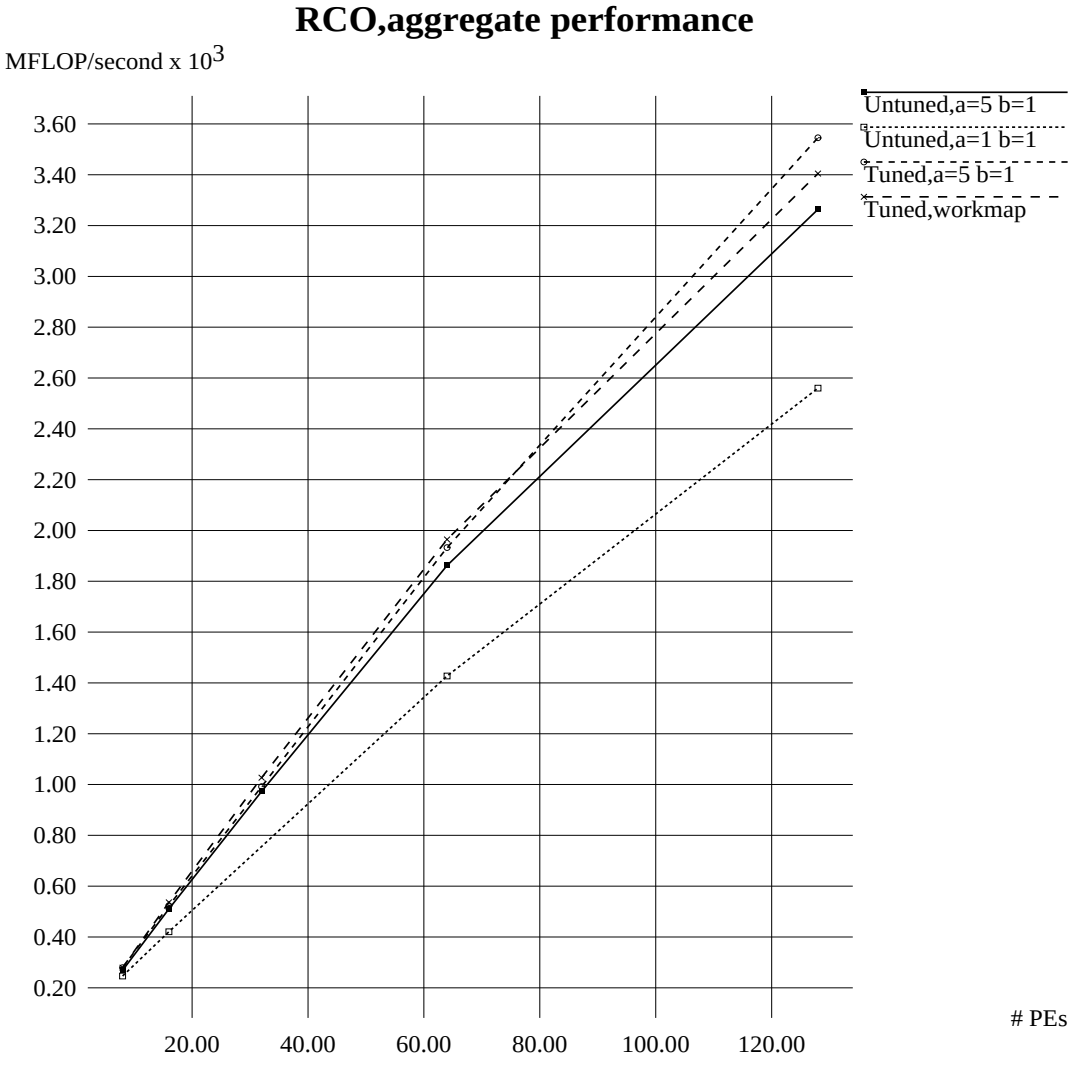

Figure 15: *Aggregate performance of RCO without sea ice (adopted from Faxen, 1999). The abbreviations for the workmaps are explained by Faxen (1999).*

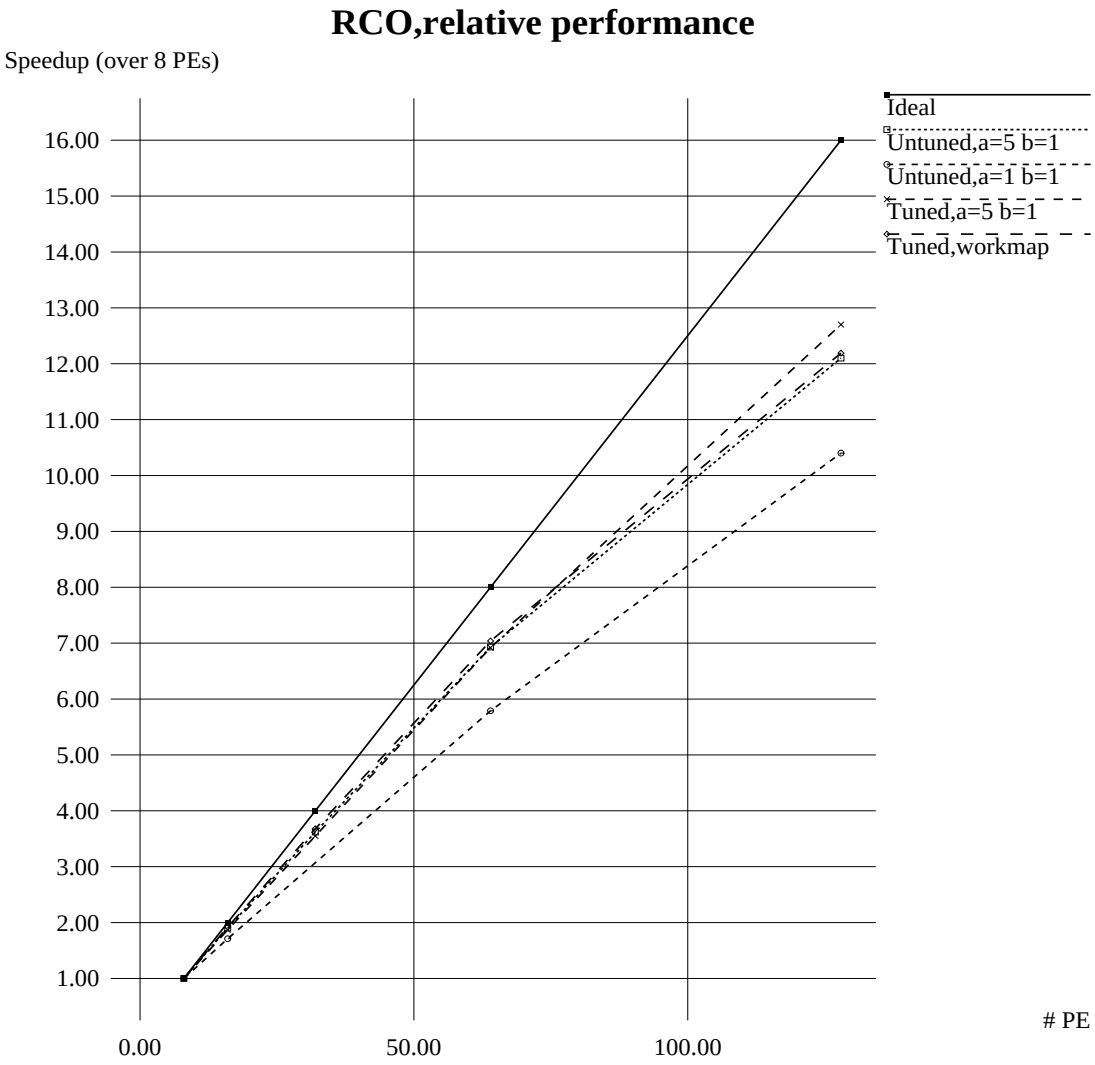

Figure 16: *Relative performance of RCO without sea ice (adopted from Faxen, 1999).*

developed by Richmond (1996).

Faxen concluded from the analysis:

- The code is running at decent single processor speed.
- There are no really obvious hot spots that can quickly improve the speed of the code significantly.
- The code shows very good scalability despite the fact that there is a non-negligible load unbalance present.

- The processor maps are important. Currently $\alpha = 5$ and $\beta = 1$ or using a version based on actual computations from earlier runs gives the best performance.
- The introduction of ice makes it necessary to modify the load balancing strategy further.

More details are given by Faxen (1999).

5 First results

5.1 Overview

Two hindcast periods have been selected to evaluate the Rossby Centre Ocean model. In this report we consider only the time period May 1992 until September 1993. Presentations are restricted to first results only. An extended evaluation including longer time periods will be given later.

In January 1993 a major salt water inflow event renewed the deep water of Bornholm Basin and led to improved oxygen conditions in that area. The salt water inflow marked the end of a 16 year long stagnation period in the Baltic Sea without any deep water renewal. As the Baltic Sea hydrography is determined by river runoff and the limited water exchange through the Danish Straits accurate modelling of salt water inflows are an absolute prerequisite for multi-year simulations of the Baltic Sea. Hence, the latest event with a number of available data sets for validation purposes has been selected.

As RCO has been developed to be coupled to a regional atmosphere model the validation of sea surface variables are important. Sea surface temperature, ice thickness and concentration are determined by atmosphere-ocean interactions. The most likely sources of error within the model are the atmospheric forcing, the bulk formulae for the heat fluxes, the sea ice model, the turbulence model (mixed layer depths) and vertical velocities (up- and downwelling regions).

The mild winter 1992/93 with complete ice coverage in the Bothnian Bay and with partial coverage in the Bothnian Sea and Gulf of Finland provides a first test for the ice model.

In the following, results of the spin-up, the main salt water inflow phase and the seasonal cycle 1992/93 are presented. The variables are sea level records, sea surface temperature, salinity, current velocity, ice thickness and ice concentration maps, vertical cross sections of temperature and salinity, records of isotherm and of isohaline depths.

5.2 Spin-up

As described in Section 2.12 a spin-up from selected observed temperature and salinity profiles has been carried out. The upper panels of Fig.17 and Fig.18 show the sea surface temperature and salinity fields one day after the initialization from May 18, 1992, 00 UTC. During the first 5 days the wind speed is increased linearly and mainly geostrophic currents parallel to the salinity gradients can be observed. The changes in salinity and temperature are small compared to the initial profiles (not shown). Unrealistic sea surface temperature differences between different sub-basins are explained by different observation dates of the profiles (see Tab.2). The timescale of vertical heat exchange with the atmosphere is shorter than the timescale of horizontal advection.

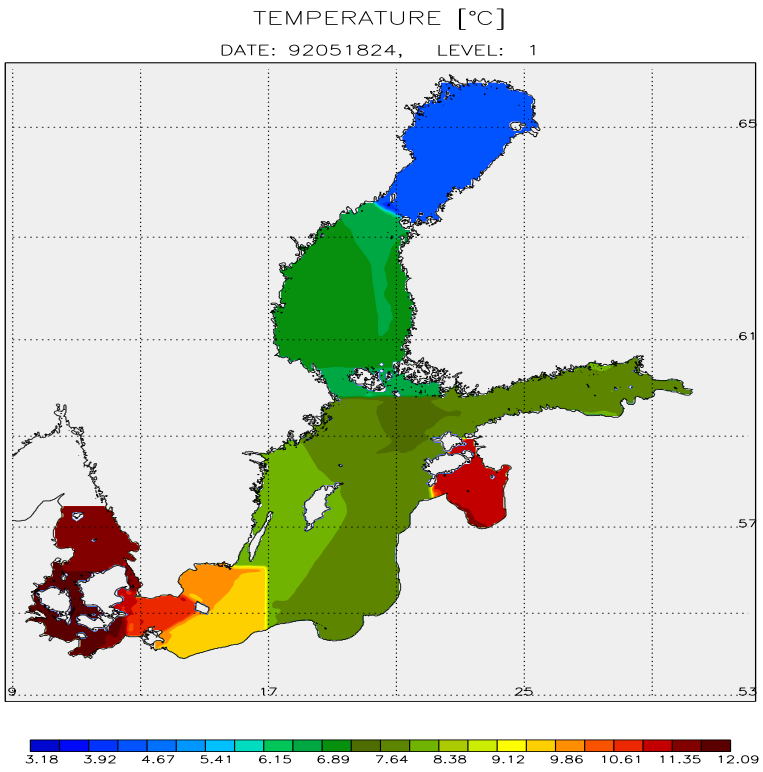

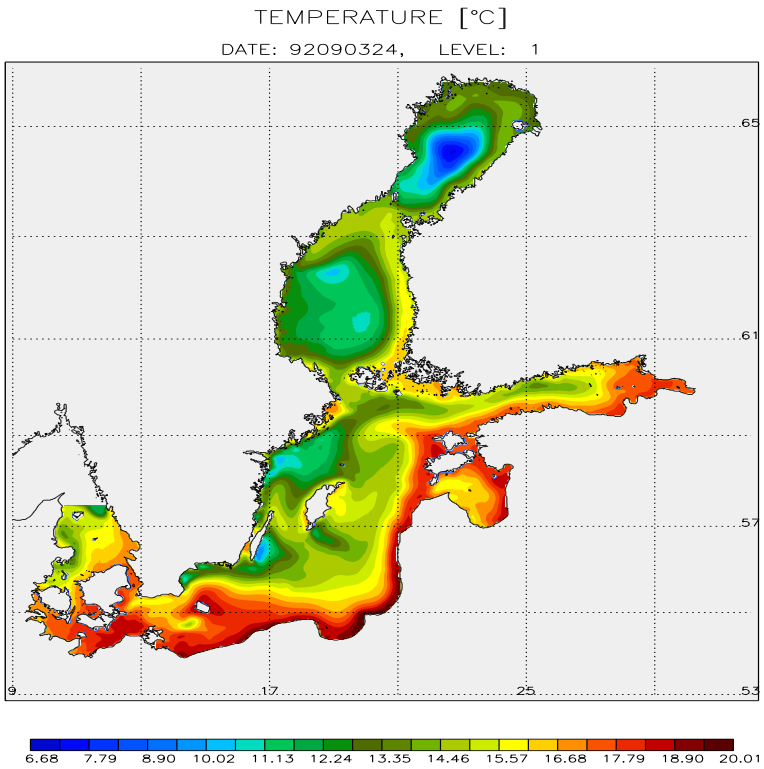

Figure 17: *Sea surface temperature (in °C) from May 18 and September 3, 1992. Different colour bars are used.*

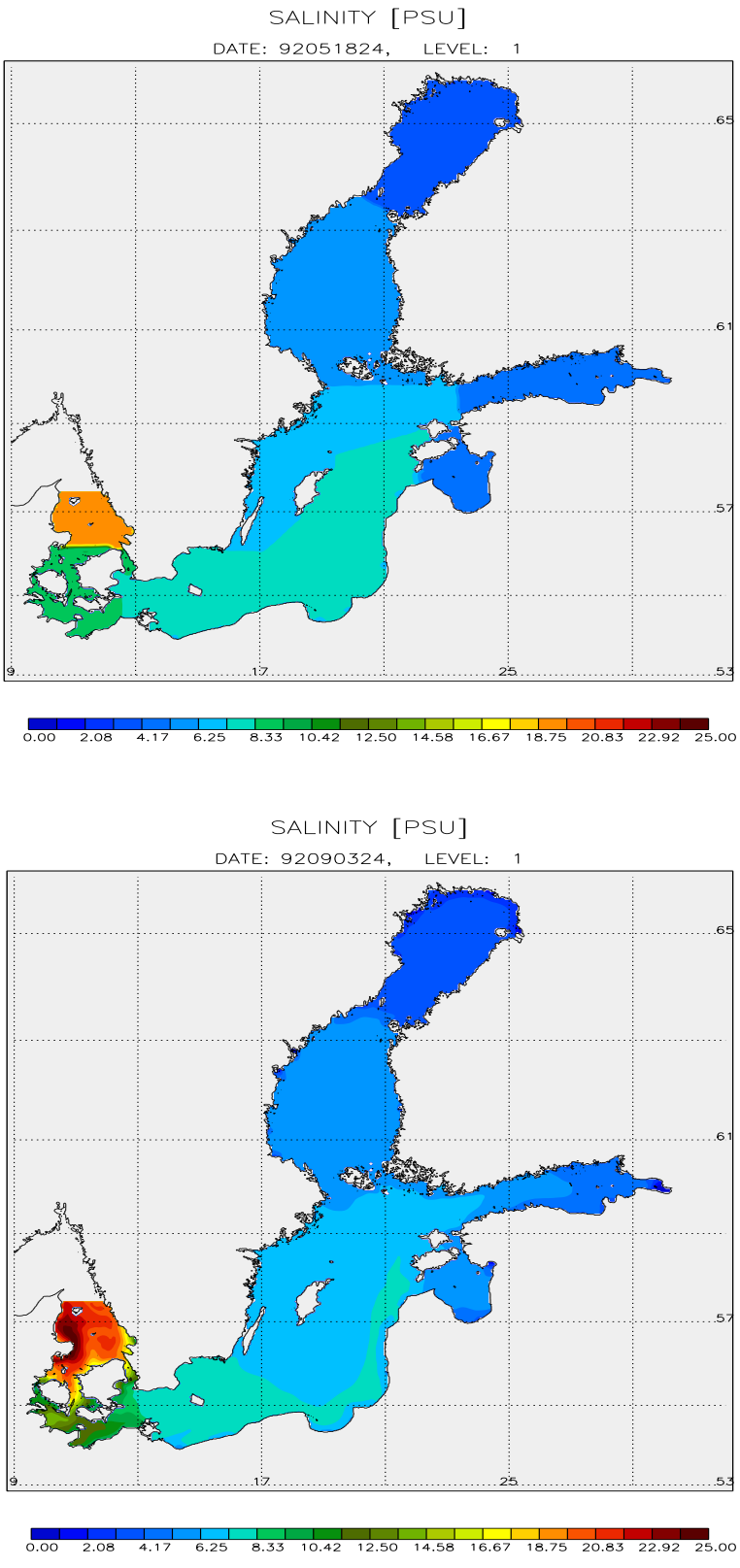

Figure 18: *Sea surface salinity (in PSU) from May 18 and September 3, 1992. The same colour bars are used.*

Contrary, horizontal salt transports dominate vertical freshwater flux in the western Baltic. The lower panels in Fig.17 and Fig.18 show the sea surface temperature and salinity distribution after 109 days of integration (September 3, 1992). The artificial gradients at the sub-basin borders disappeared and physical gradients based on up- and downwelling events (Fig.17) and horizontal current dynamics (e.g., Belt Sea front, Fig.18) have been developed.

The upper panels of Fig.19 and Fig.20 show the initial vertical cross sections of temperature and salinity after one day of integration. Correspondingly, the lower panels of these figures give the results after 109 days of integration. The profiles of the section are taken from Kattegat, Belt Sea, Arkona Basin, Bornholm Basin, Eastern Gotland Basin, Åland Sea, Bothnian Sea and Bothnian Bay. In summer the upper mixed layer has been warmed up and wind mixing in early fall has caused a deep thermocline in September (lower panel of Fig.19). The artificial horizontal gradients between the sub-basins disappeared. After the spin-up period salinity fronts in the Kattegat and Belt Sea are more realistic compared to observations than given by the initial conditions (lower panel of Fig.20).

The presented results show that the spin-up strategy is justified. It is possible to initialize a 3D Baltic Sea model with a set of selected temperature and salinity profiles if no three-dimensional initial fields are available. For simulations longer than a month it is more important to start with realistic vertical stratification in each sub-basin than with realistic horizontal gradients. After 3 months the spin-up period can be considered as finished.

5.3 Sea level

Two tide gauges have been selected and are shown here (Fig.21). Landsort in the Baltic Proper is located close to the nodal line of the main seiches of the system western Baltic Sea and Gulf of Finland (58.738^oN, 17.870^oE). Hence, this tide gauge is representative for volume changes of the Baltic Sea. The second tide gauge, Ratan, is located at the end of the Gulf of Bothnia in the narrow between the Bothnian Sea and Bothnian Bay (63.983^oN, 20.900^oE). Hence, sea level data from this tide gauge show oscillations with periods of a few days which are explained by wind stirred seiches ($31.03\,h$, Wübber and Krauß, 1979) and piling ups of water on synoptic timescale. In Fig.21 absolute sea level elevations are shown referred to the Nordic height system NH 60 from Ekman and Mäkinen (1996). From the observed sea level data the mean of the simulation period have been subtracted and replaced by the mean sea surface topography. As only 501 days are considered land uplift with a maximum of $1\,cm/year$ in the Bothnian Bay according to Ekman (1996) must not be taken into account (contrary to multi-year integrations).

The agreement between observed and modelled sea levels is strikingly. As volume changes are modelled realistically (see Landsort tide gauge) the sum of volume transports through the Danish Straits and river runoff into the Baltic Sea are simulated

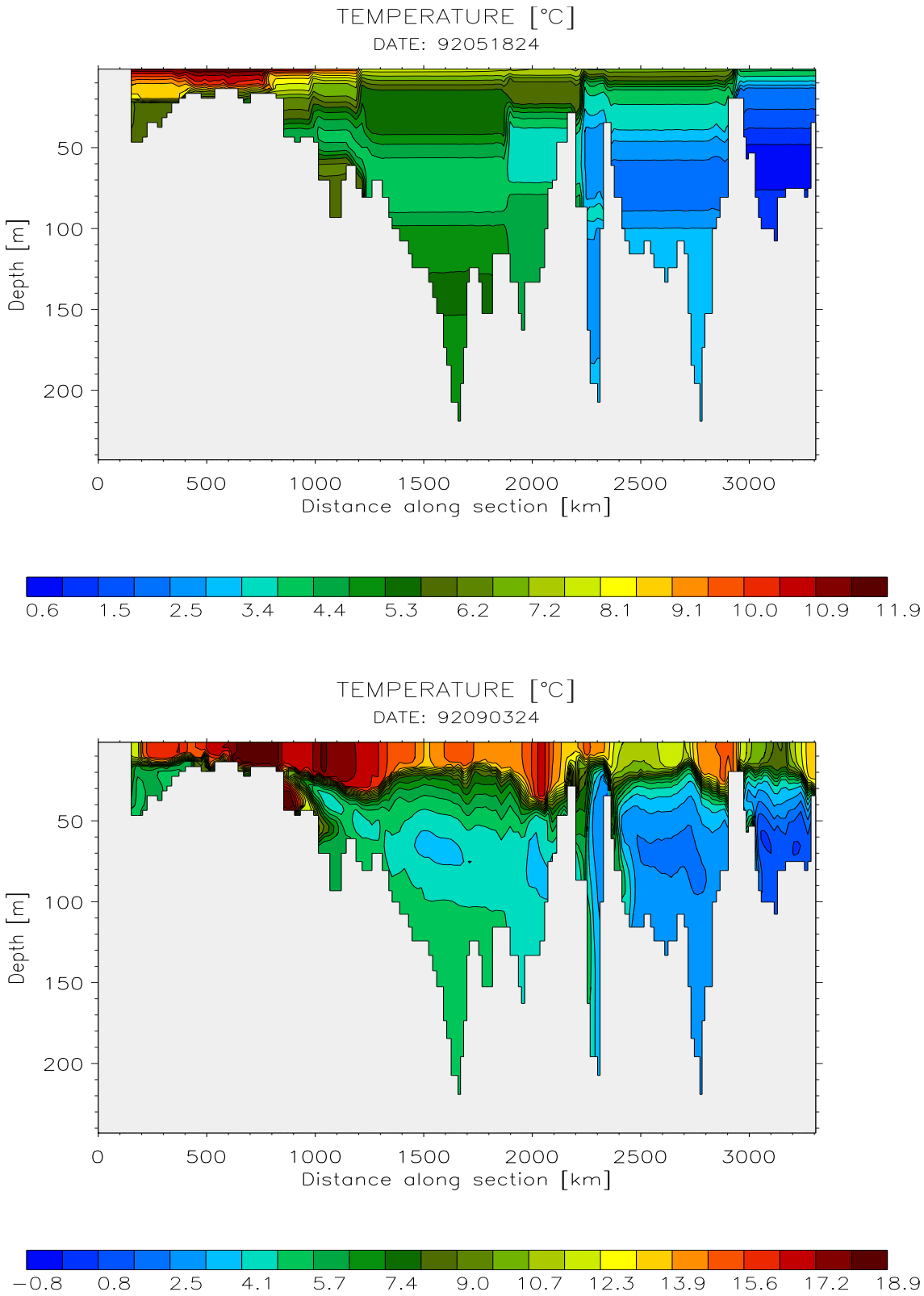

Figure 19: *Temperature section (in °C) through the whole Baltic Sea from Kattegat to Bothnian Bay from May 18 and September 3, 1992. Different colour bars are used.*

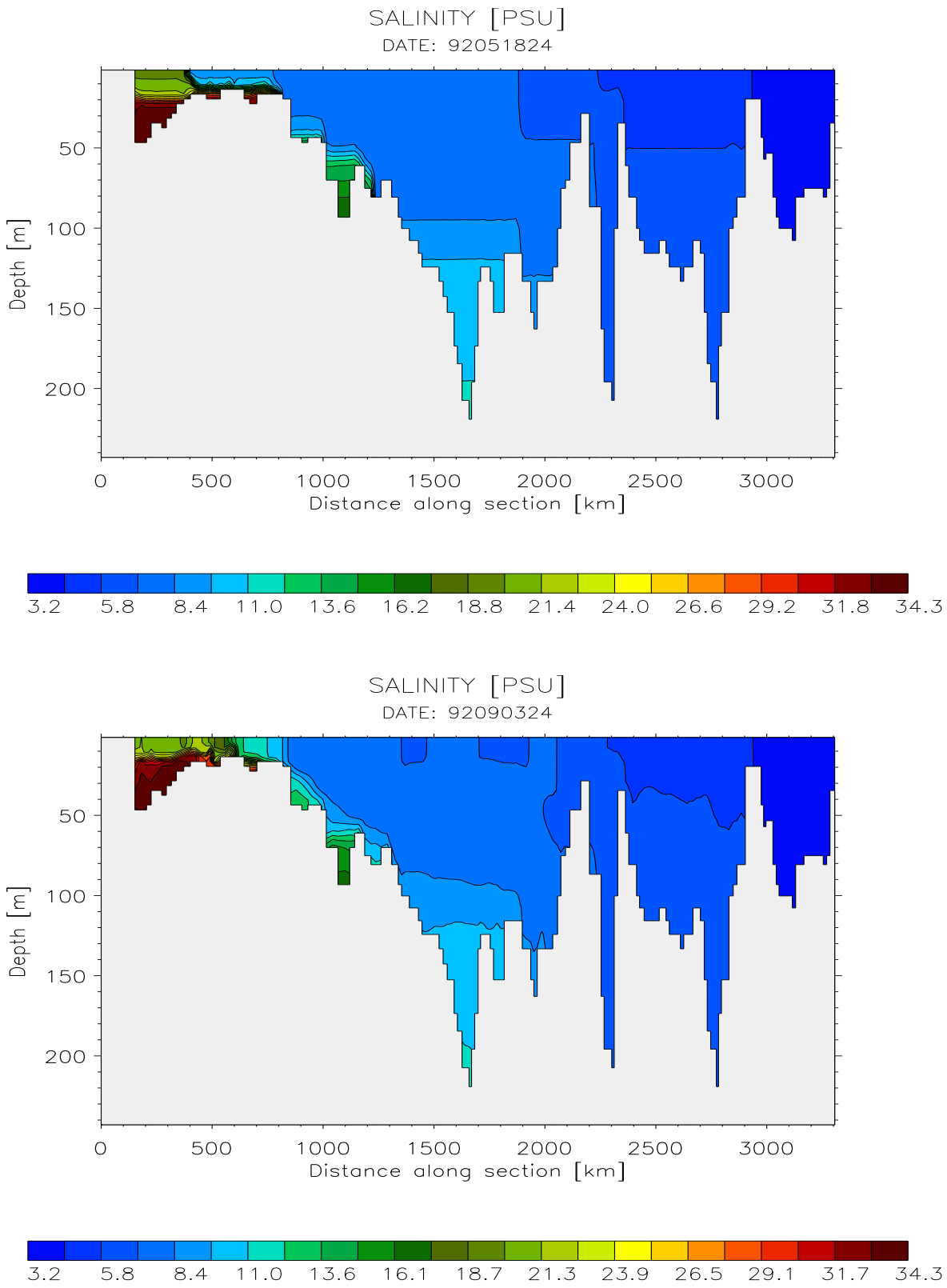

Figure 20: *Salinity section (in PSU) through the whole Baltic Sea from Kattegat to Bothnian Bay from May 18 and September 3, 1992. The same colour bars are used.*

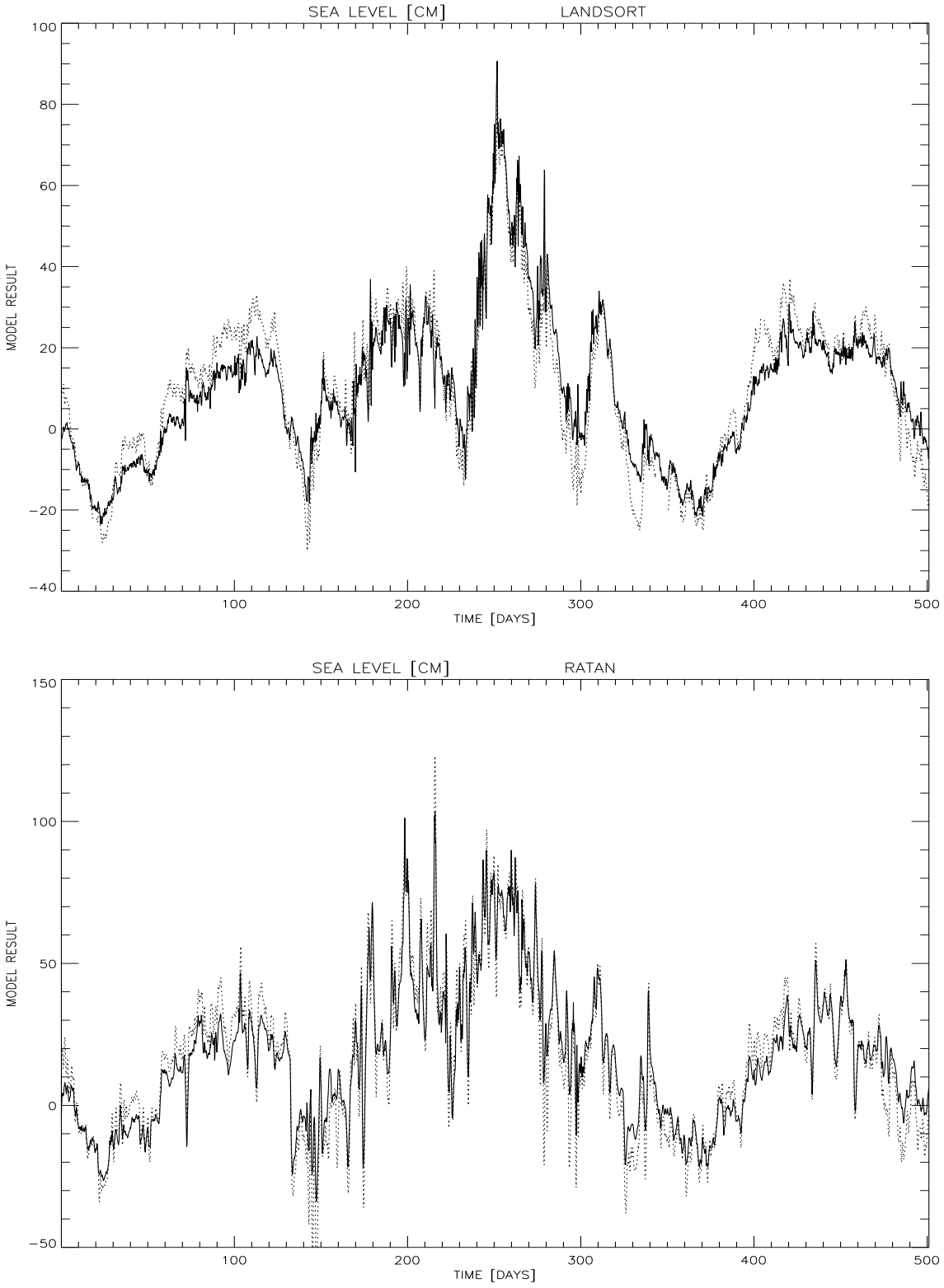

Figure 21: *Sea level data (in cm, dashed line) from the Swedish tide gauges Landsort in the Baltic Proper (upper panel) and Ratan in the Gulf of Bothnia (lower panel) compared with model results (solid line).*

correctly. The realistic simulated amplitudes and phases of observed oscillations from the tide gauge Ratan are confirmations of correct parameterized bottom friction (i.e., the bottom drag coefficient c_b) and the atmospheric forcing (i.e., the surface wind fields and pressure gradients).

5.4 Sea surface temperature

Modelled sea surface temperature fields are compared with ice-sst charts from observations published by SMHI regularly twice a week ("isläge and ytvattentemperaturer"). Selected are snapshots from summer 1992 and 1993 with high temperatures (Fig.22 and Fig.26), from the cooling period in late autumn 1992 (Fig.23) when the first ice has been developed, from the maximum ice extent in winter 1993 (Fig.24) and from the warming period in spring 1993 (Fig.25) when the ice just melted.

August 1992 has been quite warm with observed temperatures of more than $20\,^oC$ (Fig.22). Close to the Swedish coast upwelling regions were developed in the Northwestern Gotland Basin, the Bothnian Sea and the Bothnian Bay with temperatures less than $8\,^oC$. The corresponding model snapshot shows the same distribution of up- and downwelling regions but the maxima and minima are overestimated, i.e., upwelling regions close to the eastern coasts are too warm and downwelling regions are too cold. The pronounced warm coastal waters are amplified by the reduced wind speed parameterization according to Bumke (1997, pers.comm.) but the main reason for the artificial warming is not yet clear. Temperatures in the center of the sub-basins are slightly too cold.

Around November 2, 1992 the first ice in the Bothnian Bay was observed and coastal waters were colder than central basins (Fig.23). The model results are in good agreement with observations. Details like maxima in the Northwestern Gotland Basin and in the Arkona Basin (about 11^oC) or the minimum south of Gotland are simulated. Differences exist in the Bothnian Sea.

Sea surface temperature under sea ice equals freezing point temperature. Hence, the ice extent is marked by the area with freezing point temperature approximately (Fig.24). The depicted results are received using the ocean model without sea ice model. In the model the temperature is restricted by the freezing point temperature simply. Results with sea ice model included are shown below and as cover illustration. The maximum of 1^oC in the ice free central Bothnian Sea is modelled correctly. The temperatures of the Baltic Proper are simulated in the correct range between 3 and 4^oC and also the gradients towards colder coastal waters are reproduced in RCO.

The first day in 1993 without any sea ice is May 27 (Fig.25). Coastal waters were much warmer than the interior of the basins. The overall temperature distribution is simulated right. The minimum of 1^oC in the central Bothnian Bay is correctly modelled whereas the minimum of 5^oC in the central Bothnian Sea is lower with $3-4^oC$ approximately. Some local features like the upwelling region east of Gotland can be

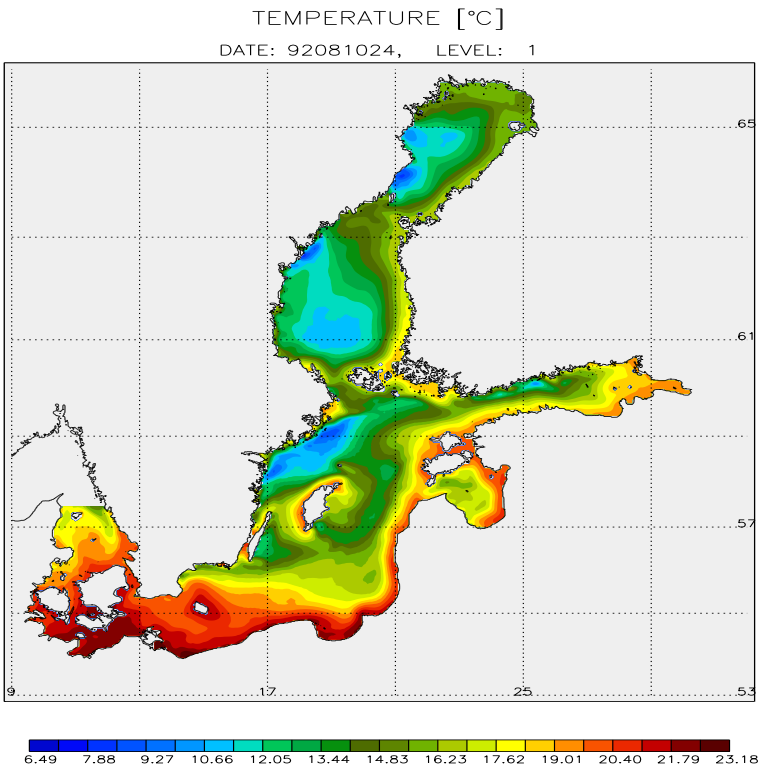

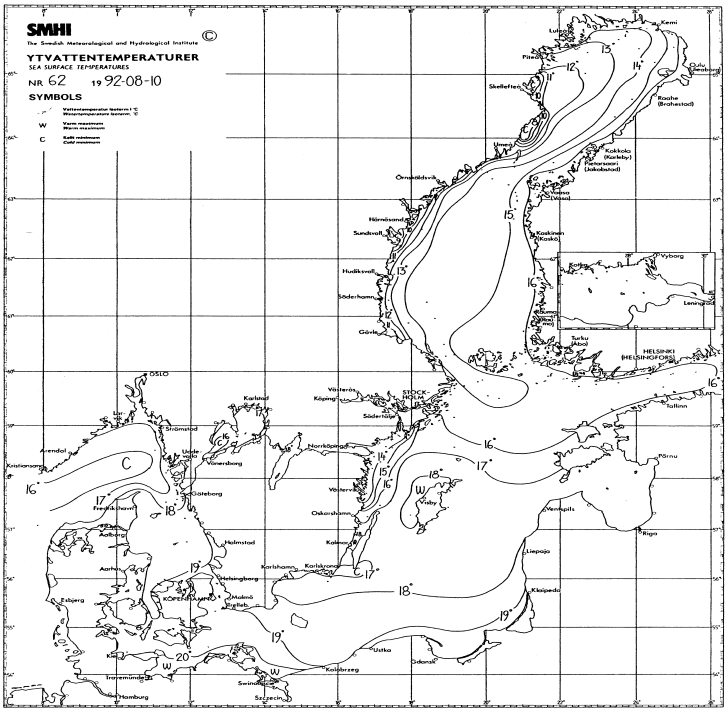

Figure 22: *Modelled sea surface temperature (in °C) from August 10, 1992, compared with the corresponding sst chart published by SMHI.*

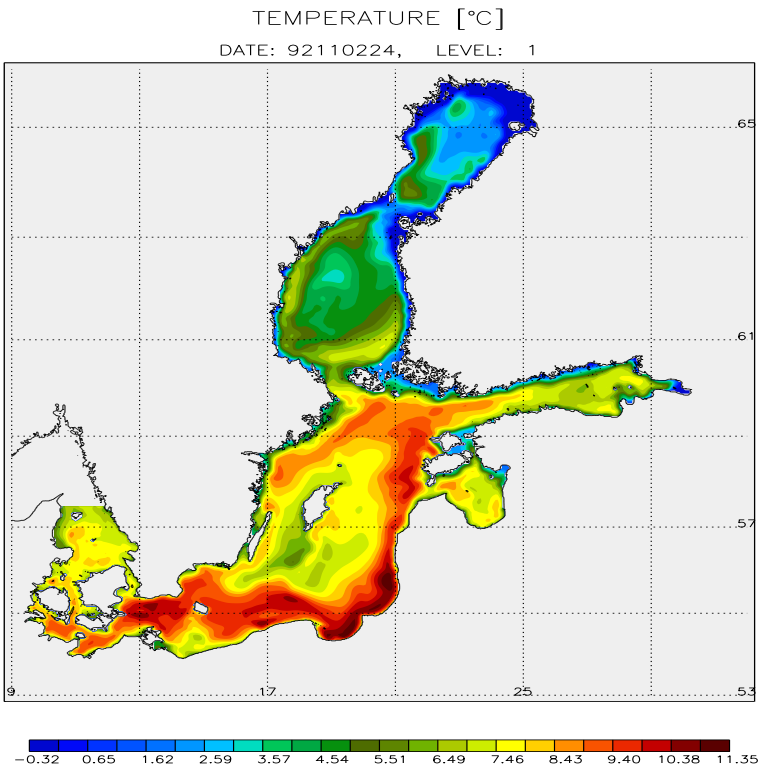

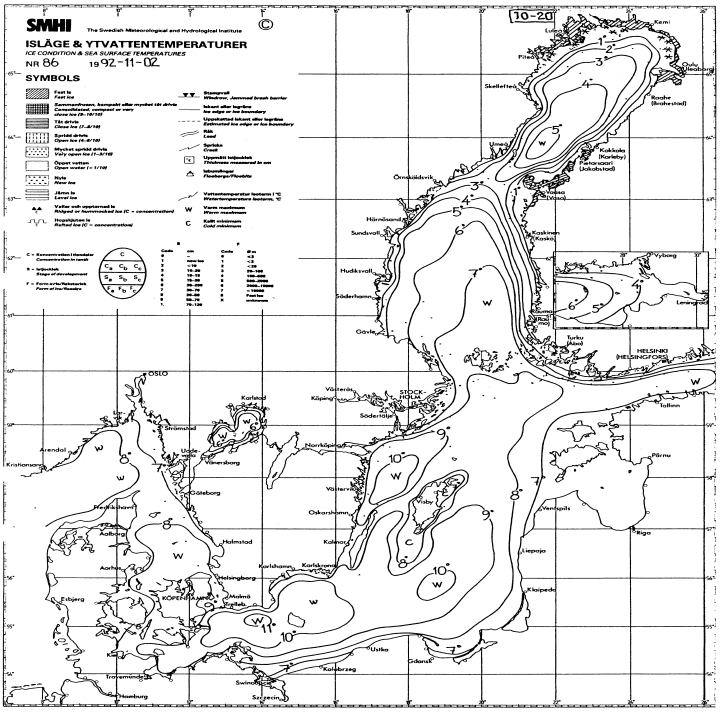

Figure 23: *Modelled sea surface temperature (in °C) from November 2, 1992, compared with the corresponding sst chart published by SMHI.*

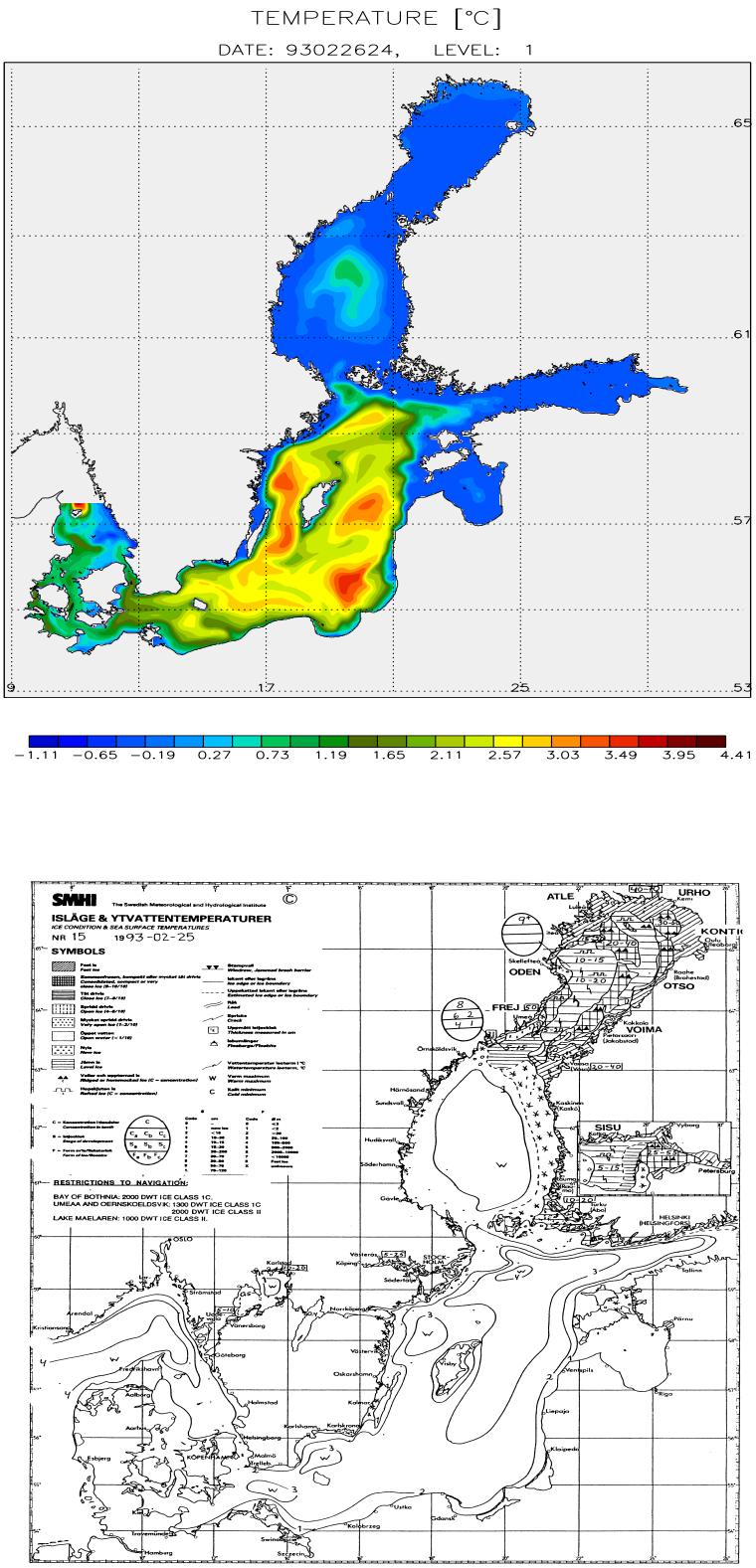

Figure 24: *Modelled sea surface temperature (in °C) from February 26, 1993, compared with the corresponding ice-sst chart published by SMHI from February 25, 1993.*

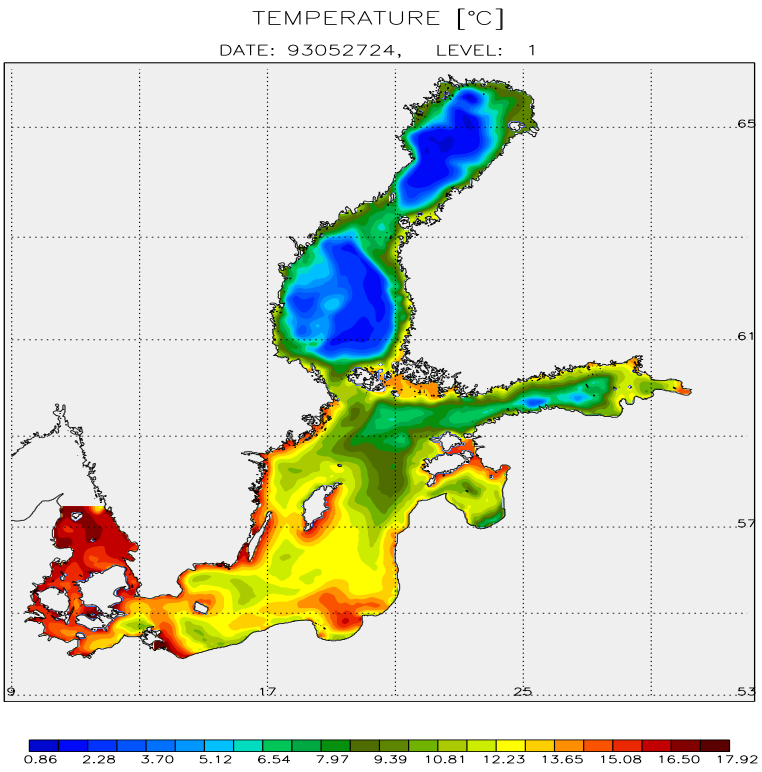

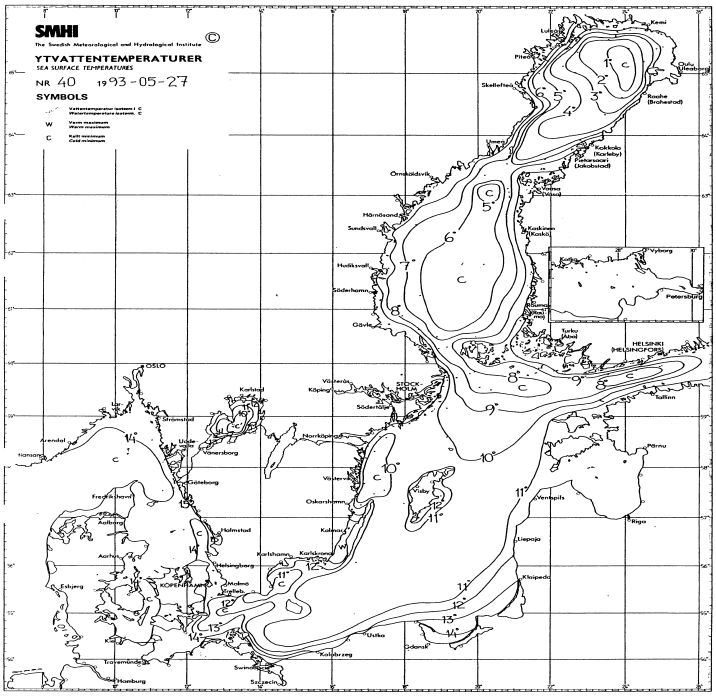

Figure 25: *Modelled sea surface temperature (in °C) from May 27, 1993, compared with the corresponding sst chart published by SMHI.*

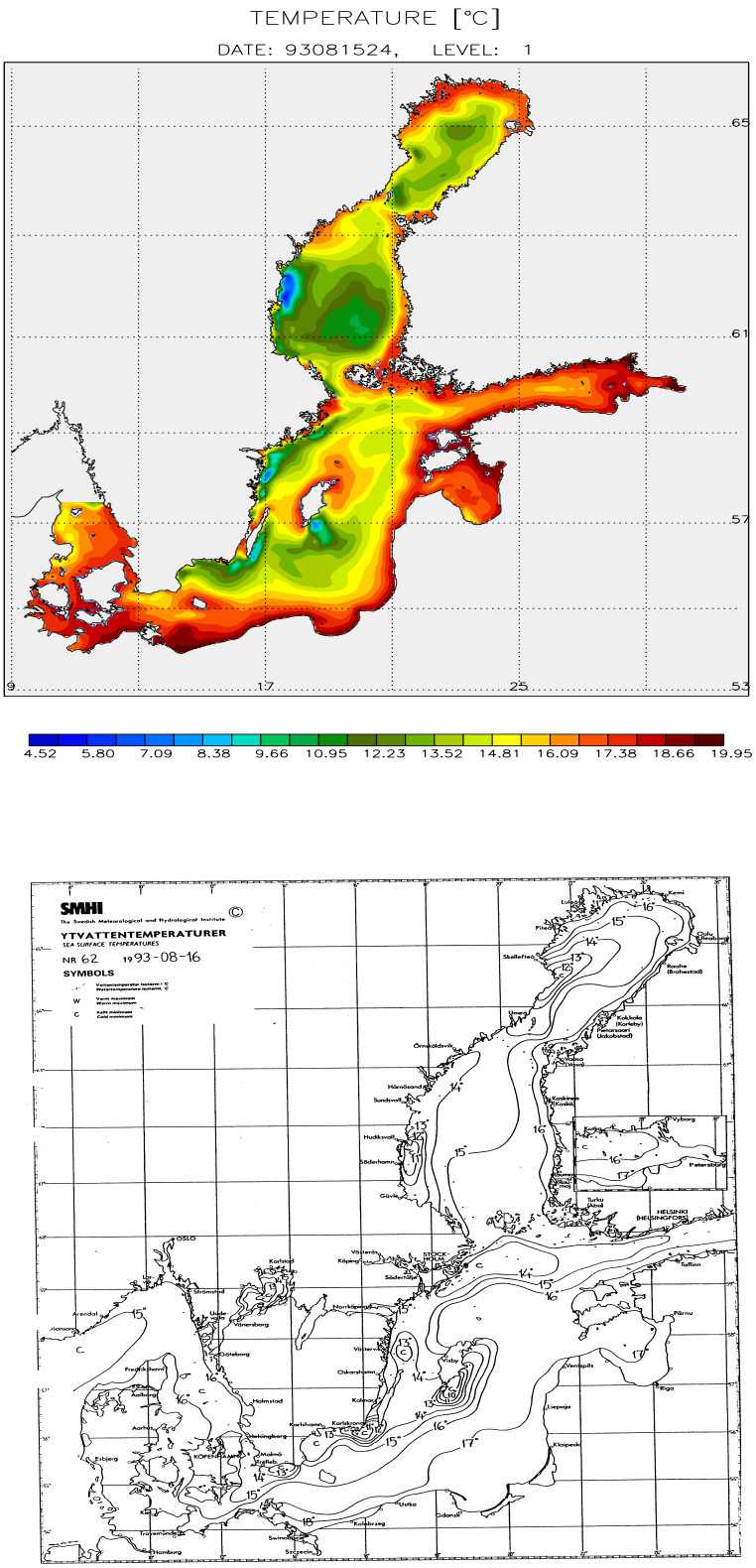

Figure 26: *Modelled sea surface temperature (in °C) from August 15, 1993, compared with the corresponding sst chart published by SMHI from August 16, 1993.*

localized also in the model. Temperatures between 10 and 11^oC were observed in the central Gotland Basin. RCO is in good agreement with these measurements. Maxima in Kattegat, Belt Sea and near the island Rügen are higher in the model with about 2 ^oC probably.

The summer 1993 was much colder than the previous one. No temperatures higher than 18^oC were observed (Fig.26). At August 16, 1993, pronounced downwelling regions occurred with sea surface temperatures less than 10^oC in some cases. As in most well developed up-/downwelling situations RCO under/overestimated sea surface temperatures at that locations but the modelled area extents agree well with observations.

The SMHI maps are not necessarily identical to reality. Generally, the maps are too smooth due to the lack of observations and due to the interpolation algorithm. Satellite data show much more mesoscale variability than the charts and look like model results. For example missing upwelling regions might be not observed and for that reason not included in the charts.

5.5 Mixed layer depth

In Fig.27 modelled isotherm depths at Bornholm Deep for the simulation period are shown. As mentioned already in connection with the sea surface temperature the sum-

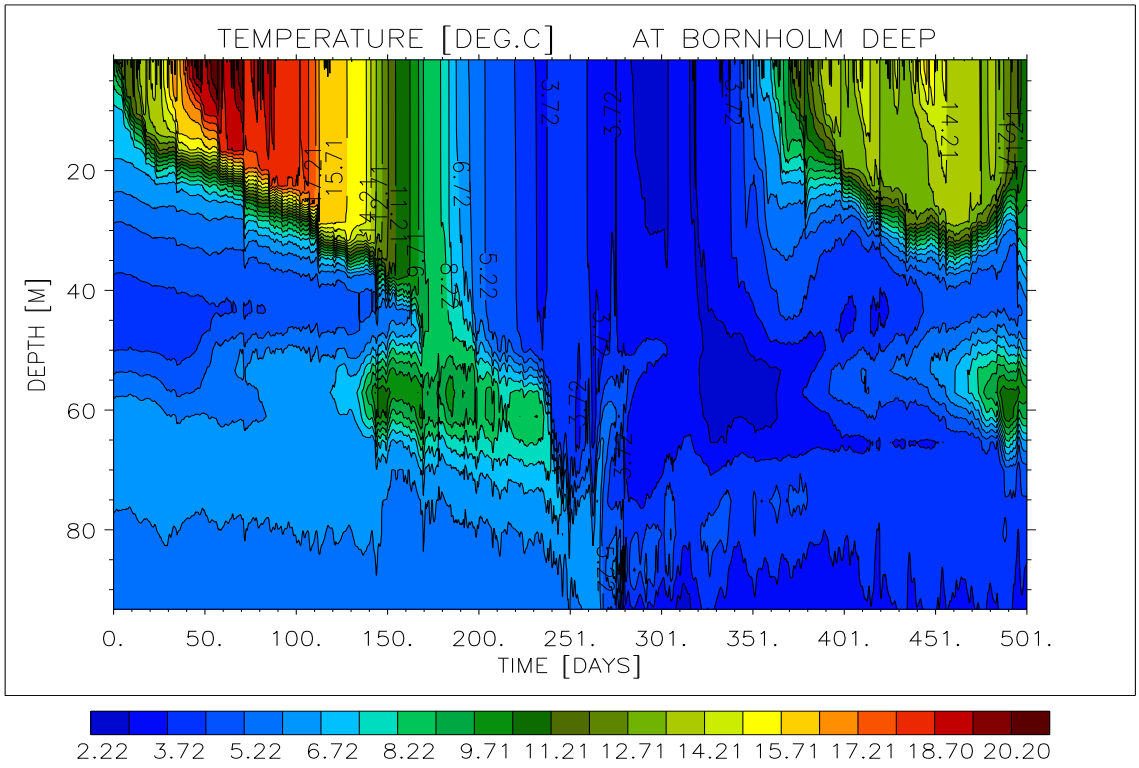

Figure 27: *Isotherm depths (in °C) from May 18, 1992, until September 30, 1993, at Bornholm Deep.*

mer 1992 was much warmer than the summer 1993 with maximum temperatures in Bornholm Basin of $21\,^{o}C$ and $17\,^{o}C$, respectively. The interannual variability is captured by RCO. Mixed layer depths are simulated correctly. Profile data for comparison were published by Meier (1996). Between 40 and $50\,m$ winter water above the halocline can be observed from the initial conditions. In winter 1993 new winter water has been formed. In the depth range of the halocline between 50 and $70\,m$ in autumn 1992 and 1993 warmer saline water is intruded. This water has been advected from the Arkona Basin horizontally. After the salt water inflow in January the bottom water in the Bornholm Basin has been replaced by more saline and colder water of less than $5^{o}C$.

5.6 Salt water inflow

At the end of December 1992 and during the first days in January 1993, a distinct outflow situation is established with low salinities in the Danish Straits (Fig.28 and 29). After the onset of strong westerly winds the salinity fronts are moved towards Arkona Basin and the Belt Sea is filled up with salty water (see results from January 17). Maximum current velocities of about $2\,m/s$ are modelled. Between January 6 and 27, a mean salinity of 26.75 PSU was observed at Drogden Sill (Håkansson et al., 1993). At Darss Sill mean maximum salinities of about 22 PSU were observed between January 26 and 28 (Matthäus et al., 1993). As time proceeds (see results from January 25) the model describes the filling up of Arkona Basin with the inflowing salty water (upper panel of Fig.30). There are no data available which elucidate this process directly. For comparison the reader is referred to Meier (1996, see his Fig.50). At the end of January the amount of inflowing salty water across Drogden and Darss Sill into Arkona Basin is greater than the outflow through Bornholm Channel into Bornholm Basin. Hence, the halocline in the Arkona Basin is lifted above the level of Darss Sill by the end of the inflow event in correspondence with data (Matthäus and Lass, 1995). Modelled maximum bottom salinities at Arkona Deep are $23.9\,PSU$ (upper panel of Fig.30) in agreement with observations ($24 - 25\,PSU$). At January 29 again outflow occurred (Fig.28 and 29). The inflowing water sank to the bottom of Bornholm Basin penetrating below the old bottom water which was lifted up (lower panel of Fig.30). Modelled maximum bottom salinities at Bornholm Deep are $17.0\,PSU$ whereas $18 - 19\,PSU$ were observed. The model slightly underestimates the amount of saline water flowing from Arkona to Bornholm Basin downhill. The shortcomings of coarse resolution level models in case of overflow situations have been reported in the literature (e.g., Beckmann and Döscher, 1997). Meier (1996) showed that the results will be even better if a horizontal resolution of $1\,nm$ is used.

The simulated overflow is sensitive to initial stratification, atmospheric forcing, sea level differences between Kattegat and western Baltic Sea, mixing parameterization and grid resolution. Here, we report only from a series of sensitivity experiments concerning salinity at the open boundary in the northern Kattegat. The results of Fig.30 are obtained using prescribed salinities of $25\,PSU$ for depths smaller than $13.5\,m$ and of $35\,PSU$ for greater depths. During the whole simulation period these constant values are used. In the reference experiment as described in Section 2.7.4 a mean profile from

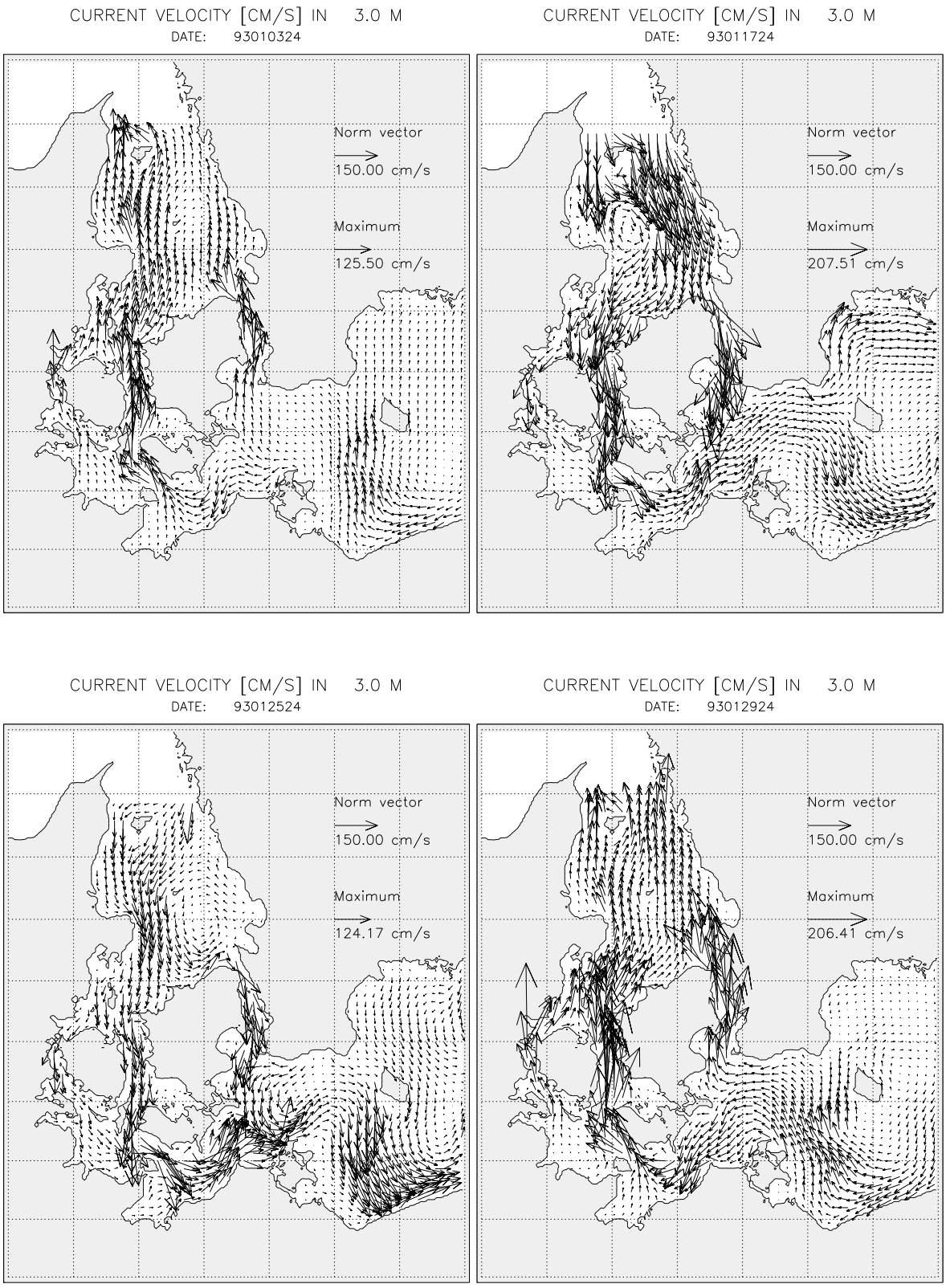

Figure 28: *Sea surface currents (in cm/s) in the western Baltic Sea from January 3, 17, 25 and 29, 1993.*

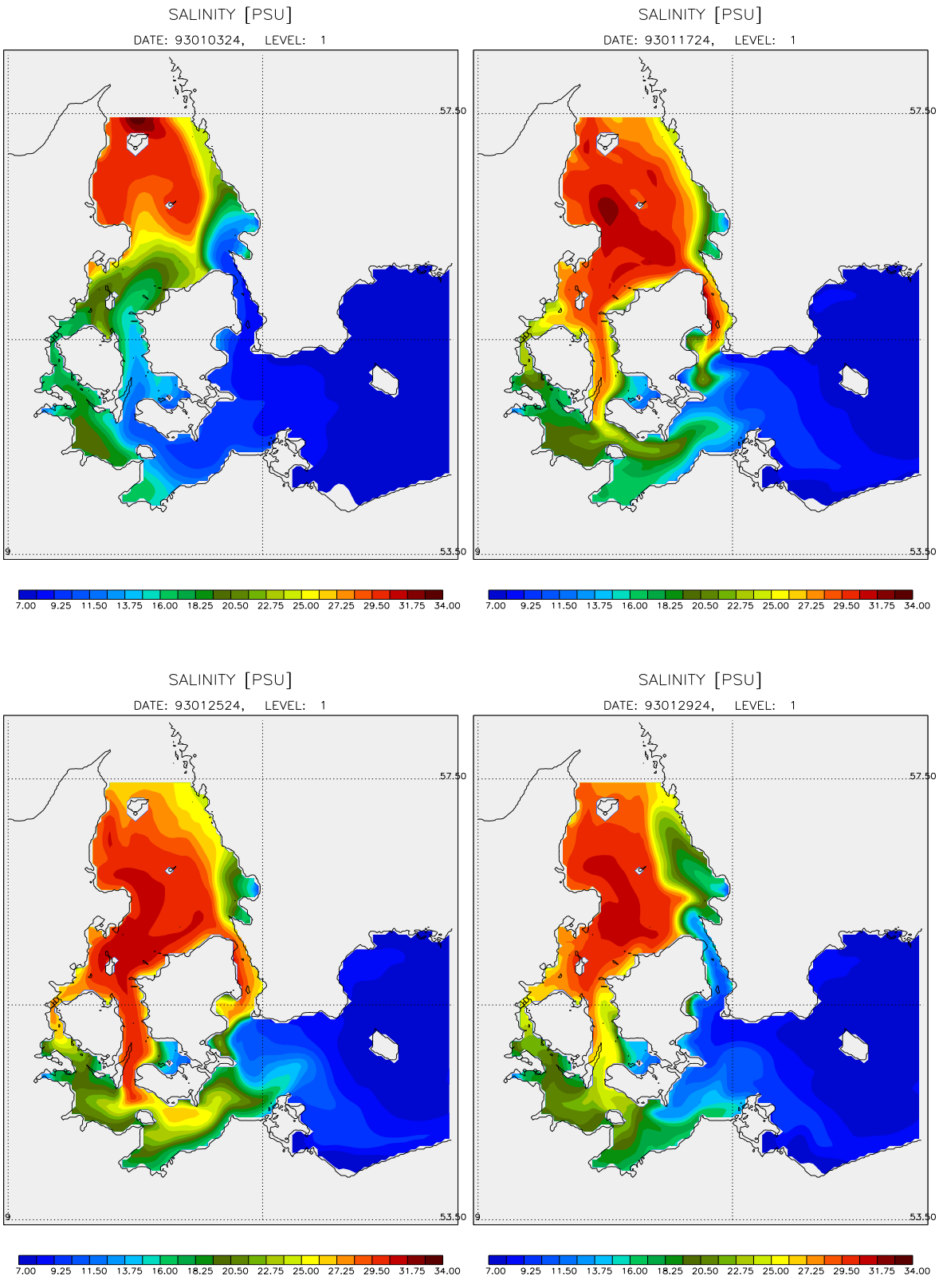

Figure 29: *Sea surface salinity (in PSU) in the western Baltic Sea from January 3, 17, 25 and 29, 1993.*

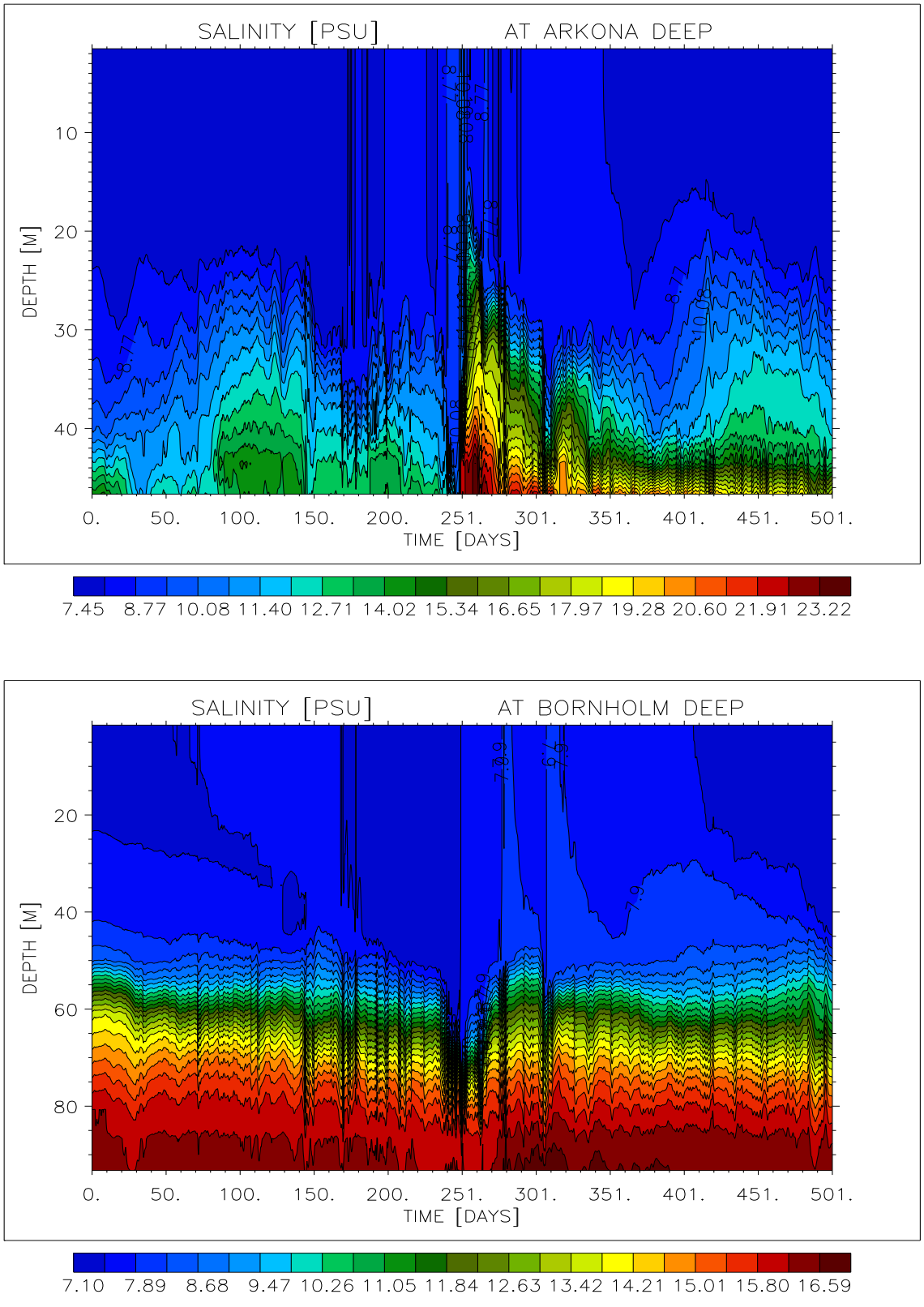

Figure 30: *Isohaline depths (in PSU) from May 18, 1992, until September 30, 1993, at Arkona Deep (upper panel) and Bornholm Deep (lower panel).*

observations at Anholt East is implemented. The salinities vary between 19.9 PSU close to the surface and 33.5 PSU at the bottom. The results show no inflow into the Bornholm Basin and no replacement of the lower layer water at all. The bottom salinity at Arkona Deep increases temporarily to 21.6 PSU whereas at Bornholm Deep the salinity decreases after the inflow. A third experiment has been performed with a boundary profile which equals Anholt East mean salinity during most of the integration period but is increased during the inflow period temporarily. Between January 5 and 27 the salinities vary as in the first experiment, i.e., 25 PSU for depths smaller than 13.5 m and 35 PSU for greater depths. The maximum bottom salinity at Arkona and Bornholm Deep are now 23.0 PSU and 16.3 PSU, respectively. The Bornholm Basin deep water is not really renewed.

The three experiments show that the upper layer salinity at the northern model boundary influences the solution of the model interior. The preconditioning of stratification in Kattegat is important for salt water inflows not only during but also before the event. This finding emphasizes again the need for adequate boundary conditions in Kattegat. Thus, a North Sea model and a barotropic model for parts of the North Atlantic is projected for future model development.

5.7 Sea ice

5.7.1 Including dynamic effects

The full Rossby Centre ice model has been applied in conjunction with the Rossby Centre ocean model for the first time. A full 2-way coupling according to Section 3.4 is employed. In this section, we present first results from a simulation of the winter 1992/93 using a horizontal resolution of 6 nm. As only one ice class is considered, a parameterization for ridged ice appears to be necessary. Here, we have utilized a simple approach reducing thermal conductivity if the ice thickness exceeds 20 cm. Correspondingly, Omstedt and Nyberg (1995) neglected the thermodynamic growth/decay functions for ridged ice.

The overall relatively mild winter 1992/93 in its coldest phase typically showed a nearly full coverage of the Bothnian Bay, coastal ice in the Bothnian Sea and a coverage in the eastern part of the Gulf of Finland. Fig.31 (upper) shows the mean thickness at February 25, which represents the maximum ice extent. The Bothnian Bay is completely covered with mean ice thicknesses (concentration $\times$ thickness) ranging from 15 to 47 cm. High concentrations (Fig.32, upper) of more than 0.8 are dominating. The Bothnian Sea shows partial ice cover along the coast lines with mean thicknesses of 10 - 15 cm. Furthermore, the Gulf of Finland shows ice up to 30 cm thick. Some areas in the Gulf of Riga are covered. Observations of the ice situation (SMHI maps) are collected in Fig.31 (lower) and correspond very well with the simulation. The contours of the ice edge are nearly identical. Specific features like ice coverage east of the Ålands and in the Gulf of Riga match nearly perfect. Given the sensibility of the ice model to sst distribution, this similarity points to a carefully adjusted mixed layer model and

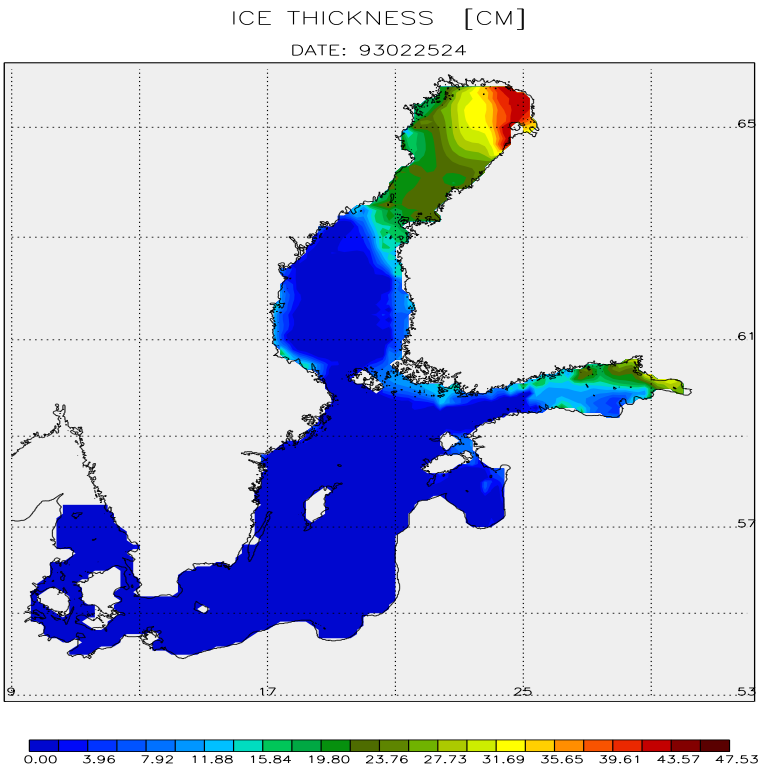

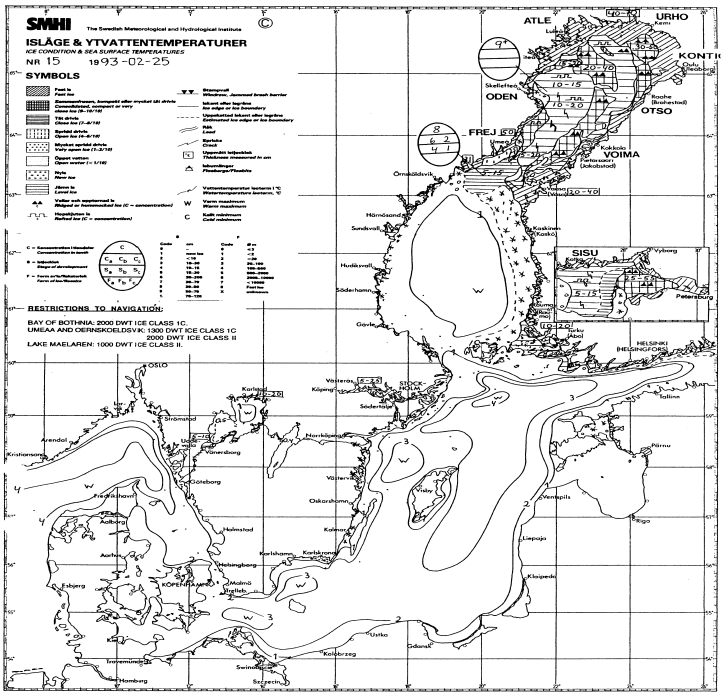

Figure 31: *Modelled mean ice thickness (in cm) from February 25, 1993, compared with the corresponding ice-sst chart published by SMHI.*

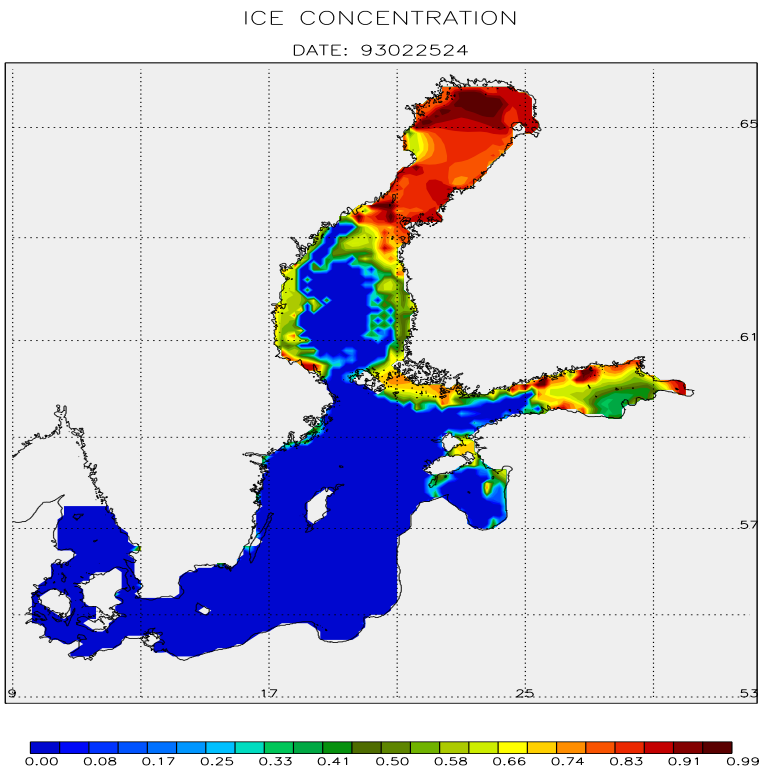

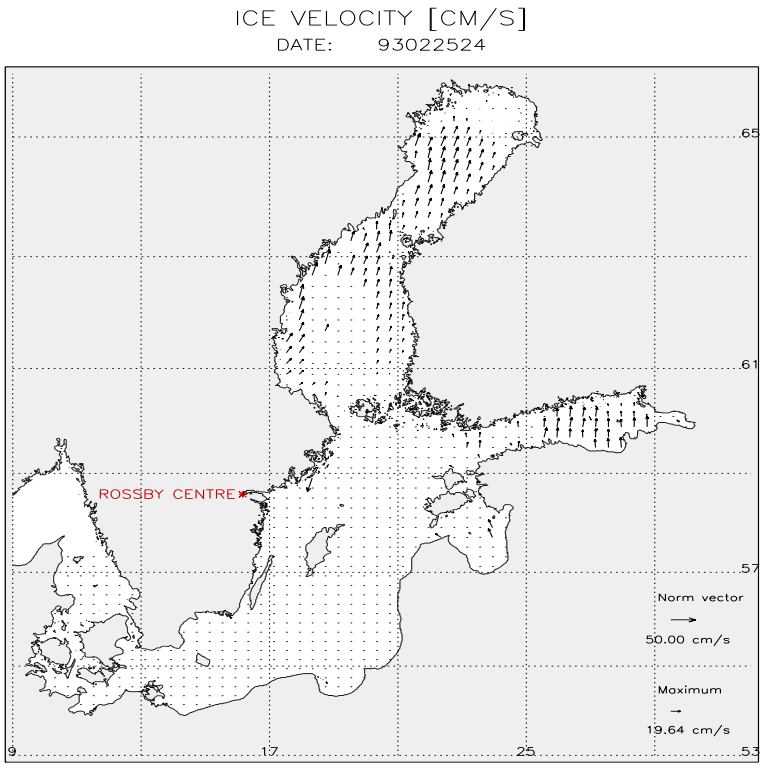

Figure 32: *Modelled ice concentration and ice velocity (in cm/s) from February 25, 1993.*

other ocean model parameterizations. Ice thickness also compares well with observations: both show a general increase from south-west to north-east in the Bothnian Bay. This is likely related to the predominantly north-eastward drift as indicated by Fig.32 (lower). Thickness realisticly reaches about 50 cm. There is only a slight hint to a thick-thin-thick structure as can be seen in the observations. This points to possible future improvements: a better fine-tuning, and ridged ice may be treated more elaborately.

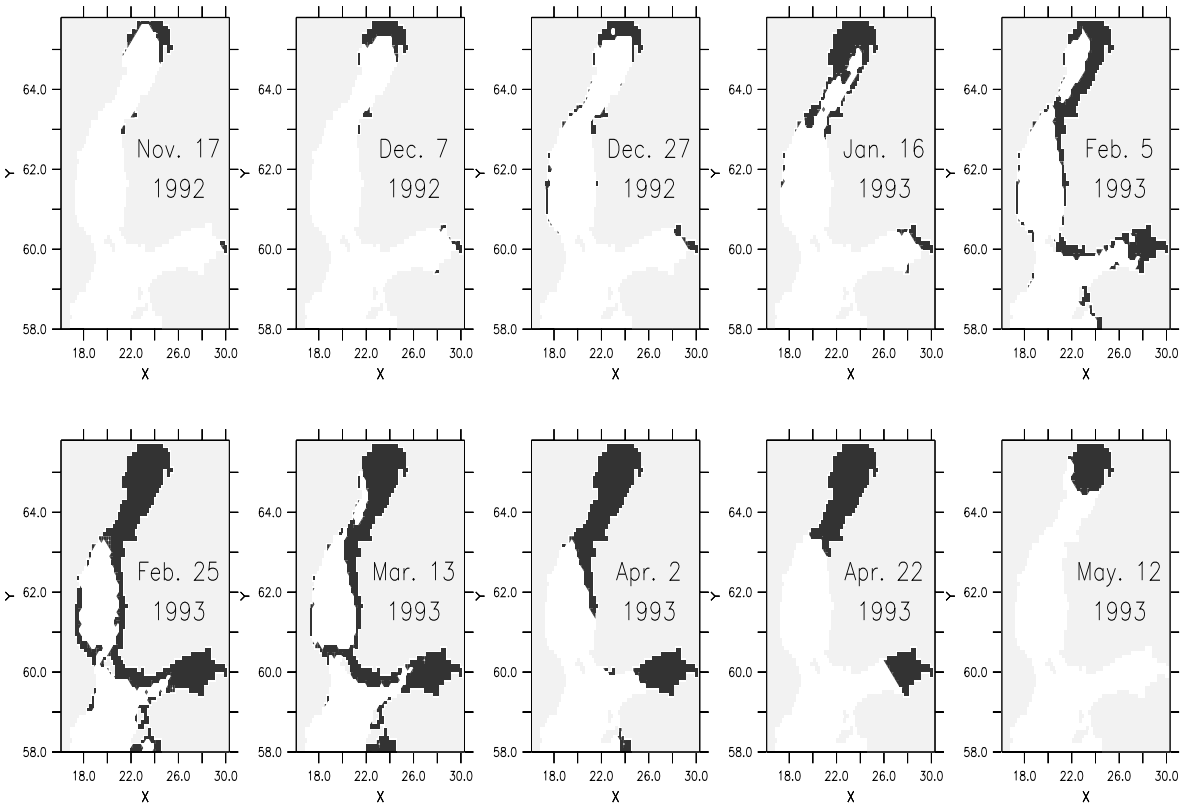

Figure 33: *Simulated ice covered areas for the winter 1992/1993 in a time sequence of 20 days interval. A mean thickness $ch > 2$ cm has been used as a criterion to identify ice areas.*

The simulated ice extent in a sequence of snapshots is displayed in Fig.33. The annual cycle can be seen in intervals of 20 days. Simulated ice formation starts at October 20 (October 22 observed) in the Lumijoen Bay off Oulu. Until December 27, ice is confined to the northern parts of the Bothnian Bay and some narrow coastal areas. This is followed by a strong lateral growth. At February 5 a hole has opened due to a strong westerly wind event. Further lateral growth occurs until the maximum ice extend is reached at March 3 (February 25 observed). During March and April, ice retracts and vanishes at May 14 (May 24 observed).

The annual cycle of ice covered area of the whole Baltic is given by Fig.34. A slow

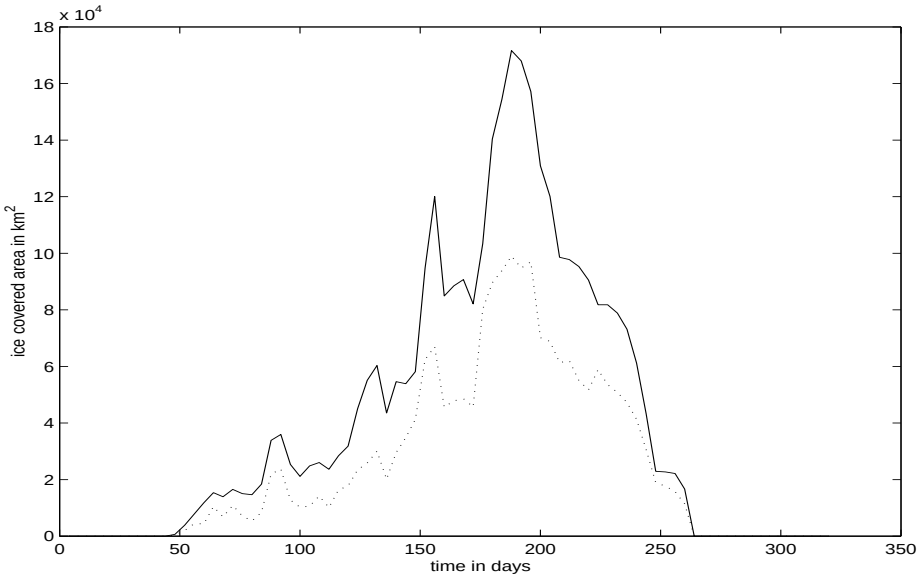

Figure 34: *Simulated ice covered area in* $10^{10}m^2$ *for the winter 1992/1993. The dotted curve takes ice concentration into account whereas the solid curve does not (see text).*

increase until December 20 is followed by a more rapid increase to the maximum at March 3. The ice vanishes within the next 2 months. The summed surface area of ocean grid-boxes which contain ice is given by the solid curve, generally representing the area north of the ice edge. The dotted curve takes the ice concentration into account, thus can be regarded as the appropriate measure of ice cover. Maxima of $170 \cdot 10^9 m^2$ or $100 \cdot 10^9 m^2$ are reached. Omstedt and Nyberg (1996), show a maximum ice extend of $136 \cdot 10^9 m^2$, i.e., $36 \cdot 10^9 m^2$ above our second result. Omstedt and Nyberg (1996) simulate the complete period 1980 - 1993. Thereby, their ice cover exceeds the observations from SMHI and FMI by $18 \cdot 10^9 m^2$ in the mean. However, the winter 1992/93 which we use here as a first test, shows greatest deviations between model and observations ($66 \cdot 10^9 m^2$ overestimation for Omstedt and Nyberg (1996) and $30 \cdot 10^9 m^2$ in our case). As the observed number of $70 \cdot 10^9 m^2$ is not supported by the observed ice edge line, either low concentrations or observation uncertainties must be involved. Summarizing, first results indicate that the ice covered area in RCO is within the range of established Baltic Sea ice models. Further testing of the Rossby Centre ice model for more than one winter will be necessary to get a clearer picture.

An interesting wind situation occurs between January 28 and February 5. Initially (Fig.35 and 36), a nearly full coverage of the Bothnian Bay with a maximum thickness of 25 cm and with an offshoot into the Bothnian Sea is given by the model. This general situation is confirmed by the observation. The offshoot can be explained by

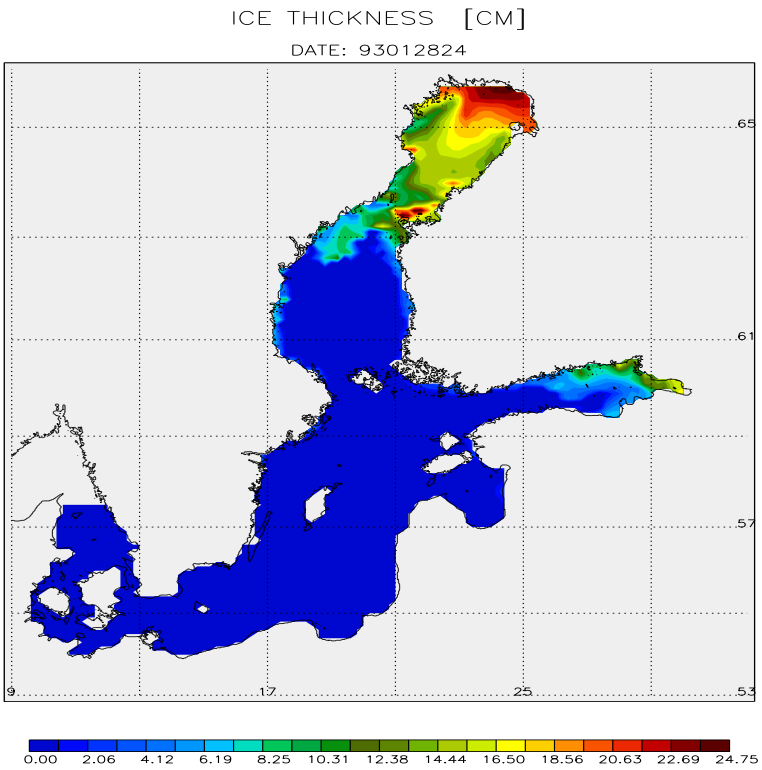

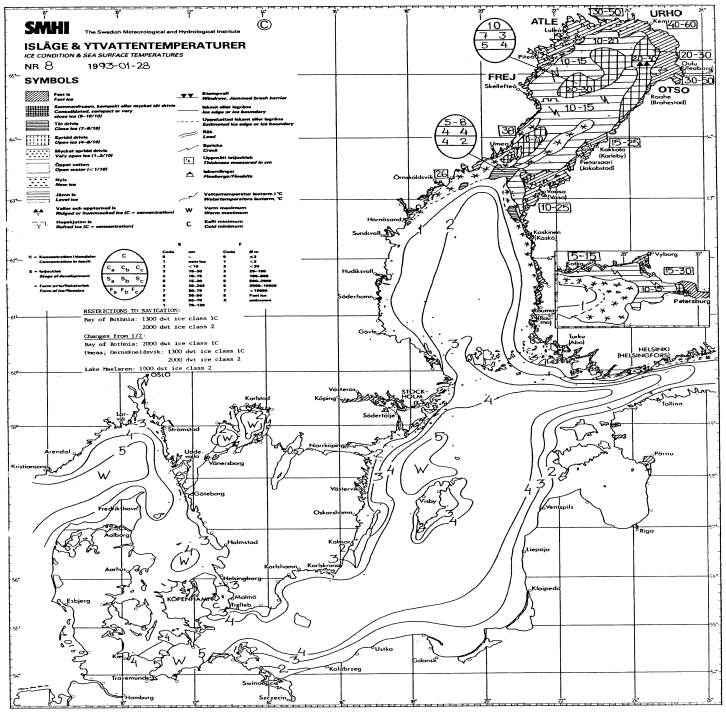

Figure 35: *Modelled mean ice thickness (in cm) from January 28, 1993, compared with the corresponding ice-sst chart published by SMHI.*

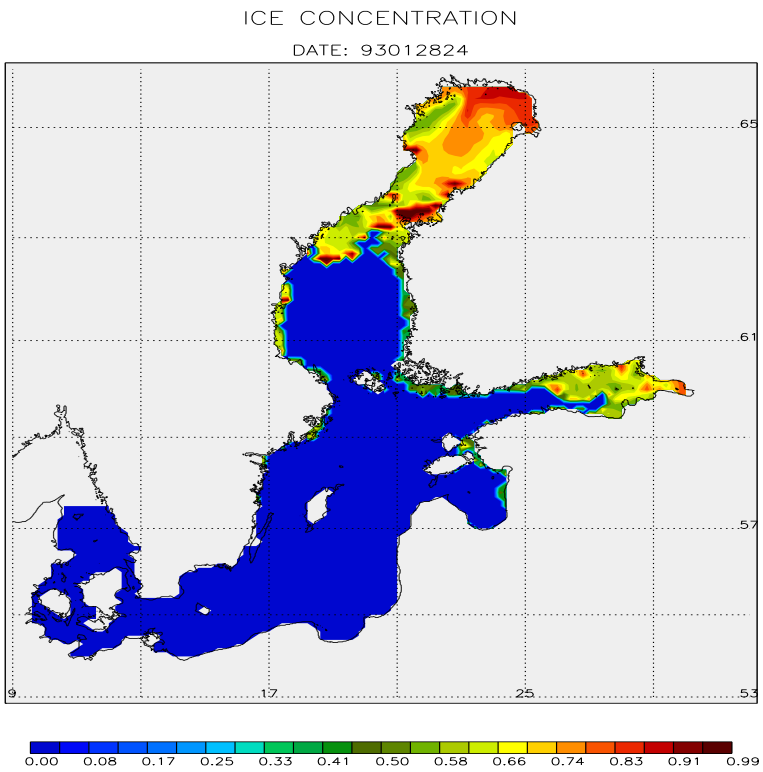

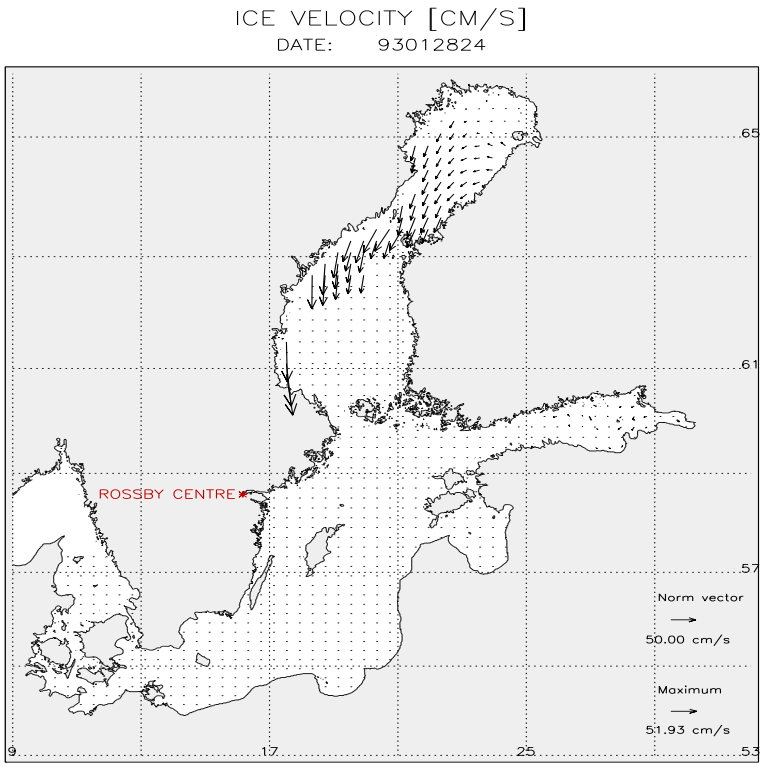

Figure 36: *Modelled ice concentration and ice velocity (in cm/s) from January 28, 1993.*

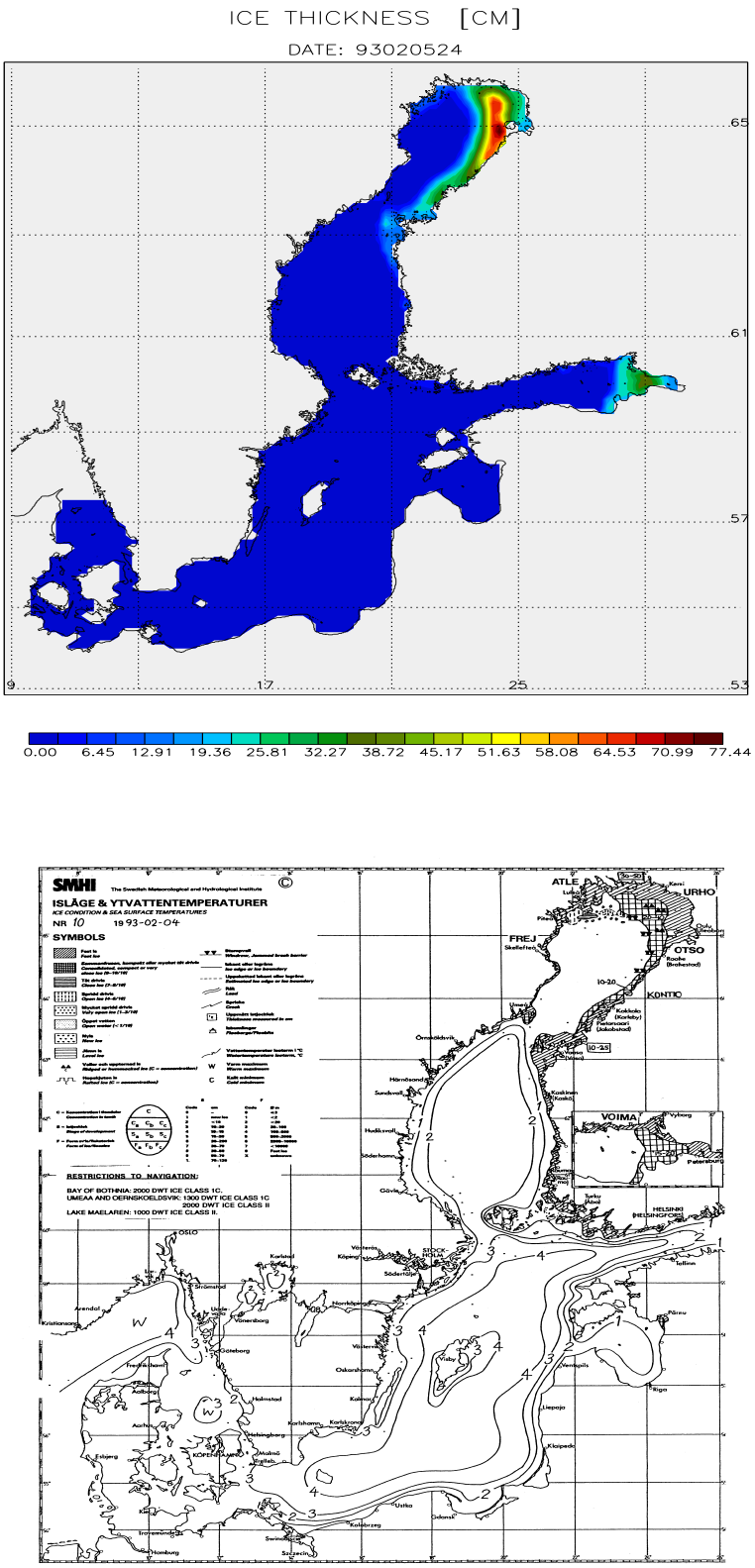

Figure 37: *Modelled mean ice thickness (in cm) from February 5, 1993, compared with the corresponding ice-sst chart published by SMHI from February 4, 1993.*

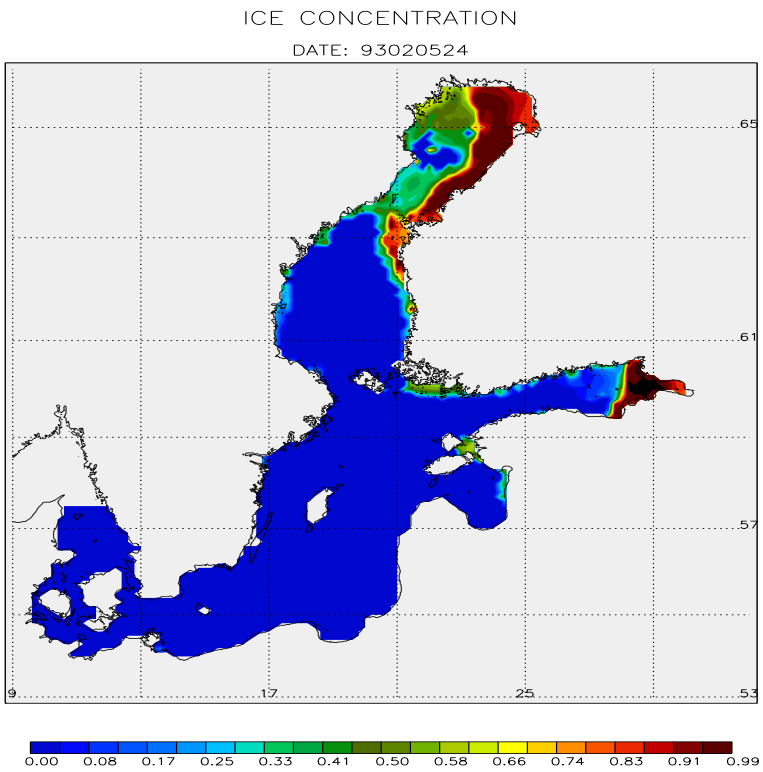

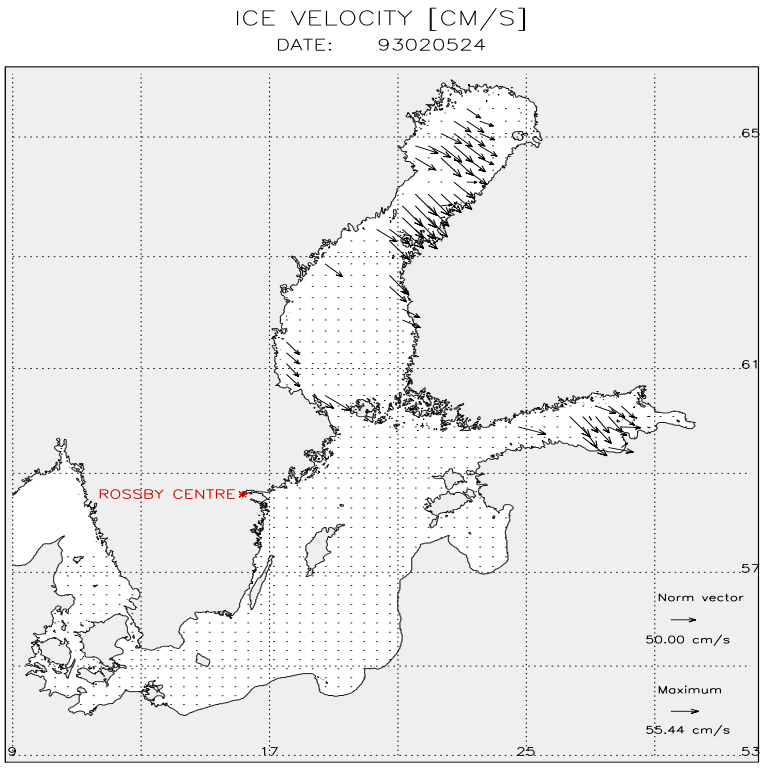

Figure 38: *Modelled ice concentration and ice velocity (in cm/s) from February 5, 1993.*

southward ice drift (Fig.36) through the narrow between Bothnian Bay and Bothnian Sea. During the next days, the driving wind increases and turns into an eastward direction. As a response, the model's ice is piled up in the eastern half of the Bothnian Bay, reaching 77 cm (Fig.37). At the same time, the western half is nearly emptied with large ice-free areas or concentrations from 0 to 0.35. Extended ice-free areas can also be seen in the observation (Fig.37, lower). The ice drift is clearly visible in Fig.38, lower. However, the densely covered area in the east is excluded from ice movement. The EVP ice rheology efficiently resists further deformation as the ice pressure increases with concentration and thickness. This wind event provides a distinct demonstration of the ice dynamics' effect on the ice distribution. This will become even clearer in the next subsection, by a comparison with a thermodynamic-only ice model run.

5.7.2 Without dynamic effects

In order to illuminate the role of dynamics in the sea ice model, the model has been run in a thermodynamics-only mode, i.e., ice velocities are not calculated and set to zero instead. Thus, ice advection is eliminated. Horizontal maps of mean ice thickness and concentration are given for February 5 (Fig.39), the same date used in the previous section to show the effect of the wind event. Contrary to the dynamics case (Fig.37), the thermodynamics-only run shows no sign of ice-free areas or reduced concentration. Instead, a nearly homogeneous thickness of around 15 cm thermodynamically grown ice fills the Bothnian Bay and the eastern Gulf of Finland. Concentrations are greater than 0.7, except at the ice edge. Thicknesses and concentrations are listed for both full and thermodynamic-only cases in Table 7.

Date	Dynamics	minimum concentration	maximum concentration	maximum thickness
Jan 28	no	0.66	0.84	18.03
Jan 28	yes	0.55	0.99	24.75
Feb 5	no	0.70	0.81	18.66
Feb 5	yes	0.0	0.99	77.44
Feb 25	no	0.74	0.90	22.27
Feb 25	yes	0.62	0.99	74.53

Table 7: *Minimum and maximum concentration and thickness at 3 days in 1993 for experiment with and without ice-dynamics for the Bothnian Bay.*

This striking difference clearly illustrates the role of dynamics: redistribution of ice volume in dependence on local conditions and mechanical ice properties. An omission of this controlled ice drift cannot lead to adequate fields of ice thickness and concentration. As the ice distribution is an important quantity in determining ocean-atmosphere or ice-ocean-atmosphere fluxes, dynamics should not be omitted. Furthermore, ice distribution is important output quantity in itself for the regional climate project SWECLIM. Climate impact estimates based on SWECLIM results will benefit from a full dynamic-thermodynamic ice model.

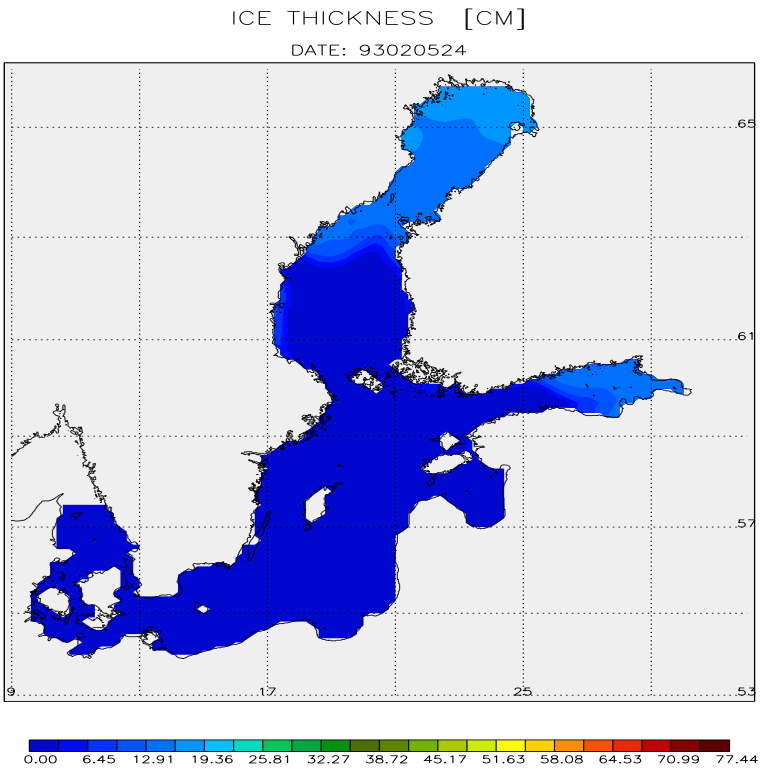

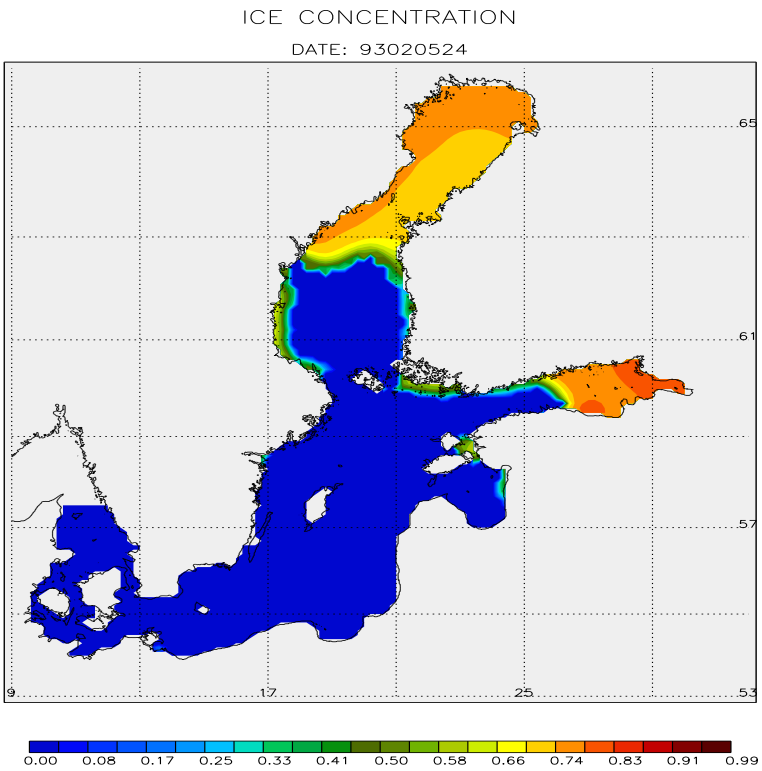

Figure 39: *Mean ice thickness (in cm) and concentration from February 5, 1993, using a thermodynamical ice model only (colour bars as in Fig.37 and 38).*

6 Summary

Within SWECLIM a 3D fully coupled ice-ocean model has been developed based on the massively parallel OCCAM code from Southampton. Compared to the global OCCAM the model has to be adopted to Baltic Sea conditions with implementations of high-frequent atmospheric forcing fields in connection with adequate bulk formulae for wind stress, heat fluxes and freshwater fluxes, solar radiation, river runoff, active open boundary conditions, a second-order moment turbulence closure scheme and a dynamic-thermodynamic sea ice model. Thereby, state-of-the-art sub-models and parameterizations have been used. RCO is the first 3D coupled ice-ocean model for the Baltic Sea with the above mentioned specifications suitable for use on mpp computers like CRAY-T3E's. Thus, a milestone for 3D ocean model development has been set. No other model is as fast as RCO. The performance has been improved significantly using advanced algorithms to optimize processor maps. This guarantees work load balance between the different processors. From now on it is possible to perform longterm simulations (10 years) within SWECLIM using a sufficiently resolved 3D Baltic Sea model.

The open boundary conditions have been tested. They allow waves to radiate out of the model domain and signals prescribed at the border to influence the model interior. No significant trends (like emptying or filling) have been observed which might prevent longer integrations of the system. An option has been included in RCO for active open boundary conditions also for temperature and salinity. For the first time the turbulence closure model has been tested within a 3D model in all Baltic sub-basins. The new flux boundary conditions for turbulent kinetic energy parameterizing breaking surface waves perform well.

First results for the hindcast period 1992/93 are presented. Therefor, realistic atmospheric, runoff and boundary data have been used. The model is initialized using observed profile temperature and salinity data. A spin-up period of 3 months starting in May is sufficient to smooth out artificial gradients from the initialization procedure and to turn in basin wide volume changes correctly.

The model results have been compared to sea level, sea surface temperature, temperature/salinity profile and ice thickness/compactness data with good agreement. Basin wide volume changes as well as daily sea level oscillations are simulated surprisingly good. Sea surface temperatures follow the observed seasonal cycle. Up- and downwelling events in RCO occur as observed with the right frequency and area extent but the sst's tend to be colder in upwelling and warmer in downwelling regions compared to observations. Mixed layer depths, which are important for the ocean heat content, agree well with previous model studies which are validated against observations intensively (Meier, 1996). The water exchange between Baltic and North Sea crucial for multi-year integrations is modelled realistically. Especially the salt water inflow in January 1993 can be reproduced. The bottom water in Bornholm Basin is replaced by new water originating from the North Sea but maximum observed bottom salinities at Bornholm Deep are underestimated by $1 - 2\,PSU$. Freezing, breakup date

and maximum ice extent are in good correspondence with observations. Improved parameterizations result in modelled ice thicknesses as observed whereas other authors report too large ice thicknesses and delayed ice melting (e.g., Haapala and Leppäranta, 1996). Multi-year simulations including mild, normal and severe winters will be necessary to elucidate this problem further. A comparison between an experiment with full dynamic-thermodynamics and one without dynamic effects reveals the importance of ice advection under wind influence. A process study from the beginning of February 1993 showed that under strong wind conditions a hole in the ice coverage can open with the size of half of the Bothnian Bay. At the end of January 1993 the Bothnian Bay, the coastal area of the Bothnian Sea and the eastern parts of the Gulf of Finland are ice covered. A couple of days later westerly winds led to wide open areas in the western Bothnian Bay while ice piled up at the eastern coasts to a correct amount. This phenomenon can be modelled only with ice dynamics included.

The aim of SWECLIM is to increase our knowledge of the effects of climate change in Sweden and the other Nordic countries. Therefor, it is necessary to understand the present climate. For the Baltic Sea even the knowledge about the present mean state and its transients is rather poor. Only a small number of long-time observations like sea level records (for example from Stockholm, see Ekman (1988)), maximum annual ice extent (e.g., Palosuo, 1953; Seinä and Palosuo, 1993) or temperature and salinity profiles from monitoring stations in some of the sub-basins (e.g., Matthäus and Frank, 1992) are available. These informations are not enough to understand the driving mechanisms of mean horizontal and vertical transports of energy, momentum and matter. 3D Baltic Sea models like RCO will close this knowledge gap in future. Thereby, it will be possible to close the water and energy cycle of the Baltic catchment area, a final goal of BALTEX. By applying atmospheric forcing data from scenario simulations in one- or two-way coupled mode it will be possible to make predictions of climate change for the Baltic Sea. Impact studies of the future marine environment will be available using detailed highly resolved information from RCO. This report presents a powerful tool for solving these and other tasks.

7 Outlook

The future outlook of the oceanographic 3D modelling activities within SWECLIM can be structured in three parts as followed: sensitivity and process oriented studies, model improvements and atmosphere-ice-ocean coupling.

7.1 Process oriented studies

The next step within SWECLIM will be to perform multi-year simulations for the whole hindcast period 1980-1993 to validate the coupled ice-ocean model, RCO, in climate mode. Process oriented studies are under development with focus on seasonal to interannual timescales to investigate a) the horizontal and vertical circulation and b) horizontal and vertical heat transports. The role of sea ice in the climate system will be explored.

Today we don't know how the estuarian circulation of the Baltic works because of the high variability overlaying longterm means. The first results of RCO for 1980-1993 (not shown in this report) reveal that the mean wind-driven horizontal circulation (simply mean Ekman) influences also the vertical balances so that the traditional view of a two layer transport system needs to be revised. This effect is not included in the box model approach. Idealized response experiments with different wind fields, freshwater fluxes (river runoff, precipitation), sea level forcing in the Kattegat, ice coverage (ice/no ice) will elucidate the important processes and involved timescales.

A second set of process oriented studies will be performed to quantify the heat budget of the Baltic Sea. Questions like

- Are horizontal heat transports in the Baltic Sea important?
- What is the role of up- and downwelling regions which are not included in box models?
- What is the role of sea ice and leads for the regional climate?

etc. will be explored. Today no climatology of surface heat- and freshwater fluxes is available. SWECLIM aims to close this knowledge gap. Using the ECMWF reanalysis data as forcing additionally will give an uncertainty range imposed on the Baltic Sea climate due to inaccuracy of the atmospheric forcing fields.

7.2 Model improvements

As outlined in the report model improvements are necessary. In the sea ice model explicit ridged ice need to be included. So far ice thickness and ice concentration in the Rossby Centre sea ice model are calculated from a two-level approach. Without too much additional resources more ice classes (level ice, ridged ice, etc.) can be considered. Including a statistical ice thickness and leads distribution will influence the local heat fluxes. Lead opening due to shear deformation need to be added to the

prognostic equation for ice concentration. A more sophisticated snow model will give a better representation of the surface albedo. The impact of these improvements will be tested.

A bottom boundary layer model will be embedded. Coarse resolution level models have problems with overflows. As the Baltic Sea topography shows several sills and deep channels between the different basins, simulated mean transports of inflowing saltwater are underestimated. To parameterize the bottom boundary layer an adequate model like the one described by Döscher and Beckmann (1999) will be useful.

A new version of RCO will be extended towards the North Sea because for scenario simulations no sea level observations are available to be prescribed at the open boundaries in Kattegat or Skagerrak. The strategy has been discussed in Section 2.5 in detail.

7.3 Atmosphere-ice-ocean coupling

The oceanographic and atmospheric models at the Rossby Centre, RCO and RCA (see Rummukainen et al., 1998) will be connected, to enable a fully 3D coupled model system of the Nordic Area (RCAO). The coupling requires either the development or adaption of a coupling interface program (the "coupler"). Special emphasis will be given to the strategies of coupling and spin-up and to the matching of fluxes between the component systems. The coupled model RCAO will then be validated in a 10-year hindcast integration with a later extension to the BRIDGE period. This will allow us to examine consistent budgets of heat, water and energy in the fully coupled system for the first time. Later, the coupled system can be applied to future scenarios.

Acknowledgments

The SWECLIM program and the Rossby Centre are funded by MISTRA and by SMHI. The testing and running of RCO has been done on the CRAY T3E at the Swedish National Supercomputer Centre (NSC) in Linköping.

The program for the calculation of the improved processor maps and a MATLAB visualization tool have been written by Jarmo Rantakokko. A first version of the partitioning software package was developed within the HIROMB project. Special thanks are given to Torgny Faxen who has implemented a performance analysis option into RCO, to Nils Kajrup for providing oceanographic profile data from the Swedish Ocean Archive SHARK (Svenskt HavsARKiv, SMHI) and to Lars Axell for providing profile data of the Gulf of Finland and Gulf of Riga. Special thanks are given also to the oceanography model group at the Baltic Sea Research Institute in Warnemünde (IOW). They made the MOM 2.2 code with special features and options of the IOW available to the Rossby Centre to perform the model intercomparison as mentioned in Section 4. Special acknowledgment is given to Doris Pürkner-Landqvist for scanning the ice maps and other technical support. Comments on an earlier draft have been made by Lars Moen, Bertil Håkansson and Anders Omstedt.

References

Aitsam, A. and Elken, J. (1982): Synoptic scale variability of hydrophysical fields in the Baltic proper on the basis of CTD measurements. In: Nihoul, J.C.C. (ed.). *Hydrodynamics of semi-enclosed seas.*

BALTEX (1997): The main BALTEX experiment 1999 - 2001 BRIDGE – Strategic plan. *International BALTEX Secretariat publication series*, **9**, October 1997, 78 pp

Baumert, H., H. Burchard and E. Kleine (1997): On Second-Moment Closures for Marine Turbulence: A Review. Manuscript presented at the 29^{th} International Liège Colloquium on Ocean Hydrodynamics: *Marine Turbulence Revisited*, May 5 - 9, 1997

Beckmann, A. and R. Döscher (1997): A method for improved representation of dense water spreading over topography in geopotential-coordinate models. *J. Phys. Oceanogr.*, **27**, 581-591

Bergström, S. and B. Carlsson (1994): River runoff to the Baltic Sea: 1950-1990. *Ambio*, **23**, 280-287

Bettge, F., J.W. Weatherley, W.M. Washington, D. Pollard, B.P. Briegleb, W.G. Strand Jr. (1992): The NCAR CSM Sea Ice Model. *NCAR Technical Note*, **425**, 25pp

Blanke, B. and P. Delecluse (1993): Variability of the Tropical Atlantic Ocean simulated by a general circulation model with two different mixed layer physics. *J. Phys. Oceanogr.*, **23**, 1363-1388

Bock, K.H. (1971): Monatskarten des Salzgehaltes der Ostsee. *Ergänzungsheft zur Dt. Hydrogr. Z., Reihe B*, **12**, 1-147

Bodin, S. (1979): A predictive numerical model of the atmospheric boundary layer based on the turbulent energy equation. *Report Meteorology and Climatology, SMHI*, **13**, 139 pp

Bryan, K. (1969): A numerical method for the study of the circulation of the World Ocean. *J. Comput. Phys.*, **4**, 347-376

Bryan, K. and M.D. Cox (1972): An approximate equation of state for numerical models of ocean circulation. *J. Phys. Oceanogr.*, **2**, 510-514

Bumke, K. and L. Hasse (1989): An analysis scheme for the determination of true surface winds at sea from ship synoptic wind and pressure observations. *Boundary-Layer Meteorol.*, **47**, 295-308

Burchard, H. and H. Baumert (1995): On the performance of a mixed-layer model based on the $k-\epsilon$ turbulence closure. *J. Geophys. Res.*, **100**, 8523-8540

Carsey, F. (1992): Remote sensing of ice and snow: review and status. *Intl. J. Remote Sens.*, **13, (1)**, 5-11

Chapman, W.L., W.J. Welch, K.P. Bowman, J. Sacks and J.E. Walsh (1992): Arctic sea ice variability: Model sensitivities and a multidecadal simulation. *J. Geophys. Res.*, **99**, 919 - 935

Charnock (1955): Wind stress on a water surface. *Quart. J. Roy. Meteor. Soc.*, **81**, 639-640

Coward, A.C. (1997): The SWECLIM (initial) model. *Technical Report, SWECLIM*, 9 pp

Cox, M.D. (1984): A primitive equation 3-dimensional model of the ocean. *GFDL Ocean Group Tech. Rep.*, **1**, GFDL/Princeton University

Craig, P. D., and M. L. Banner (1994): Modelling wave-enhanced turbulence in the ocean surface layer. *J. Phys. Oceanogr.*, **24**, 2546-2559

Craig, P. D. (1996): Velocity profiles and surface roughness under breaking waves. *J. Geophys. Res.*, **101**, 1265-1277

Dahlström, B. (1986): Determination of areal precipitation for the Baltic Sea. In: *Baltic Sea Environment Proceedings*, **16**, 174 pp

Dera, J, (1992): Marine Physics. Elsevier, Amsterdam, 516 pp

Döscher, R. and A. Beckmann (1999): Effects of a bottom boundary layer parameterization in a coarse resolution model of the North-Atlantic Ocean. *J. Atmosph. and Oceanic Tech.* , (accepted)

Elken, J. (1996): Deep water overflow, circulation and vertical exchange in the Baltic Proper. *Report Series, Estonian Marine Institute, Tallinn*, **6**, 91 pp

Ekman, M. (1988): The world's longest continued series of sea level observations. *Pure Appl. Geophys.*, **127**, 73-77

Ekman, M. (1996): A consistent map of the postglacial uplift of Fennoscandia. *Terra Nova*, **8**, 158-165

Ekman, M. and J. Mäkinen (1996): Mean sea surface topography in the Baltic sea and its transition area to the North Sea: A geodetic solution and comparison with oceanographic models. *J. Geophys. Res.*, **101** (C5), 11993-11999

Farrow, D.E. and D.P. Stevens (1995): A new tracer advection scheme for Bryan and Cox type ocean general circulation models. *J. Phys. Oceanogr.*, **25**, 1731-1741

Faxen, T. (1999): Tuning and performance analysis of the Rossby Centre Ocean model. *Technical Report, Swedish Meteorological and Hydrological Institute, Norrköping*, 22 pp

Fennel, W., T. Seifert and B. Kayser (1991): Rossby radii and phase speeds in the Baltic Sea. *Contin. Shelf Res.*, **11**, 23-36

Friehe, C.A. and K.F. Schmitt (1976): Parameterization of air-sea interface fluxes of sensible heat and moisture by the bulk aerodynamic formula. *J. Phys. Oceanogr.*, **6**, 801-809

Gidhagen, L. and B. Håkansson (1992): A model of the deep water flow into the Baltic Sea. *Tellus*, **44A**, 414-424

Gill, A.E. (1982): Atmosphere-ocean dynamics. Academic Press, London, 662 pp

Haapala, J. and M. Leppäranta (1996): Simulating the Baltic Sea ice season with a coupled ice-ocean model. *Tellus*, **48A**, 622 - 643

Hagedorn, R., A. Lehmann and D. Jacob (1999): A coupled high resolution atmosphere-ocean model for the BALTEX region. *Contr. Atmos. Phys.*, (accepted)

Harvey, L.D.D. (1988): Development of a sea ice model for use in zonally averaged energy balance climate models. *Journal of climate*, **1**, 1221 - 1238.

Hibler, W. D. (1979): A dynamic thermodynamic sea ice model. *J. Phys. Oceanogr.*, **9**, 817-846.

Hunke, E. C. (1997): CICE: the Los Alamos sea ice model documentation and software user's manual. *Technical documentation, LACC-98-16*, 19 pp

Hunke, E. C. and J. K. Dukowicz (1997): An elastic-viscous-plastic model for sea ice dynamics. *J. Phys. Oceanogr.*, **27**, 1849-1867.

Hunke, E. C. and Y. Zhang (1999): Recent Arctic Sea Ice Change Simulated with a Coupled Ice-Ocean Model. *J. of Geophys. Res.*, (submitted)

Håkansson, B.G., B. Broman and H. Dahlin (1993): The flow of water and salt in the Sound during the Baltic major inflow event in January 1993. ICES Statutory Meeting. ICES C.M. 1993/C:57

Jakobsen, F. (1995): The major inflow to the Baltic Sea during January 1993. *J. Mar. Systems*, **6**, 227-240

Jakobsen, F. (1997): Hydrographic investigation of the Northern Kattegat front. *Contin. Shelf Res.*, **17**, 533-554

Janssen, F., C. Schrum and J.O. Backhaus (1999): A climatological data set of temperature and salinity for the North Sea and the Baltic Sea. *Dt. Hydrogr. Z.*, (accepted)

Jerlov, N.G. (1968): Optical oceanography. Elsevier, 194 pp

Karger, U. (1995): Küsteneinfluß auf mittlere Bodenwindgeschwindigkeiten über der Ostsee. Diplomarbeit, Inst. f. Meeresk., Kiel, 82 pp

Kielmann, J. (1981): Grundlagen und Anwendung eines numerischen Modells der geschichteten Ostsee. *Ber. Inst. f. Meeresk., Kiel*, **87 a/b**, 158/116 pp

Killworth, P.D., D. Stainforth, D.J. Webb and S.M. Paterson (1989): A free surface Bryan-Cox-Semtner model. *Inst. of Oceanogr. Sciences Deacon Lab. Rep.*, **270**, 184 pp

Killworth, P.D., D. Stainforth, D.J. Webb and S.M. Paterson (1991): The development of a free-surface Bryan-Cox-Semtner ocean model. *J. Phys. Oceanogr.*, **21**, 1333-1348

Krauß, W. (1973): Methods and results of theoretical oceanography. Vol.1: Dynamics of the homogeneous and quasi-homogeneous ocean. Gebrüder Bornträger, Berlin, 302 pp

Krauß, W. and B. Brügge (1991): Wind-produced water exchange between the deep basins of the Baltic Sea. *J. Phys. Oceanogr.*, **21**, 373-384

Large, W.G. and S. Pond (1981): Open ocean momentum flux measurements in moderate to strong winds. *J. Phys. Oceanogr.*, **11**, 324-336

Large, W.G. and S. Pond (1982): Sensible and latent heat flux measurements over the ocean. *J. Phys. Oceanogr.*, **12**, 464-482

Lehmann, A. (1992): Ein dreidimensionales baroklines wirbelauflösendes Modell der Ostsee. *Ber. Inst. f. Meeresk., Kiel*, **231**, 104 pp

Lehmann, A. (1995): A three-dimensional baroclinic eddy-resolving model of the Baltic Sea. *Tellus*, **47A**, 1013-1031

Lenz, W. (1971): Monatskarten der Temperatur der Ostsee. *Ergänzungsheft zur Dt. Hydrogr. Z., Reihe B*, **11**, 1-148

Leonard, B.P. (1979): A stable and accurate convective modelling procedure based on quadratic upstream interpolation. *Comp. Meths. Appl. Mech. Eng.*, **19**, 59-98

Leppäranta, M. (1998): The Dynamics of Sea Ice. In: *Physics of Ice-Covered Seas*, Lecture Notes from a Summer School in Savonlinna, Finland, June 6-17, 1994, **1**, 305-342

Leppäranta, M., S. Yan and J. Haapala (1995): Comparison of sea ice velocity fields from ERS-1 SAR and a dynamical model. In: Yan Sun (ed.). *SAR remote sensing., technical report*, **275**, Chalmers University of Technology, Gothenburg, Sweden.

Ly, L.N. (1990): Numerical studies of the surface-wave effects on the upper turbulent layer in the ocean. *Tellus*, **42**, 557-567

Magaard, L. and G. Rheinheimer (1974): Meereskunde der Ostsee. Springer-Verlag, 265 pp

Matthäus, W. and H. Franck (1992): Characteristics of major Baltic inflows — a statistical analysis. *Contin. Shelf Res.*, **12**, 1375-1400

Matthäus, W., H.-U. Lass and R. Tiesel (1993): The major Baltic inflow in January 1993. ICES Statutory Meeting. ICES C.M. 1993/C:51

Matthäus, W. and H.-U. Lass (1995): The recent salt inflow into the Baltic Sea. *J. Phys. Oceanogr.*, **25**, 280-286

Maykut, G.A. (1986): The surface heat and mass balance. In: N. Untersteiner (ed.). *The Geophysics of Sea Ice.* NATO ASI Series, B 146. New York, USA. Plenum, 395-463

Meier, H.E.M. and W. Krauss (1994): Data assimilation into a numerical model of the Baltic Sea using the adjoint method. In: *Proceedings of the* 19^{th} *Conference of the Baltic Oceanographers*, Sopot, Poland, 447-458

Meier, H.E.M. (1996): A regional model of the western Baltic Sea with open boundary conditions and data assimilation (in German). *Ber. Inst. f. Meereskunde, Kiel, Germany*, **284**, 117 pp

Meier, H.E.M. (1999): Choices for parameterization of turbulence in the Baltic Sea. In: *Proceedings of the BALTEX workshop on "Parameterization of surface fluxes, atmospheric planetary boundary layer and ocean mixed layer turbulence for BRIDGE - What can we learn from field experiments"*, Abisko, Lapland, Sweden, June 20 -21, 1999, *International BALTEX Secretariat publication series*, (in press)

Mellor, G.L. and T. Yamada (1982): Development of a turbulence closure model for geophysical fluid problems. *Rev. Geophys. Space Phys.*, **20**, 851-875

Mesinger, F. and A. Arakawa (1976): Numerical methods used in atmospheric models. Vol. 1. GARP Publications Series No. 17, WMO, Geneva, 64 pp

Millero, F.J. (1978): Freezing point of sea water, Eigth report of the joint panel of oceanographic tables and standards. *UNESCO Technical Papers in marine science*,**28**, UNESCO, Paris, France

Millero, F.J. and K. Kremling (1976): The densities of Baltic Sea waters. *Deep Sea Res.*, **23**, 1129-1138

Müller, P. and J. Willebrand (1989): Equations for oceanic motions. In: Sündermann, J. (ed.). *Landolt–Börnstein, Group V, Oceanography*, **3b**. Springer Verlag, Berlin, 1-14

Mutzke, A. (1998): Open boundary condition in the GFDL model with free surface. *Ocean modelling*, **116**

Niekamp, K. (1992): Untersuchung zur Güte der Parametrisierung von Malevskii–Malevich zur Bestimmung der solaren Einstrahlung an der Ozeanoberfläche. Diplomarbeit, Inst. f. Meeresk., Kiel, 107 pp

Omstedt, A. (1990): Modelling the Baltic Sea as thirteen sub-basins with vertical resolution. *Tellus*, **42A**, 286-301

Omstedt, A. and L. Nyberg (1995): A coupled ice-ocean model supporting winter navigation in the Baltic Sea. Part 2. Thermodynamics and meteorological coupling. *Reports Oceanography, SMHI*, **21**, 39 pp

Omstedt, A. and L. Nyberg (1996): Response of Baltic Sea ice to seasonal, interannual forcing and climate change. *Tellus*, **48 A**, 644 - 662

Omstedt, A. and J.S. Wettlaufer (1992): Ice growth and oceanic heat flux, models and measurements. *J. Geophys. Res.*, **97**, 9383 - 9390

Pacanowski, R.C. (1996): MOM 2 documentation, user's guide and reference manual. *GFDL Ocean Tech. Rep.*, **3.2**, Geophysical Fluid Dynamics Laboratory/NOAA, Princeton University, Princeton, NJ, 329 pp

Palosuo, E. (1953): A treatise on severe ice conditions in the Central Baltic. *Merentutkimuslaitoksen Julkaisu, Finnish Marine Research*, **156**, 130pp

Parkinson, C.L. and W.M. Washington (1979): A large–scale numerical model of sea ice. *J. Geophys. Res.*, **84**, 311-337

Paulson, C.A. and J.J. Simpson (1977): Irradiance measurements in the upper ocean. *J. Phys. Oceanogr.*, **7**, 952-956

Perovich, D.K. (1996): The optical properties of sea ice. *CRREL Monograph*, **96**-1. Hanover,NH, USA

Rantakokko, J, (1997): A framework for partitioning with inhomogeneous workload. *Parallel Algorithms and Applications*, (submitted, revised version of Report No. 194, Department of Scientific Computing, Uppsala University, Uppsala, Sweden, 1997)

Reed, R.K. (1977): On estimating insolation over the ocean. *J. Phys. Oceanogr.*, **7**, 482-485

Richmond, C.S. (1996): Optimisation of the OCCAM code. *Technical Report, Southampton Oceanography Centre, Southampton*, 59 pp

Rodi, W. (1993): Turbulence models and their application in hydraulics - a state-of-the-art review, *Int. Assoc. for Hydraul. Res.*, A.A. Balkema, Rotterdam, Brookfield, 3rd edition, 104 pp

Rummukainen, M., J. Räisänen, A. Ullerstig, B. Bringfelt, U. Hansson, P. Graham and U. Willén (1998): RCA – Rossby Centre regional Atmospheric climate model: model description and results from the first multi-year simulation. *Reports Meteorology and Climatology, SMHI*, **83**, 76 pp

Rutgersson, A. (1999): The sensitivity of an ocean mixed layer model to the meteorological forcing. *Technical Report PROBE CASE, SMHI*, **B 21**, 26 pp

Räisänen, J., M. Rummukainen, A. Ullerstig, B. Bringfelt, U. Hansson and U. Willén (1999): The first Rossby Centre regional climate scenario – dynamical downscaling of CO_2 - induced climate change in HadCM2 GCM. *Reports Meteorology and Climatology, SMHI*, **85**, 56 pp

Sahlberg, J. (1988): Modelling of the thermal regime of a lake during winter season. *Cold Region Science and Technology*, **15**, 151-159

Schmidt, M., A. Mutzke, T. Neumann, T Seifert (1997): Special features and options of the IOW implementation of MOM 2.2. *Technical Report, Baltic Sea Research Institute, Warnemünde*, 93 pp

Schrum, C. and J.O. Backhaus (1999): Sensitivity of atmosphere-ocean heat exchange and heat content in the North Sea and in the Baltic Sea - a comparative assessment. *Tellus*, (accepted)

Seifert, T. and W. Fennel (1994): Numerical experiments in the transition area between Baltic Sea and North Sea. In: *Proceedings of the* 19^{th} *Conference of the Baltic Oceanographers*, Sopot, Poland, 422-437

Seifert, T. and B. Kayser (1995): A high resolution spherical grid topography of the Baltic Sea. *Meereswiss. Ber., Warnemünde*, **9**, 73-88

Seinä, A. and E. Palosuo (1993): The classification of the maximum annual extent of ice cover in the Baltic Sea 1720-1992. *Meri*, **20**, 5-20

Semtner, A.J. (1976): A model for the thermodynamic growth of sea ice in numerical investigations of climate. *J. Phys. Oceanogr.*, **6**, 379 - 389

Simons, T.J. (1976): Topographic and baroclinic circulations in the southwest Baltic. *Ber. Inst. f. Meeresk., Kiel*, **25**

Simonsen, K. and P.M. Haugan (1996): Heat budgets of the Arctic Mediterranean and sea surface heat flux parameterizations for the Nordic Seas. *J. Geophys. Res.*, **101** (C3), 6553-6576

Smagorinsky, J. (1963): General circulation experiments with the primitive equations: I. The basic experiment. *Mon. Wea. Rev.*, **91**, 99-164

Steinhorn, I. (1991): Notes and correspondence - Salt flux and evaporation. *J. Phys. Oceanogr.*, **21**, 1681-1683

Stevens, D.P. (1990): On open boundary conditions for three dimensional primitive equation ocean circulation models. *Geophys. Astrophys. Fluid Dynamics*, **51**, 103-133

Stevens, D.P. (1991): The open boundary condition in the United Kingdom fine-resolution Antarctic model. *J. Phys. Oceanogr.*, **21**, 1494-1499

Stigebrandt, A. (1983): A model for the exchange of water and salt between the Baltic and the Skagerrak. *J. Phys. Oceanogr.*, **13**, 411-427

Stigebrandt, A. (1987): A model of the vertical circulation of the Baltic deep water. *J. Phys. Oceanogr.*, **17**, 1772-1785

Svensson, U. (1978): A mathematical model of the seasonal thermocline, *Rep. 1002, Dep. of Water Resour. Eng., Univ. of Lund, Lund, Sweden*, 187 pp

SWECLIM (1998): Regional climate simulations for the Nordic region – First results from SWECLIM. SMHI, November, 1998, 22 pp

UNESCO (1981): Tenth report of the joint panel on oceanographic tables and standards. *UNESCO Technical Papers in Marine Sci.*, **36**, UNESCO, Paris

Walin, G. (1977): A theoretical framework for the description of estuaries. *Tellus*, **29**, 128-136

Wattenberg, H. (1941): Über die Grenzen zwischen Nord- und Ostseewasser. *Ann. Hydrogr. Marit. Meteorol.*, **69**, 265-279

Webb, D.J. (1995): The vertical advection of momentum in Bryan-Cox-Semtner Ocean General Circulation models. *J. Phys. Oceanogr.*, **25**, 3186-3195

Webb, D.J., A.C. Coward, B.A. de Cuevas and C.S. Gwilliam (1997): A multiprocessor ocean circulation model using message passing. *J. Atmos. Oceanic Technol.*, **14**, 175-183

Webb, D.J., B.A. de Cuevas and C.S. Richmond (1998): Improved advection schemes for ocean models. *J. Atmos. Oceanic Technol.*, **15**, 1171-1187

Welander, P. (1974): Two-layer exchange in an estuary basin, with special reference to the Baltic Sea. *J. Phys. Oceanogr.*, **4**, 542-556

Wübber, C. and W. Krauß (1979): The two–dimensional seiches of the Baltic Sea. *Oceanol. Acta*, **2**, 435-446

Related www-source

(August, 1999)

SMHI: http://www.smhi.se/

Rossby Centre: http://www.smhi.se/sgn0106/rossby/index.htm

MISTRA: http://www.mistra-research.se

OCCAM: http://www.soc.soton.ac.uk/JRD/OCCAM/occam.html

SMF0: http://www.smf.su.se/

CICE: http://gnarly.lanl.gov:80/Pop/eclare/cicecode/cice.html

NSC: http://www.nsc.liu.se/

BALTEX: http://w3.gkss.de/baltex/baltex_home.html

Institutes: Baltic Sea ice - 3D ocean modelling

IfM Kiel: http://www.ifm.uni-kiel.de/to/baltex/baltex.html

IOW Warnemünde:
http://www.io-warnemuende.de/Sections/en_physhome.htm

University of Helsinki:
http://geophysics.helsinki.fi/research/snow_ice/index.html

List of Figures

List of Tables